University of West Bohemia

Faculty of Mechanical Engineering

DISSERTATION

Fracture behaviour of heterogeneous materials manufactured using additive technology

Ing. Daniel Melzer **Pilsen, 2024**

FACULTY OF MECHANICAL
ENGINEERING
UNIVERSITY OF WEST BOHEMIA

Dissertation

in support of a candidature for the academic title of PhD in the study programme

P0715D270026 – Engineering technology and materials

Ing. Daniel Melzer

Fracture behaviour of heterogeneous materials manufactured using additive technology

Supervisor: prof. Ing. Ján Džugan, Ph.D.

Statement

I declare that I have prepared my dissertation independently and have used the sources I cite and list in the list of references. The usual scientific procedures are used in the submitted scientific work.

Date

……………………………………
signature

Acknowledgements

I would like to thank my family and friends for their support during the creation of this written work. I would especially like to thank Ing. Sylwia Rzepa, for her significant help and support, which gave me the determination to complete this work. A big thank you goes to my colleagues who helped me conduct the experiments, and without whose help the results contained herein would not have been published. I also thank COMTES FHT a.s. for providing all the necessary resources for the implementation of the research part. Last but not least, I thank prof. Ján Džugan for his professional guidance during my doctoral studies.

Declaration of the project supervisor

I declare that the project Pre-Application Research of Functionally Graduated Materials by Additive Technologies, No. CZ.02.1.01/0.0/0.0/17_048/0007350, within which this dissertation was prepared, has achieved the results presented. The student’s participation in these results comprised 50% of the project.

Date

……………………………………
signature

Abstract

This thesis focuses on exploring functionally graded materials (FGM) created through additive manufacturing, specifically combining stainless steel 316L with the nickel-based alloy Inconel 718. Utilizing the directed energy deposition method, this study achieves direct joining of these two distinct materials in powder form. The research involves producing three FGM variants, each with different fusion line orientations between the materials (horizontal, vertical, and inclined) and varying sequences of material deposition. The structural and mechanical properties of these modifications are meticulously analysed. A key finding is that the sequence of material layering significantly influences the evolution of the grain structure and the extent of material intermixing. Notably, a higher level of material mixture occurs when 316L is deposited onto Inconel 718. This variation in material ordering directly impacts the formation of defects, such as pores and solidification cracks, which predominantly arise in the mixed material zone. Furthermore, the study examines how the orientation of the fusion line between the dissimilar materials affects the mechanical properties, particularly in terms of tensile behaviour. The results demonstrate a decrease in mechanical performance as the fusion line's angle increases. In evaluating mechanical efficiency and structural integrity, the vertically oriented interface exhibited the poorest interface quality. This comprehensive investigation not only contributes to the understanding of FGMs in additive manufacturing but also offers valuable insights for component repair using AM, where deposition planes might deflect from ideal horizontal orientation.

Keywords

Functionally graded materials, additive manufacturing, directed energy deposition, stainless steel 316L, Inconel 718, miniaturized test techniques.

Abstrakt

Tato disertační práce se věnuje zkoumání funkčně gradovaných materiálů (FGM) vytvořených aditivní technologií, kombinací korozivzdorné oceli 316L a niklové superslitiny Inconelu 718. Technologie přímé energetické depozice byla použita pro přímou metodu spojení dvou práškových materiálů. Výzkum obsahuje celkem 3 varianty FGM bloků, každý s rozdílnou orientací linie spojení mezi materiály (horizontální, vertikální a nakloněné) a rozdílným pořadím depozice. Byly zkoumány strukturní a mechanické vlastnosti těchto rozdílných variant. Klíčové nálezy odhalily důležitý vliv pořadí depozice materiálů na mikrostrukturální vývoj a úroveň materiálového promíšení. Zcela jednoznačně bylo pozorováno, že vyšší úroveň materiálového promíšení vzniká při depozici oceli na inconelovou slitinu. Proměnné pořadí depozice také významně ovlivňuje množství vzniklých defektů, jako jsou póry a solidifikační trhliny, které vznikají v zóně promíšení nebo její bezprostřední blízkosti. Studie dále detailně analyzuje vliv orientace linie spojení mezi rozdílnými materiály na mechanické vlastnosti. Na základě výsledků lze pozorovat jednoznačný pokles tahových vlastností s tím, jak roste náklon linie spojení. Z pohledu mechanických vlastností a strukturní integrity byla varianta se zcela vertikálně orientovaným rozhraním vyhodnocena jako ta nejméně kvalitní. Tento výzkum poskytuje znalosti ohledně aditivně vyrobených funkčně gradovaných materiálů a opravy komponent pomocí technologie DED, kde může docházet k odklonu deponované plochy od ideální horizontální orientace.

Klíčová slova

Funkčně gradované materiály, aditivní výroba, přímá energetická depozice, korozivzdorná ocel 316L, Inconel 718, miniaturizované zkušební techniky.

Contents

LIST OF ABBREVIATIONS AND SYMBOLS USED..8

1 INTRODUCTION 10

2 ANALYSIS OF THE CURRENT STATE OF KNOWLEDGE 13

2.1 ADDITIVE MANUFACTURING 13
2.2 CONCEPT OF FUNCTIONALLY GRADED MATERIALS.. 15
2.3 CLASSIFICATION OF FUNCTIONALLY GRADED MATERIALS 16
2.4 ADDITIVE MANUFACTURING OF FUNCTIONALLY GRADED MATERIALS 19
2.5 DIRECTED ENERGY DEPOSITION (DED) 22
2.6 FGM BASED ON 316L AND IN718 24
2.7 INTERFACE FORMATION IN FGM OF STAINLESS STEEL/INCONEL COMBINATION .. 26
2.8 DEFECTS IN AM STAINLESS STEEL/INCONEL FGM PRODUCTS........................ 30
2.9 MINIATURIZED TESTING TECHNIQUES 32
2.9.1 Miniaturized tensile test 33
2.9.2 Miniaturized fracture toughness measurement of FGM materials 35
2.9.3 The Inclusion of Digital Image Correlation into Material Testing........... 38

3 DISSERTATION OBJECTIVES...40

4 EXPERIMENTAL PART...41

4.1 MACHINES AND SYSTEMS USED IN EXPERIMENTAL PART 43
4.2 FGM FABRICATION PROCESS 48
4.3 CUTTING SCHEMAS AND TESTING PROCEDURES 49
4.3.1 MTT testing 49
4.3.2 Fracture toughness testing 51

5 RESULTS..54

5.1 HORIZONTAL BLOCK RESULTS 54
5.1.1 Horizontal block deposition strategy 54
5.1.2 Evaluation of porosity of HB.. 55
5.1.3 Light microscope observation of HB.. 56
5.1.4 EDS and EBSD mapping of HB 57
5.1.5 Miniaturized tensile testing of HB.. 60
5.1.6 Fracture toughness test of HB.. 64
5.1.7 Fractography of MTT and MCT specimens of HB.............................. 66
5.2 VERTICAL BLOCK RESULTS 70
5.2.1 Vertical block deposition strategy... 70
5.2.2 Evaluation of porosity of VB 71
5.2.3 Light microscope observation of VB 72
5.2.4 EDS and EBSD mapping of VB... 74
5.2.5 Miniaturized tensile test results of VB.. 76
5.2.6 Fracture toughness test results of VB 80
5.2.7 Fractography of MTT and MCT specimens of VB 81
5.3 INCLINED CONTINUOUS BLOCKS RESULTS 85
5.3.1 Evaluation of porosity of CIB... 86
5.3.2 Light microscope observation of CIB... 87

    5.3.3 EDS and EBSD mapping of CIB 89
    5.3.4 Miniaturized tensile test results of CIB 91
    5.3.5 Fractography of MTT specimens of CIB 92
  5.4 INCLINED DISCONTINUOUS BLOCKS RESULTS 94
    5.4.1 Evaluation of porosity of DIB 95
    5.4.2 Light microscope observation of DIB 97
    5.4.3 EDS and EBSD mapping of DIB 97
    5.4.4 Miniaturized tensile test results of DIB 100
    5.4.5 Fractography of MTT specimens of DIB 101
  5.5 HB SHARP INTERFACE FAILURE ANALYSIS 103

6 DISCUSSION 111

  6.1 INTERFACE ORIENTATION-DEPENDENT STRUCTURE EVALUATION 111
  6.2 POROSITY AND DEFECTS FORMATION 115
  6.3 TENSILE CHARACTERISTICS COMPARISON 118
  6.4 CRACK PROPAGATION ACROSS THE INTERFACES 123

7 CONCLUSIONS 126

  7.1 SUMMARY OF RESEARCH ACHIEVEMENTS 126
  7.2 CONTRIBUTION TO THE SCIENTIFIC DISCIPLINE 129
  7.3 CONTRIBUTION TO PRACTICE 130
  7.4 RECOMMENDATIONS FOR FURTHER RESEARCH 130

8 ZÁVĚR 131

  8.1 SOUHRN DOSAŽENÝCH VÝSLEDKŮ VÝZKUMU 131
  8.2 PŘÍNOS PRO VĚDNÍ OBOR 134
  8.3 PŘÍNOS PRO PRAXI 135
  8.4 DOPORUČENÍ NA DALŠÍ VÝZKUM 135

9 REFERENCES 137

10 LIST OF OWN PUBLICATIONS 148

LIST OF FIGURES AND TABLES 152

List of abbreviations and symbols used

Symbol	Unit	Description
a	mm	Crack length
A	%	Elongation
A_g	%	Uniform elongation
AM	-	Additive manufacturing
ASTM	-	American society for testing and materials
BSE	-	Back scattered electron
CAD	-	Computer-aided design
CIB	-	Continuous inclined blocks
CMOD	-	Crack mouth opening displacement
CWC	mm	Compositional width change
ČSN	-	Czech technical standard
d	mm	Grain size
DCPD	-	Direct current potential drop
DED	-	Directed energy deposition
DIB	-	Discontinuous inclined blocks
DIC	-	Digital image correlation
DLP	-	Digital light processing
DMLS	-	Direct metal laser sintering
DMT	-	Direct metal tooling
EBSD	-	Electron back scattered diffraction
EDS	-	Energy dispersive spectroscopy
EP	-	Elastic plastic
FCG	-	Fatigue crack growth
FDM	-	Fused deposition modelling
FGM	-	Functionally graded material
HB	-	Horizontal block
HT	-	Heat-treatment
I	A	Current
IB	-	Inclined block
ISO	-	International organization for standardization
J_{IC}	kJ/m^2	Valid value of J-integral
J_Q	kJ/m^2	Provisional value of J-integral
k	-	Proportionality coefficient
K	$MPa.m^{1/2}$	Stress intensity factor
K_{IC}	$MPa.m^{1/2}$	Valid value of stress intensity factor considered fracture toughness
K_Q	$MPa.m^{1/2}$	Provisional value of stress intensity factor
k_y	-	Strengthening coefficient
L-DED	-	Laser directed energy deposition
LE	-	Linear elastic
LENS	-	Laser engineered net shaping
LM	-	Light microscope

LMD	-	Laser metal deposition
LOM	-	Laminated object manufacturing
L-PBF	-	Laser powder bed fusion
MCT	-	Miniaturized compact test
MJM	-	Multi-jet modelling
MTT	-	Miniaturized tensile test
MTTs	-	Miniaturized test techniques
PBIH	-	Powder bed and inject head
PP	-	Plaster-based 3D printing
RA	Ω	Electrical resistance
R_m	MPa	Ultimate tensile strength
$R_{p0.2}$	MPa	Yield strength
S_0	MPa	Material constant for the stress at which starts the dislocation movement
SC	-	Solidification cracks
SCCZ	-	Sudden compositional change zone
SEM	-	Scanning electron microscope
SLS	-	Selective laser sintering
STL	-	Stereolithography
UC	-	Ultrasonic consolidation
UE	%	Uniform elongation
UTS	MPa	Ultimate tensile strength
VB	-	Vertical block
W	mm	Specimen width
YS	MPa	Yield strength
Z	%	Reduction of area
Z	%	Reduction of the cross-section
γ'	-	Secondary precipitates phases in Inconel 718 (Ni_3Al)
γ''	-	Ternary precipitates phase in Inconel 718 (Ni_3Nb)
δ	-	Stable form of (Ni_3Nb)
Δa	mm	Crack extension
$\dot{\varepsilon}$	s^{-1}	Strain rate
η	-	Triaxiality
ρ	Ω	Specific electrical resistance

1 INTRODUCTION

Additive manufacturing (AM) ranks among the most rapidly expanding technologies in the industrial sector in recent years. Its origins date back to the 1980s when it was primarily limited to prototype applications. Since then, AM has come a long way, evolving into its current state. Initially, in 1987, AM was represented by stereolithography (STL), a process that solidifies thin layers of light-sensitive liquid polymer exposed by a laser beam. The development of the first AM system capable of processing metallic materials occurred in the 1990s. Over time, AM has surpassed its original use for rapid prototyping and is now extensively applied in the manufacturing of real components [1]. One of the key strengths of AM lies in its versatility, allowing the processing of a wide range of materials. Presently, additive technologies can be categorized into seven families, each corresponding to a basic process type [2], [3]. These families differ in the principle of material deposition, joining methods, and achievable accuracy. Consequently, each family is compatible only with certain types of materials.

AM technology is highly promising, even though it is a relatively new field of material processing. Despite significant efforts, AM has not yet established itself as a widely adopted production technology in technical applications. However, based on the Wohlers report 2023, the AM industry is expected to grow continuously with the potential to increase the share of end production applications. This trend will be strengthen with the development of new standards related to the AM [4]. While AM offers considerable advantages, such as the ability to build complex geometries, manufacture various structural parts, and facilitate component repairing processes, the final products often require post-treatment operations. The limited accuracy and unsatisfactory surface quality may necessitate subsequent surface treatment through machining. Additionally, the typical AM material structure may not always meet the specific material application requirements. Consequently, heat-treatment (HT) is frequently necessary to achieve the desired material properties. However, high technological costs are justifiable only when they are associated with a high added value of the product, eliminate the need for additional supplementary technologies or producing large series of products.

One of the reasons why AM technologies are not widely adopted in the industry compared to conventional technologies is the still not well-understood material behaviour. Unlike conventionally-processed materials, predicting the performance of AM materials is less reliable due to significant differences between individual parts. Conventionally processed materials typically exhibit low porosity levels and a uniform structure throughout the component volume. On the contrary, AM processed materials can have considerably higher porosity levels due to the complexity of geometry. Additionally, the structure and substructure features can vary based on the stability of AM-processed parameters (e.g., direct metal tooling mode in directed energy deposition – DED).

The reason why so much emphasis is placed on the development of AM is the new possibilities in the production of new materials and the production of elements with complex shapes, which are unattainable with conventional technologies. Furthermore, the AM technologies are adapted for the production of components by combining two or more different materials within single component produced in single process. This allows to produce new types of materials with unique properties for highly specialized applications. Another use that currently dominates the DED application is the repair of components and tools. DED as a repair technology can be found in many sectors, namely: aerospace, automotive, medical, service bureaus, general industry and tooling, oil & gas and energy, military etc. [5]–[8].

There are two main groups of functionally graded materials (FGM): structural FGM, characterized by a uniform chemical composition within the volume, but with locally changed structural properties through controlled deposition parameters, and compositionally FGM, based on variable chemical composition, often in the deposition direction. FGM materials manufactured by AM technologies are promising and offer new possibilities of application, but their response to mechanical loading remains uncertain. Therefore, a detailed mapping of the structural and fracture features is essential to ensure their safe use.

In AM, creating a multi-material FGM component typically involves changing the material type in the deposition (vertical) direction. This strategy of FGM production is beneficial since it aligns with the usual bottom-to-top object creation process. Moreover, this approach ensures a strong fusion between the bottom layer and the newly deposited material. Nevertheless, there are situations in which the conventional grading direction cannot be upheld throughout the AM procedure. This commonly occurs when employing DED for tasks such as repairing or finishing conventionally manufactured components. This scenario can result in material deposition on predefined geometric shapes such as, vertical wall repair, corner zone enhancements, or when fabricating intricate components with material type alterations in diverse directions. During these specific cases the interface orientation between dissimilar materials deviates from horizontal plane.

This thesis focuses on the detailed material characterization of FGM based on the combination of stainless steel 316L and nickel-based alloy Inconel 718. Carrying out this research is important from the point of view of mapping the regularities of FGM production by AM technologies, the emergence and character of the structure at the interface of different materials and defining the boundary conditions for which the final properties of FGM are acceptable in terms of mechanical properties, whether it is the production of a completely new FGM component, or repair an existing one. The laser powder blown directed energy deposition (L-DED) system was used for creating the FGM, as it allows feeding several different materials into the generated melt-pool. The structural characterization, along with the evaluation of mechanical properties, were used in order to evaluate four different types of FGM with varying interface orientation. Furthermore, the potential usability of FGM is explored, and the strengths and weaknesses of the analysed material are established.

2 ANALYSIS OF THE CURRENT STATE OF KNOWLEDGE

This section introduces the basic knowledge about the used technology of FGM production and comprehensive review of the previous researches. Summary of the most relevant findings were presented with special focus on multi-material systems based on combination of stainless steel and Inconel alloys.

2.1 Additive manufacturing

The AM, as we know it in its current form, has undergone more than 30 years of development. Starting as a technology primarily used for prototyping with polymer materials, hence the term 'rapid prototyping,' it has evolved into an industrially significant technology with its boundaries being pushed several times. Currently, AM is not only employed for prototyping but, above all, for the practical production of real-life products using a diverse range of materials (metals, ceramics, polymers) [9]–[13]. Furthermore, AM has potential to positively affect environmental impact of industries [14].

Despite the enormous AM technology evolution over the years, the principle of the manufacturing process is the same. The component is firstly designed using computer-aided design software. Usually, the model (in the case of metallic materials) is modified in size with respect to the AM process that often produces slightly larger parts due to an attached powder particles on the surface of the final product. Furthermore, in the case of complex shapes, supports needs to be designed as well, to ensure the part will not collapse during the manufacturing. The finished 3D model is transferred to the AM system compatible format (mostly STL). Based on the part size, geometry, orientation etc. the machine is prepared for the AM process and AM deposition parameters are set considering the material type. The building process itself is always the same. The component is built on the platform made of usually the same material as being deposited. The part is built in layer-by-layer repeated process when the stock material (in the form of powder, wire or sheets) is heated by the power of laser or electron beam. The process repeats as many times as was the number of slices of the original 3D model. After the deposition process is finished, the component is removed from the platform and supports are removed from the part. Additional surface treatment might be employed in order to clean the surface from undesirable un-melted particles, or remove rough surface topology [10] [15], [16].

Currently, several fundamental AM techniques are distinguished, differing from each other in terms of energy source, technical arrangement, and input materials used. However, the principle of creating a component remains the same across all techniques – material is not subtracted from a raw material, but instead, it is gradually fused together, often layer by layer. The basic classification of additive technologies according to ASTM F42 is presented in **Table 1**. This work focuses solely on the second group of processes – Directed Energy Deposition (DED), which is currently the most widespread in terms of FGM [3], [17]–[19].

***Table 1**. Seven main AM processes according the ASTM F42* [3].

Process	Brief description	Technology	Materials
Powder Bed Fusion	Laser or electron beam melts powdered material selectively layer by layer.	Electron beam melting (EBM), Selective laser sintering and rating (SLS/SHS), direct metal laser sintering (DMLS)	Metals and polymers
Directed Energy Deposition	Powder or wire is fed through the nozzle into a melt-pool generated by the laser or electron beam.	Laser metal deposition (LMD)	Metals and polymers
Material Extrusion	Material is extruded through a nozzle in tracks, which are combined into multi-layer model.	Fused deposition modelling (FDM)	Polymers
Vat Photopolymerization	A vat of liquid photopolymer resin is cured through selective exposure to light.	Seterolitography (SLA), digital light processing (DLP)	Photopolymers
Binder Jetting	Liquid bonding agents are selectively applied onto thin layers of powdered material to build up parts layer by layer.	Powder bed and inject head (PBIH), plaster-based 3D printing (PP)	Polymers and metals
Material Jetting	Droplets of material are deposited layer by layer to make parts.	Multi-jet modelling (MJM)	Polymers and resins
Sheet Lamination	Sheets of material are stacked and laminated together to form an object.	Laminated object manufacturing (LOM), ultrasonic consolidation (UC)	Paper, metals

2.2 Concept of Functionally Graded Materials

The concept of FGM was introduced to the world firstly in the 1983 in Japan. The motivation was Japanese space shuttle program which required significant material innovation due to the extreme thermal conditions, which single material components could not withstand. The combination of metal + ceramic would help to reduce thermal stresses of the component and ensure safe operation of the space shuttle. The initial idea of structure with graded properties originate from nature observation. Human bones, skin, teeth and bio-tissues of animals and tress have all gradation in properties which provides necessary hardness and ductility variations [1], [20], [21].

FGM are a relatively modern group of materials, which were developed based on the special needs of special industrial applications. Typically, automobile, biomedical, defence and aerospace areas usually require materials with a combination of very specific material properties [9]. Every material has limited number of applications in terms of properties, which are possible to achieve using various processing technologies. For instance, it is not always possible to produce a component with sufficient level of both, hardness and toughness simultaneously, as sometimes these two different properties are incompatible. Furthermore, the environment in which a certain component is employed can be characterized by significant condition changes. These changes can cause considerable gradients of physical quantities (e.g., temperature, pressure, magnetism) or changes in chemical reactivity. From an economical point of view, a solution in the form of single material component production with the best properties increases costs, as these materials are often the most expensive. Therefore, in certain cases, the only option to ensure that economic competitiveness will be maintained and that the component can withstand these environmental changes is through the combination of a modern advanced materials with a less expensive material. By combining these materials, a new component with special features called FGM is obtained. Furthermore, graded components might be used to reduce the total number of parts needed [22]–[24].

Various FGM production techniques can be used nowadays. The corresponding joining technique shall be used based on the certain material application. Production techniques can be classified with respect to the principle of the process. Individual methods based on the principle of FGM creation are listed in **Table 2** [25]. The first group based on the powder densification method is the most similar to the AM techniques.

***Table 2**. List of various FGM production techniques classified according to the process type* [25].

Process	Variability of transition function	Versatility on phase content	Type of FGM	Versatility in component geometry
Powder stacking	Very good	Very good	Bulk	Moderate
Sheet lamination	Very good	Very good	Bulk	Moderate
Wet powder spraying	Very good	Very good	Bulk	Moderate
Slurry dipping	Very good	Very good	Coating	Good
Jet solidification	Very good	Very good	Bulk	Very good
Sedimentation/centrifuging	Good	Very good	Bulk	poor
Filtration/slip casting	Very good	Very good	Bulk	Good
Laser cladding	Very good	Very good	Bulk, Coating	Very good
Thermal spraying	Very good	Very good	Coating, Bulk	Good
Diffusion	Moderate	Very good	Joint, Coating	Good
Directed solidification	Moderate	Moderate	Bulk	poor
Electrochemical gradation	Moderate	Good	Bulk	Good
Foaming of polymers	Moderate	Good	Bulk	good
PVD, CVD	Very good	Very good	Coating	Moderate
GMFC process	Very good	Moderate	Bulk	Good
DED	Very good	Very good	Bulk, coating, joint, thin walled	Very good

AM technologies are very promising in terms of FGM production. AM provide a great design freedom of build products. Careful control of deposition parameters can contribute to the structural and compositional changes in certain component areas and directions. However, although AM brings these advantages, by the very nature of its technological process the produced components exhibit increased uncertainty of final structural and mechanical features compared to conventional materials. The uncertainty is even greater in the case of FGM since the multi-material systems formation is generally more complicated. AM material properties are very sensitive to deposition parameters, hence constant investigation of FGM based on AM technologies is actual.

2.3 Classification of functionally graded materials

There are numerous studies that provided many possible classification systems of FGM [26]–[33]. One classification system categorizes FGM based on processing methods, as presented in **Figure 1**, with two main FGM groups: Thin and Thick, characterizing the scale. FGM produced through AM processes are assigned to the Thick FGM group. Another classification takes the scale into account as well, but it is not directly related to the processing technologies. This system divides FGM into three main groups: Bulk Materials, Surface Coatings, and Interfacial Layers, based on the volume of material in which the gradient of chemical composition is created. The third possible classification system is more suitable to the AM technology. It is based on the various build strategies of multi-material component production. The corresponding strategy is chosen based on the product application, required precision and whether the material is graded structurally or compositionally [34]–[40]. Last two factors are also the main groups into which FGM can be classified as follows:

- Structurally graded materials
    - Porous FGM
    - Structural FGM
- Compositionally graded materials
    - Direct joining
    - Gradient path method
    - Intermediate section method

The group of structurally graded materials is characterized by the uniform chemical composition within the component volume. The specific various properties in certain locations are achieved by the change of deposition parameters. Numerous studies demonstrated the sensitivity of the material to the deposition parameters and how their changes can lead to the structural changes [41]–[46]. As presented by many authors before [47]–[52], by the change of deposition parameters (e.g. laser power, laser scanning speed, preheating temperature) grain size, grain orientation, grain morphology, pores size and distribution can be successfully controlled. A special case of porous FGM are functionally graded cellular structures. These mostly bio-inspired materials for implants or bone replacements allow to build density graded components by adjusting the lattice size and arrangement [53]–[57].

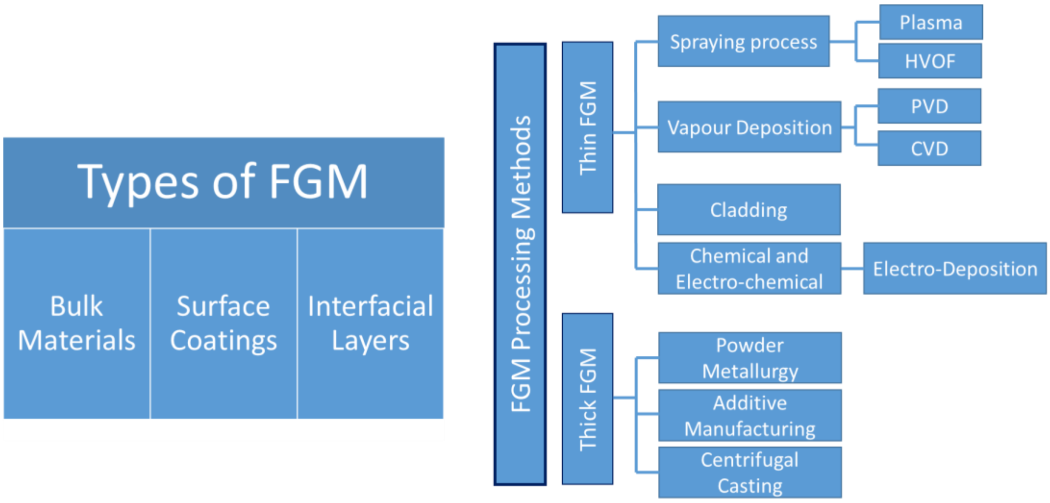

Figure 1. *FGM basic classifications based on the scale and production method* [29].

FGM produced in this thesis is classified as compositionally graded material. The difference between the individual subgroups for the case of a combination of two materials is depicted in **Figure 2**. The FGM group of interest within the thesis is compositionally graded materials based on direct joining method. When multi-material fabrication based on two different materials is considered, the direct joining principle lies in direct deposition of the melted material A on the previously deposited material B. Gradient path method requires creation of gradient transition area where the ratio of chemical composition of two main constituents is changing stepwise from 100% of material B to 100% of material A. Compare to direct joining method, each of the unique layer of certain chemical composition require its own optimized deposition parameters. This is not a problem in the case of direct joining method, where only two deposition parameters sets are needed. Third group named intermediate section method shows that the gradient transition is realized by third type of material that is used as the bonding constituent between the main material A and B. The principle of this FGM group is the fact that the chemical composition of material C is different from two main materials A and B. This is very helpful in the case when two significantly different materials needs to be bonded together but the character of the bond without using additional material does not allow its production or lacks quality [30].

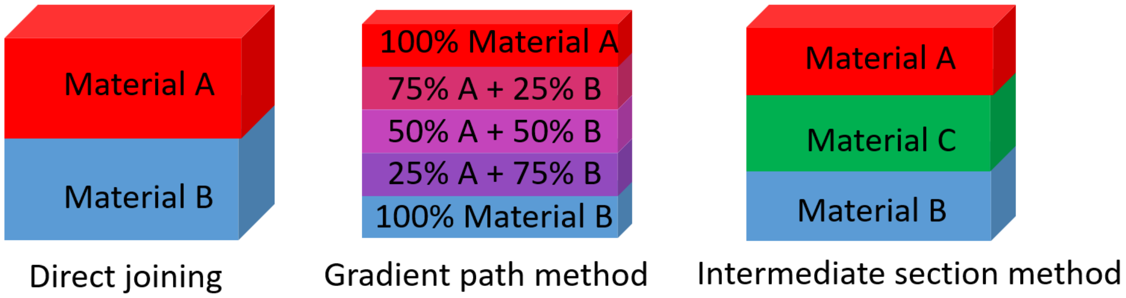

***Figure 2**. Graphical representation of different joining methods of FGM production* [30].

2.4 Additive manufacturing of functionally graded materials

A modern production method involved in FGM fabrication is AM. Compared to other production processes depicted in **Table 2**, AM offers several significant advantages that increase the effectiveness and value of the final products. The entire process is computer-assisted, which enhances the precision of the manufactured parts. Products with complex geometries can be built with minimal amounts of support material. As-built shapes can be optimized to minimize the need for additional machining operations. Moreover, AM allows for a gradual change of single material properties in certain locations or directions by adjusting the deposition parameters accordingly. Despite AM's multifunctional capabilities for FGM fabrication, there are still numerous challenges that require further investigation and resolution. The study [58] summarized current critical challenges of FGM production using AM technologies. The challenges investigated within the present thesis are marked with bold text, namely:

- Material combination issue – The issue of material combination arises when creating a chemical gradient within a single component, which primarily aims at synergizing various properties of each material type. The variability of material properties is fundamental to the creation of FGM, but it also complicates the production process. Challenges arise when the joining materials have compatibility issues, such as significant differences in melting points, crystal cell parameters, phase transformations or thermal conductivity. Additionally, detrimental intermetallic phases may form during their joining, necessitating the consideration of a different material-bonding layer. However, the presence of a third material type in the multi-material bonding introduces further difficulties in selecting appropriate processing and post-processing parameters. Furthermore, careful analysis of ternary phase diagrams is necessary to address these challenges.

- **Defects formation** – AM technology, although modern, is known for fabricating materials that usually contain a higher number of structural defects compared to conventionally processed materials. The complexity of the AM process, where re-melting and re-heating of deposited material occur within the melt-pool under the influence of deposition parameters, leads to an increased number of defects. Melt-pool stability strongly depends on these parameters, which in turn affect the formation of defects. When different materials are melted together and mixed within a single melt-pool, the formation of defects may be further enhanced compared to materials with a chemically homogeneous structure. The flow of melted materials within the melt-pool can be significantly altered due to variations in densities and thermal properties, such as solidification rate and heat conductivity. For instance, in the case of a stainless steel/Inconel combination, solidification and ductility dip cracks are often reported, occurring in both directly joined and gradient path fabricated materials.

- Processing and post-processing parameters optimization – Each of the single materials in AM requires careful selection of deposition parameters. As mentioned earlier, the choice of deposition parameters is critical as it strongly influences defects formation and the level of fusion. Furthermore, when two or more material systems are deposited, these parameters might need additional optimization. The parameters of one material can unfavourably affect the structure and properties of the second material, particularly at the fusion line, where direct bonding between different structures is situated. Post-processing parameters selection is another crucial aspect of AM-produced parts, especially in the case of FGM. Optimizing post-processing parameters, such as HT, can be very challenging for FGMs. In studies [59], [60], heat treatment, specifically aging, was conducted on 316L and Inconel 718/625 FGMs. The results demonstrated that aging can significantly increase the mechanical properties of Inconel 718 but, at the same time, cause the properties of 316L to decrease below the as-deposited state. Similarly, annealing resulted in an overall decrease in the hardness of the FGM. However, it is important to note that the annealing temperature can affect whether the hardness of the Inconel part of the structure drops below the original minimal hardness of 316L in its as-deposited state.

- **Order of material deposition** – In chapter 2.3, three basic joining methods for producing FGM were introduced. Considering these methods and the variability of properties in the two main constituents, the order of deposited materials becomes a critical factor that affects the nature of the multi-material interface. Different deposition parameters and the position of the top or bottom material within the multi-material melt-pool result in various types of interfaces based on the level of material mixture. The flow of melted materials and the varying level of chemical composition gradient strongly influence the mechanical properties of the interface and the potential formation of defects. Additionally, the power of the laser beam directly impacts the penetration depth into the substrate.

- **Orientation of the multi-material interface** – The most common strategy for creating a multi-material FGM component involves a material type change in the deposition (vertical) direction. This approach is favoured in AM because the object is built from the bottom platform to the top position, allowing for effective fusion between the bottom layer and newly deposited material. However, there are cases where maintaining or desiring a vertical grading direction is not possible due to the complex geometry of the product. For example, when joining two materials with significantly different melting points, the power source might cause deeper penetration into the substrate than is acceptable, leading to unwanted shifts or distortions in the original interface location. In such cases, it may be preferable to situate the multi-material interface within a vertical plane to avoid overheating the substrate. Geometrically, L-DED is limited when depositing material in the corner zone of a component due to restricted nozzle motion and the vertical wall of the corner impeding complete nozzle access. Numerous studies have discussed the effect of interface orientation and structure design of FGM materials on the obtained results [61]–[63]. However, many of these presented results primarily focus on polymer materials, and their applicability to metallic materials cases cannot be directly transferred [64]–[67].

2.5 Directed energy deposition (DED)

DED is one of the most suitable AM processes when FGM are fabricated [61], [62]. DED process can be further classified based on the various feeding material and energy source types. Following DED system description corresponds to the DED based on laser energy source and feeding powder material since this type was used for the FGM fabrication within present thesis.

The DED system shares many features common with other AM systems. The process schema of DED is visualized in **Figure 3** [63]. Like any other AM system, the DED system requires a previously designed 3D model of the manufactured product. Based on the STL or other formats, the part is built layer by layer, from the bottom to the top. The DED system's chamber workspace contains a table on which the platform or the component for repair is attached. Above the table, there is a deposition head, which integrates laser optics, powder nozzle(s), inert gas tubing, and in some cases, sensors. The nozzle serves as a powder feeder, controlling the amount of powder fed to the platform, and thus affecting the production rate. The material deposition is controlled by relative differential motion between the substrate and the deposition head. This motion can be achieved by moving the deposition head, moving the substrate, or using a combination of both. Typical DED systems use 3-axis motion, where the deposition occurs in a vertical manner. However, 4- or 5-axis systems that use rotary tables or robotic arms are also available for more complex operations [68], [69].

Preheating of the platform may be performed before the deposition process to reduce residual stress in the final part. In comparison to other popular methods like Laser Powder Bed Fusion (L-PBF), the melted metal powder in DED is not pre-laid on the substrate; instead, it is melted as it is being deposited. The deposition process involves feeding material powder through the nozzle onto the platform. As the powder flows, it collides with the focused laser beam. Powders particles are melted in the moment they enter the melt-pool created by the power source in the substrate. In some cases, powder can be melted during the collision with the beam and arrive into melt-pool in molten state. However, this is not very typical procedure. Deposition process is conducted under the protective atmosphere of a shield gas, such as argon or helium. Once a full layer of material is deposited, the nozzle is moved up by the height of the deposited layer, and the process is repeated until the entire object is built. When depositing FGM, the system may employ several powder feeders that can be controlled independently. This allows for changes in material type and deposition parameters as needed [70], [71].

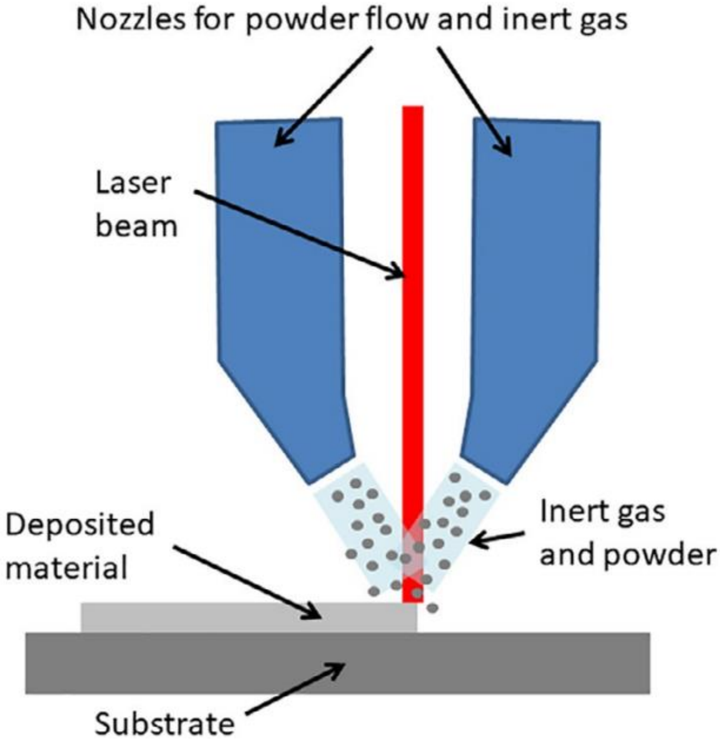

Figure 3. *Schema of directed energy deposition process principle* [63].

After the deposition process is finished, the part usually needs to be cleaned (sand-blasting) since the surface contains many un-melted powder particles that were rebound during the process. Additional machining operation of the holes and other contact surfaces is needed as well, because the rough surface might causing the fatigue crack to initiate easier compare to machined surface [10].

Heat treatment might be required in order to decrease residual stress level. After the part is cut out the deposition platform, considerable deformation might occur as a result of residual stress. Another aging treatment might be suggested in order to enhance the mechanical properties of the material, which are not sufficient in the as-deposited state.

As mentioned before, DED is suitable process for the FGM fabrication. The feeders controlled separately allow continuous change of deposited material or their combination in various ratio. Furthermore, DED systems allow material deposition on the surface of already existing parts. This is mainly applicable for product repair operations. The precision, heat control, full automation and excellent metallurgical bonding are the main advantages compared to other conventional welding methods.

2.6 FGM based on 316L and IN718

Steel 316L is an austenitic low carbon stainless steel, commonly used due to its relatively low cost. Besides iron, 316L contains chromium (16-18%), nickel (10-12%), and molybdenum (2-3%). The addition of molybdenum enhances its corrosion resistance against chlorides and reducing acids. Thanks to its excellent weldability, 316L stainless steel finds widespread use in various industries, including petrochemical, marine, and medical applications. During the cooling and repeated heating of the deposition process, stainless steel does not undergo any allotropic transformation. However, the presence of detrimental σ phase may occur in the as-deposited structure [72].

The nickel-based superalloy, Inconel 718, is a precipitation-hardenable material. Its heat-treated state allows for reinforcement of the structure through solid solution and precipitation of second phases. The austenitic matrix γ is a solid solution of chromium, iron, and molybdenum in nickel, with a face-centered cubic lattice. The matrix is reinforced by secondary precipitates phases such as γ’ (Ni_3Al), γ” (Ni3Nb), δ (stable form of Ni3Nb), and carbides. Inconel 718 exhibits excellent properties at both high and low temperatures, ranging from -200°C to 650°C. Additionally, it can withstand high pressures and offers excellent corrosion resistance against high-temperature chemical fluids. Consequently, Inconel 718 is widely used in applications where parts are exposed to high-temperature and high-pressure environments, such as heat exchangers, gas turbines, and aircraft. However, one limitation of Inconel 718 is its high cost. Therefore, combining it with other low-cost materials, such as stainless steel 316L, provides an attractive compromise [73].

Heterogeneous multi-materials based on the combination of stainless steel and nickel-based superalloys are relatively widespread in various technical applications.

Components built from this combination exhibit the strength at elevated temperatures and corrosion resistance of nickel-based alloys, as well as the cost-effectiveness of stainless steel. Such materials are capable of withstanding significant temperature variations in different locations, making them suitable for diverse applications. These material combinations find use in vessels in the chemical and petrochemical industry, nuclear power generation construction, pressure vessels, marine projects, aircraft components, combustion chambers, and turbine parts.

The reason for the widespread use of the combination of stainless steel and Inconel alloy lies in the compatibility of their properties. **Table 3** provides a comparison of several structural and physical parameters of 316L and IN718. Properties such as melting point, matrix phase type, lattice parameters, and density are very similar for both materials. These parameters are crucial when producing a joint, as they allow for harmonious interaction between the materials without causing significant adverse effects. For example, a higher difference in lattice parameters can lead to lattice distortion at the fusion line and subsequent delamination. Furthermore, similar melting points are advantageous for the joint process, and similar densities result in comparable Young's modulus, which facilitates load transfer between materials and equal deformation under certain operational loads. Additionally, both materials do not undergo phase transformation while being heated and melted repeatedly during manufacturing. However, there are significant differences in thermal properties, such as thermal conductivity, specific heat, and thermal expansion. These relative differences in thermal properties may cause significant changes in mechanical and structural properties at the interface of these two base materials. The greatest heat flow gradient might occur at the interface, where a sudden change of material type is present. As a result of slower or faster heat flow in the deposited component, significant crystal structure changes and new phase precipitation may occur. Typically, Laves phase and carbides are formed in the structure of the two main constituents [74].

***Table 3**. Specific material properties of the two main constituents 316L and IN718.*

Specific material property	Unit	Material	
		316L	IN718
Melting point	[°C]	1440	1350
Matrix phase	-	FCC	FCC
Lattice parameter	[Å]	Fe = 3.65	Ni = 3.56
Thermal conductivity	W/m/K	16.3	11.4
Specific heat	J/kg/K	500	435
Density	g/cm^3	7.99	8.19
Thermal expansion	µm/µm/°C	15.9	13.0

The combination of 316L and IN718 is a highly discussed topic in current research. Many studies have thoroughly investigated the properties of DED-deposited single materials of 316L and IN718 [75]–[82]. Additionally, multi-materials based on 316L and IN718 have been extensively examined in the past, particularly concerning their structural features. However, a detailed investigation of the mechanical properties and fracture behaviour of multi-material components has only been partially presented. Furthermore, the effect of the multi-material interface, especially in the case of metallic multi-materials, remains unexplored. The following chapters provide a comprehensive summary of the presented study, which primarily focuses on multi-material fabrication using stainless steel 316L and Inconel 718.

2.7 Interface formation in FGM of stainless steel/Inconel combination

As mentioned in the previous chapter, great compatibility of 316L and IN718 allows applying direct joining method in the multi-material component fabrication. Thus, formed multi-material interface is strictly defined by the interaction of the two main constituents and their elements. Furthermore, the character of the interface is dependent on the order of deposited materials. Many studies demonstrated application of the same deposition parameters for both main materials, 316L and IN718. However, the requirements for the parameters might change with respect to used deposition system and the level of materials dissimilarity. For instance, in the case of 316L and pure copper combination, a higher porosity was observed on the copper side due to copper’s high laser reflectivity and thermal conductivity [83]. Therefore, careful modification of deposition parameter must precede the FGM production. However, in various studies, it was demonstrated that the combination of 316L/IN718 might be deposited by even parameters for both materials.

The nature of a multi-material interface is inherently determined by the chosen joining strategy. Numerous studies have presented comparisons between the gradient path method, involving an intersection layer with controlled material ratios, and the direct joining method characterized by a discrete (sharp) multi-material interface. For instance, in a study conducted by [84], Laser Engineered Net Shaping (LENS) deposition of IN625 on 316 was carried out under constant deposition parameters. The direct joining method yielded a visually sharp multi-material interface. However, a Backscattered Electron (BSE) image, accompanied by a line Energy-Dispersive X-ray Spectroscopy (EDS) scan, revealed that the chemical composition transition occurred gradually. Specifically, the content of Fe and Ni showed a gradual decrease and increase, respectively, in the direction of IN625. Notably, no distinct defects or delamination were observed at the transition zone or in its immediate vicinity. In contrast, the gradient path intersection exhibited a more linear evolution of chemical composition across the interface. Moreover, this approach led to instances where some 316 particles were not completely melted during the process. Consequently, the detected Ni and Cr content was higher, while the Fe content was lower compared to the direct joining method.

Another study investigating the multi-material interface involving the 316L/IN625 combination was presented in [85]. DED system was utilized, employing the same process parameters for both materials. In this specific case, the primary materials were deposited alternately upon one another. The effect of the material deposition sequence on the interface characteristics was explored through imaging techniques and simulation of the flow field within the molten pool. As a consequence of varying printing sequences, distinct interfaces emerged and were observed. Notably, when 316L was deposited onto IN625, a notably deeper penetration occurred, giving rise to the appearance of molten pool banding. This phenomenon was attributed to the lower energy absorption rate and thermal conductivity of IN625 in comparison to 316L. Moreover, the columnar grains at the interface exhibited a tendency to align perpendicularly to the interface line between tracks. These grains maintained their orientation from the adjacent grains of the previous track within the re-melting region near the interface.

A distinct boundary was discerned when IN625 was deposited onto 316L, with an elemental distribution map unveiling a transition zone approximately 50 μm wide.

Within this zone, the content of Fe decreased while the content of Ni increased, transitioning from steel to Inconel. In contrast, a sudden compositional change zone (SCCZ) manifested within the first type of interface. The presence of this SCCZ within the interface was attributed to differences in chemical composition within the melt-pool. In this zone, primary dendritic arms were observable, and these arms extended into a cellular structure on both sides.

The study presented by Koike et al. [86] showed that in the direct joining of IN625 on top of 316L, a sharp interface is formed in terms of the main elements Fe and Ni. These elements are less likely to be disturbed across the interface. Conversely, other elements such as Nb and Mo were observed to be distributed in both metals (with Nb not being part of 316L).

The evolution of the interface between 316L deposited on IN625 using DED was studied by Feenstra et al. [87]. Interface analysis through EDX revealed distinctive rings of Ni-rich regions around the bottom edges of the Fe-rich melt pools within the initial dissimilar layer. This phenomenon appears to be a result of mass transport caused by the liquid or molten material being drawn into fine gaps or pores of the substrate material due to capillary action, known as the wicking effect. Additionally, compositional maps were generated across the interface. These maps demonstrated the creation of a stepwise functional gradient, with each layer (0.9 mm) having its unique elemental composition. This differentiation was observed for the main elements Fe and Ni. Interestingly, this contrasts with a previous study in which the order of deposited materials was reversed. As the distance from the first dissimilar layer increased, the wicking effect became less pronounced until the chemical composition transitioned to stainless steel. The width of the transition zone depended on the applied laser power, which varied from 1200 W to 2000 W. The widest transition zone, measuring up to 3.5 mm, was achieved with the highest laser power setting. Notably, alterations in laser power did not significantly impact the tensile behaviour of specimens oriented across the interface.

Chen et al. [88] investigated the structure of an IN625/316L block produced using LMD via the gradient path method. The chemical composition transitioned from 100% 316L to 100% IN625 through the addition of 10% IN625 at each step. The chemical composition profile demonstrated a linear evolution of Fe and Ni content within the gradient zone. Furthermore, it was observed that, as the chemical composition changed and heat accumulated, the primary dendrite arms within the microstructure became thicker, leading to increased spacing between them. This effect resulted in a decrease in the thermal gradient.

A study conducted by Koike et al. [89] compared their initial direct joint block, composed of an 316L/IN625 combination, produced via DED, with two other blocks based on the gradient path method and a block utilizing a 50/50 mixture of powders. The hardness profiles measured exhibited significant differences among the various sequences of deposited materials when the gradient path method was employed. Measurement of cooling rates revealed distinct behaviours when IN625 is deposited on 316L compared to when 316L is deposited on IN625. Specifically, when IN625 is deposited on 316L, the cooling rate value rapidly decreases, leading to a reduction in hardness until it reaches a minimum value at the 3:7 ratio of 316L:IN625. Conversely, when 316L is deposited on IN625, the cooling rate remains relatively stable throughout the entire height of the block. Consequently, this stability results in a linear and consistent increase in hardness as the 316L content increments.

Wu et al. [90] presented the microstructure evolution of an 316L/IN718-based structure. Two scanning strategies were employed: the traditional approach with a chemical composition gradient in the building direction, and the second approach with a gradient in the horizontal direction. Analysis of the chemical composition change revealed a close elemental distribution of the main elements Fe and Ni. In the traditional block, the hardness profile measurement indicated an initial decrease in hardness, attributed to the columnar structure. Subsequently, this hardness transitioned to a cellular equiaxed structure beyond 50% of IN718 content. This change is attributed to the increased cooling rate and a decrease in temperature gradient. The presence of a cellular equiaxed structure led to an immediate hardness increase, which continued to rise with higher IN718 ratios. Conversely, the horizontally graded block exhibited a consistent hardness increase as the IN718 content increased. This behaviour can be attributed to the fact that columnar dendritic growth was not as dominant as in the first case.

Wen et al. [91] conducted an investigation on a bimetallic multi-material produced via SLM using 316L and IN718. Electron Backscatter Diffraction (EBSD) mapping revealed a cellular equiaxed fine grain structure for 316L and columnar grains for IN718. A transition zone, approximately 150 μm wide, was observed between these two material regions. Within this transition zone, coarsened grains were found to be developed. This coarsening of grains was attributed to the re-melting and subsequent recrystallization of the last layer of 316L caused by the additional heat input during the IN718 deposition process.

2.8 Defects in AM stainless steel/Inconel FGM products

AM products are prone to the formation of various defects due to the complex thermal history associated with material processing. The repeated heating and cooling of deposited layers result in the development of unique structures. Unfortunately, the complexity of this processing often leads to a higher level of porosity, as well as the formation of detrimental phases or precipitates. Increased porosity, un-melted particles, and other defects are frequently influenced by the thickness of the built component. Furthermore, the impact of deposition parameters on defect formation has been demonstrated in numerous studies involving different materials [92]–[97]. In the context of FGMs with compositional variations, uncertainties in material quality and mechanical performance are heightened at the interfaces between multiple materials and in their vicinity. Numerous studies have been dedicated to the investigation of crack formation and other defects in multi-material systems based on stainless steel and Inconel. Cracking susceptibility was already investigated in the past for welding operations between stainless steel and Inconel. For instance Varestraint testing is typically employed when susceptibility to hot cracking of the material needs to be quantified. The result of the test provides the dependency between crack length and induced strain during the heating of the specimen and mechanical testing [98].

In the study [99] a weight percentage of Inconel 625 was increasing by 10% interval from individual zone of 316L to 100% of individual Inconel 625. Graded specimens with and without heating were produced and analysed. It was found that while solidification and cold cracks occurred in the no-preheated specimens, no cracks were found in synchronous preheated specimens. Multiple cracks were found in the blocks corresponding to material ratio of 90% 316L/10% Inconel625 and 70% 316L/30% Inconel625. The cracks propagated from the bottom to the top in the perpendicular direction to the substrate and across multiple layers. The position of the crack was exclusively in the center of the melt-pools. Additional SEM observation revealed that the cracking initiated from the interface between the layers and propagated along the dendritic interface in the different growth directions because of elemental segregation and stress concentration. Cracks were formed as a result of Nb and Mo elements segregation from the solidification front to liquid metal due to the strong segregation characteristics of these elements.

The study [100] conducted a comprehensive examination of defects occurring at the interface of 316L/IN718 materials, utilizing both direct joining and compositional gradient joining methods. In the 316L zone, no precipitation was observed. However, within the deposited 316L layer near the sharp interface, TiO_2 and Al_2O_3 precipitates were evident, accompanied by the presence of developed cracks. During solidification, the IN718 material exhibited the formation of a Laves phase. High cooling rates played a role in limiting the growth of the Laves phase and segregation. Initially, the deposition process exhibited elevated cooling rates due to heat transfer to the platform. As the number of layers increased, the cooling rate decreased, leading to accelerated Laves phase growth and increased Nb segregation due to heat accumulation. In the case of the compositionally graded interface, the progression of Laves phase and Nb segregation exhibited a deceleration as the IN718/316L ratio shifted from 20/80 towards the zone composed of 100% IN718. Cracks were identified at the interface between columnar and equiaxed grains, propagating from this interface towards the 316L zone along the deposition direction. Additionally, inclusions were identified in proximity to these cracks. EDS mapping indicated that these inclusions were SiO_2. In the context of the compositionally graded interface, cracks were detected across various material compositional ratios. The formation of these cracks was attributed to the presence of precipitated Nb and Mo. Furthermore, oxides such as Al_2O_3 and TiO_2 were identified as contributors to the formation of cracks.

A comprehensive study conducted by Kim et al. [101] was dedicated to addressing the challenge of producing defect-free FGMs based on 316L/IN718 through DED. The study focused on utilizing a gradient path method to achieve compositional changes, ranging from 100% IN718 to 100% 316L, with incremental additions of 10% 316L every 2.75 mm. Within the resulting microstructure, equiaxed dendrites were positioned adjacent to columnar dendrites, causing thermal and residual stresses to concentrate at the interfaces. Consequently, defects emerged at the interfaces between 30 wt% Inconel 718 and 70 wt% 316L, as well as between 20 wt% Inconel 718 and 80 wt% 316L. The microstructures observed exhibited inward lateral variability that compromised their stability, particularly at grain boundaries, contributing to defect formation. At specific transition regions, such as 50 wt% Inconel 718 and 50 wt% 316L, and 75 wt% Inconel 718 and 25 wt% 316L, segregants (such as Nb and Mo) were detected in inter-dendritic regions and precipitated at grain boundaries due to constitutional supercooling, intensifying thermal and residual stresses in these areas. Comparative analysis results revealed that defects were induced by the presence of ceramic oxides Al_2O_3 and TiO_2, which formed as a result of oxidation during the high-energy laser irradiation process. Additionally, these defects were found to propagate along intermetallic and carbide compounds, such as (Ni, Cr, Fe)2(Nb, Mo, Ti), δ-Ni3Nb, γ′- Ni3Al, Cr23C6, NbC, and MoC, primarily located at grain boundaries.

Koukolíková et al. [102] conducted a study investigating the impact of laser power on the evolution of the 316L/IN718 interface and the formation of defects. Their findings revealed that the most effective suppression of defect formation occurred within the laser power range of 350 – 500 W, with the optimum result observed at 350 W. The deposition mode DMT, also employed in the study, ranked as the second most effective option for defect suppression. The cracks that emerged during solidification exhibited an intergranular nature and a dendritic structure. This can be attributed to variations in solute concentration during the final stages of solidification, which coincide with the precipitation and formation of carbides and the Laves phase.

2.9 Miniaturized testing techniques

Many of the studies presented in the field of FGMs typically encompass two distinct types of mechanical property investigations. The measurement of hardness profiles serves as a straightforward method to assess the quality of deposited materials. However, to gain more insightful information about fabricated FGMs, the application of tensile testing becomes indispensable. The tensile test, besides basic tensile parameters for component design, provides also additional insights into the behaviour of multi-material systems during plastic deformation and aids in identifying the weakest points within the FGM structure. Most studies investigating FGM often lack a thorough assessment of mechanical properties, including comparisons with other conventional and AM materials, as well as a detailed analysis of the failure mechanism. In this thesis, conventional mechanical investigation techniques are employed, encompassing tensile tests. Furthermore, the assessment extends to include fracture toughness and fatigue crack growth techniques, ensuring a complete characterization of the FGM material while pinpointing its areas of vulnerability. It's important to note that all testing methods were executed in a miniaturized mode. This approach was chosen as it offers reliable mechanical property data for localized zones within the multi-material volume under assessment. Furthermore, no need for big material volume deposits for experiment. However, it's worth mentioning that the miniaturized testing approach poses challenges, particularly in accurately extracting specimens due to the limited dimensions.

Subsequently, the forthcoming section of the thesis introduces the foundational knowledge concerning miniaturized testing techniques. These techniques, previously employed to characterize both conventional and AM FGMs, are also a pivotal component of the present study.

2.9.1 Miniaturized tensile test

The Miniaturized Tensile Test (MTT) essentially mirrors a standard tensile test in its methodology [103]–[107]. Often, testing conditions adhere to the requirements outlined in widely recognized testing standards such as ASTM or ISO. The primary distinction between the two lies in the dimensions of the tested specimens. For instance, according to ČSN EN ISO 6892-1 [108], the standard specimen's smallest allowable cross-sectional area is 7 mm², with a corresponding gauge length of 15 mm for proportional specimens. These dimensions are determined by a proportionality coefficient k = 5.65. On the other hand, the ASTM E8/E8M-16a [109] standard sets the smallest test specimen dimensions with a gauge length of 10 mm and a specimen cross-section of 4.9 mm². This specification is designed to ensure that the gauge length is four times the diameter of the specimen [110].

It's important to highlight that the specimens conforming to ASTM standards are classified as small-size proportional testing samples. The exploration of miniaturized specimen geometries has been a subject of thorough investigation across various studies, resulting in a spectrum of diverse designs. Over time, the comparability between MTT and standard-sized specimens has been studied extensively, along with their applicability in different domains [111]–[119]. One of the most significant concerns was the potential impact of gauge length on the measured specimen elongation. To ensure comparable elongation measurements, a viable approach is to maintain the proportionality of the specimen identical to that of standard specimens. However, this entails a specimen cross-section that's more than ten times smaller in the case of MTT with a gauge length of 4 mm. The substantial reduction in specimen volume within the gauge length can potentially influence the material's stress-strain curve. Notably, research has indicated that the number of grains within the specimen's cross-section emerges as a pivotal factor in achieving size comparability[120], [121]. A smaller number of grains affects the strain hardening process during plastic deformation, leading to a reduction in stress levels in accordance with the Hall-Petch equation (1).

$$YS = S_0 + \frac{k_y}{\sqrt{d}} \tag{1}$$

Where YS is the yield strength, S_0 is a material constant for the stress at which starts the dislocation movement, k_y is the strengthening coefficient and d is the grain diameter.

Another study [122] revealed a significant disparity in strain distribution within the specimen body between standard-sized and Miniaturized Tensile Test (MTT) specimens. Bimodal strain distribution was noted for both the standard ASTM and MTT geometries. However, the peak strain values were notably higher in the case of MTT specimens. This phenomenon clarifies why the stress values for MTT specimens exceeded those of ASTM standard specimens to such a degree. Further investigations explored the effect of tensile specimen thickness on the comparability of tensile characteristics for additively manufactured materials. A study [123] tested walls with varying thicknesses ranging from 1 to 10 mm, composed of maraging steel. The findings indicated that thickness didn't influence the measured strength but did impact elongation values and data scatter. Notably, as deposited wall thickness decreased, pore size increased. Consequently, the presence of pores exhibited the most pronounced effect on the mechanical properties of thin specimens. Additional studies have addressed the influence of thickness on tensile properties for various additively manufactured materials [114], [124] with conclusions revealing variable strength values associated with different thicknesses. Discrepancies in tensile behaviour among specimens sharing the same gauge length but differing cross-sectional dimensions could potentially arise due to varying triaxiality states during the necking process. During a tensile test, the observation of uniaxial loading conditions with a triaxiality value (η) of 0.33 corresponds to uniform deformation. However, once the necking process begins, strain concentration occurs within a smaller area, leading to a shift from uniaxial stress to conditions of plane stress and plane strain [125].

The investigation of MTT potential resulted in the development of standard ISO/ASTM 52909 – Additive manufacturing of metals – Finished part properties – Orientation and location dependence of mechanical properties for metal powder bed fusion [2]. This standard introduced testing methodology, specimen’s miniaturized geometries and designation system for AM materials. The minimum dimensions of MTT specimens are determined based on the height of the multi-material interface. In the case of the direct joining method, a sharp interface with a height below 1 mm is formed, allowing for relatively short specimen gauge lengths. Conversely, the gradient path joining method frequently results in higher interfaces, exceeding several millimetres or even tens of millimetres. Tensile specimens are generally oriented perpendicular to the multi-material interface. Following the test, the fracture location is analysed to identify the weakest point within the graded component.

To date, no other studies offering tensile characteristics of the 316L/IN718 multi-material interface based on the DED process have been found. While numerous studies have addressed the combination of 316L/IN625, it's important to note that IN625 possesses considerably lower mechanical properties in comparison to IN718. Its distinct advantage lies in its enhanced corrosion resistance.

2.9.2 Miniaturized fracture toughness measurement of FGM materials

In addition to fundamental mechanical property assessments, such as tensile testing, more insightful fracture analysis techniques can be employed. Fracture toughness testing can be more intricate method that provides deeper insights into crack propagation within a material. The usefulness and applicability of miniaturized fracture toughness testing methods were investigated for many years on the conventional materials [126]–[130]. For FGMs, it's crucial to examine the material's fracture behaviour involving sharp cracks within its structure. Equally important is the analysis of material response during crack propagation across the multi-material interface and at the interface itself. The main constituents of a multi-material component, such as 316L and IN718, possess notably distinct crack propagation properties. Consequently, crack propagation from one material to another may result in a rapid increase in crack propagation rate or even sudden material failure. However, such investigations have been seldom performed in articles focusing on the FGM 316L/IN718 combination. For instance, in a study by [131] FCG of a DED-manufactured 316L/IN718 component was investigated using three-point bend specimens and the direct current potential drop (DCPD) method. Fatigue cracks propagated in both directions: from 316L to IN718 and vice versa. Notably, no significant increase in crack propagation rate was observed as the crack transitioned from the softer 316L to IN718 after crossing the interface. It's worth noting that the relatively higher propagation rates within the specimens may contribute to this negligible difference in fatigue crack propagation rates. Throughout the testing, no spontaneous or stress-induced delamination occurred. However, a distinct shielding effect emerged during the testing of the opposite crack propagation direction (316L to IN718). This shielding effect is attributed to the differing stiffness of the two main materials. During crack propagation, the less stiff material experiences a higher degree of deformation, leading to the shielding effect—a reduction in the driving force for crack propagation—when the crack travels from 316L to IN718. Conversely, an anti-shielding effect—acceleration in crack propagation rate—occurs when the transition is from IN718 to 316L. The magnitude of both the shielding and anti-shielding effects hinges on the dissimilarity between the two main materials.

In the context of fracture toughness testing, there is a notable lack of recently published articles investigating the fracture behaviour of the 316L/IN718 multi-material combination. Furthermore, there is limited available data for additively manufactured individual materials such as 316L and IN718 using the DED system. In the case of IN718, most of the presented material data pertains to the powder bed processing method.

The methodology for measuring fracture toughness relies on the material's behaviour during crack extension under quasi-static loading. Cracks within a material can grow in either an unstable or stable mode. The unstable mode is typical for brittle materials, where sudden cracking occurs under applied load, resulting in the formation of a brittle crack without significant macro-plastic deformation. The second case is stable crack growth, also initiated by applied load, but requiring continuous loading for the crack to continue to grow. This fracture mode is common for ductile materials. The investigated materials, 316L and IN718, both exhibit ductile behaviour under quasi-static loading conditions at room temperature. Consequently, the J-R curve testing methodology follows the ASTM E 1820 testing standard. However, the results from multi-material specimens can potentially lead to misinterpretation. This arises because the standard test technique is formulated for specimens made of a single material. The presence of an interface that separates two zones of dissimilar materials might deviate from the fundamental principles of this evaluation. For instance, the DCPD method of constructing J-R curves relies on monitoring voltage changes during crack extension. The DCPD method operates in accordance with Ohm's law, as defined by Equation (2):

$$V = IR = f\left(I\rho \frac{l}{W - a}\right) \tag{2}$$

In fracture mechanics, the crack propagation rate can often be monitored using methods such as DCPD. This method relies on the relationship between current (I), electrical resistivity (ρ), specimen length (l), specimen width (W), and crack size (a), as indicated by the Equation (3):

$$I = \frac{\rho \cdot l}{W \cdot a} \tag{3}$$

However, when dealing with multi-material specimens, defining the electrical resistivity becomes less straightforward, as the main materials have different resistivity values.

Another commonly used technique in elastic-plastic (EP) fracture mechanics is unloading compliance [132]. This method tracks the change in specimen compliance to monitor crack extension and energy input, corresponding to ductile crack propagation. However, this method was initially developed for monolithic specimens.

In the case of multi-material specimens, the overall specimen stiffness is influenced by the combination of individual material compliances. Furthermore, as the specimen undergoes repeated loading and unloading sequences, different material zones within the specimen experience varying levels of deformation. The specific arrangement of compliant materials, whether they are positioned in front of or behind the crack tip, becomes crucial. This arrangement affects the occurrence of shielding and anti-shielding effects, which are sensitive to the relative positions of these materials.

Numerous studies have delved into the fracture behaviour of FGMs and have examined crack-tip fields within these materials. In a particular study [133], the influence of graded material composition on fracture parameters was investigated. The study explored the variation of Young’s modulus across the multi-material interface. Although the Young's modulus of base materials remains constant, different functions can be employed to describe the transitional zone's evolution. A discretization method was proposed to analyse the stress intensity factor's sensitivity across the interface. It is important to note that this solution is applicable primarily to linear-elastic (LE) fracture mechanics scenarios, where macro-scale plastic deformation is not linked to crack extension. In situations involving EP fracture mechanics with significant plastic deformation a more intricate stress field emerges at the crack tip. As a result, the parameter K alone might not adequately describe this complex behaviour. Other studies [134], [135] have demonstrated that the crack tip fields within FGMs mirror those within homogeneous materials. However, it's crucial to recognize that the applicability of these findings is mainly within the scope of LE fracture mechanics [136].

2.9.3 The Inclusion of Digital Image Correlation into Material Testing

Digital image correlation (DIC) is a relatively recent optical technique that enables 2D and 3D measurements of surfaces on components and specimens. Its primary purpose is to quantify deformation during loading. DIC systems, as we recognize them today, were developed around the turn of the 21st century. These systems function by capturing specific deformation processes. By comparing consecutive images, the strain field can be computed from the image data. The system assigns a unique grayscale value to each pixel in the image. Each pixel, along with its immediate surroundings, constitutes a distinct unit that is tracked throughout the deformation process, including changes in length and width. Alterations in relative positions are evaluated from the initial state to the final deformation stage. Subsequently, the DIC system analyses the deformation field, enabling the identification of regions with the most significant deformation, pinpointing failure locations, or determining the magnitude of deformation that leads to failure [137]–[141].

In order to evaluate the deformation of a component and track strain evolution during the deformation process, a contrast pattern must be applied to the surface. Typically, a black and white colouring scheme is employed. This pattern serves the purpose of minimizing glare on the surface, particularly for shiny metal surfaces. However, it's crucial that the pattern applied is stochastic, meaning it's randomly distributed and non-repetitive. This stochastic pattern prevents the tracking algorithm from erroneously identifying the same pattern in different locations on the specimen. By using a stochastic pattern, the accuracy of displacement sensitivity and noise suppression is significantly improved.

DIC offers several key advantages, including:

- Comprehensive assessment of surface deformation. Each image can encompass hundreds to thousands of points (as determined by system resolution), each containing strain data.
- DIC operates as a noncontact technique, adaptable to nearly any component or specimen shape, provided the surface remains optically accessible during deformation.
- DIC excels in monitoring miniaturized test specimens, where conventional contact strain gauges are impractical.
- The DIC system furnishes accurate quantitative data, serving as input for numerical simulations and material modelling.
- In the characterization of FGMs, DIC offers vital insights into the deformation behaviour of intricate structures. It facilitates the evaluation of strain values for each distinct chemically varied segment of a component, aiding in the identification of its weakest point.

3 DISSERTATION OBJECTIVES

The aim of this thesis is to investigate the structural properties and mechanical performance of additively manufactured FGM blocks using a combination of stainless steel and Inconel alloy. Based on the current state of knowledge following objectives were suggested to be investigated:

1) **Production of FGM materials with different deposition sequences of base materials for evaluation of the most optimal sequence** - Alternate deposition sequences will be implemented during the production process of FGM using L-DED. For the evaluation of the most optimal sequence, the key material zones of interest will be the fusion lines where two base materials come into contact. These areas will be assessed and compared in terms of structural properties and mechanical behaviour.

2) **Evaluation of the influence of the interface orientation on the structural features and mechanical performance of FGM** – FGM specimens with various orientation of fusion line (horizontal – 0°, 15°, 30°, 45°, 60° and vertical – 90°) will be manufactured. Assessment of structural and mechanical properties will be crucial, in order to establish the limitation of L-DED system, when inclined interfaces are produced.

3) **Evaluation of the effect of surface treatment on the dissimilar interface evolution and defects formation** – Prior the Inconel 718 deposition, pre-machined and as-deposited state of surface of the substrate 316L will be prepared, in order to evaluate whether the substrate surface preparation affects the interface quality, especially in terms of defects formation.

4) **Evaluation of the failure mechanism of the two-material interface** – Tensile testing and fracture toughness testing of interface located specimens will be conducted. Results will be used for the assessment of the failure mechanism and crack propagation process at the fusion line of FGM. Most importantly, the failure mechanism will be evaluated for various orientations of fusion lines, which is crucial for determining the most optimal arrangement of FGM materials in real components.

4 EXPERIMENTAL PART

The motivation behind the experimental part is to comprehensively investigate and evaluate the limitations and potential solutions for component repair through DED technology. The experimental portion of the thesis focuses on investigating various multi-material blocks produced using DED technology. The FGM investigated in this study consists of a combination of stainless steel 316L and the nickel-based superalloy Inconel 718. Direct joining method was employed for all variations. The investigation encompassed four main modifications of FGM blocks, which were produced and analysed. All FGM blocks were investigated in as deposited state at room temperature conditions. The timeline of the experimental part is depicted in **Figure 4**. The first FGM modification involved arranging the base single materials with interfaces oriented horizontally within the block. This was achieved through chemical composition control during the deposition process. This particular block is referred to as the horizontal block (HB). The second modification explored the effect of extreme interface orientation on the mechanical and structural properties of FGM. For this purpose, a block with a chemical composition change oriented in the horizontal direction was manufactured. The interfaces between the materials were aligned vertically within the block, leading to the reference term vertical block (VB). The third modification comprised a group of blocks with two-material interfaces inclined at four different levels from the horizontal orientation. These inclinations were set at 15°, 30°, 45°, and 60°. This set is due to a continuous deposition strategy referred as CIB. Fourth modification is identical with CIB except the fact pre-machining of the substrate was employed in order to investigate potential interface quality improvement. A more comprehensive description of each modification's fabrication process is presented in the following subsections. Various imaging techniques were utilized to examine the multi-material structure, distribution of chemical composition, and presence of defects across interfaces and within base materials. Additionally, mechanical testing techniques such as MTT and fracture toughness test were applied to validate material properties at specific locations (interfaces and base materials) and to facilitate comparison among different block modifications.

The main discussion points of the experimental phase are outlined as follows:

- Formation of the multi-material interface through chemical composition variation.
- Examination of the influence of the sequence of deposited base materials on the nature of the multi-material interface.
- Discussion of the correlation between the type of multi-material interface and the occurrence of defects.
- Exploration of the limitations and advantages of employing miniaturized testing techniques for FGM characterization.
- Comparative analysis of mechanical test outcomes across different block modifications and other relevant findings in the literature.
- Effect of surface treatment prior the dissimilar interface deposition on the defect formation
- Investigation into the failure mechanism of interfaces.

Presented results were published in three studies dedicated to horizontal modification [142] vertical modification [143] and inclined modification [144].

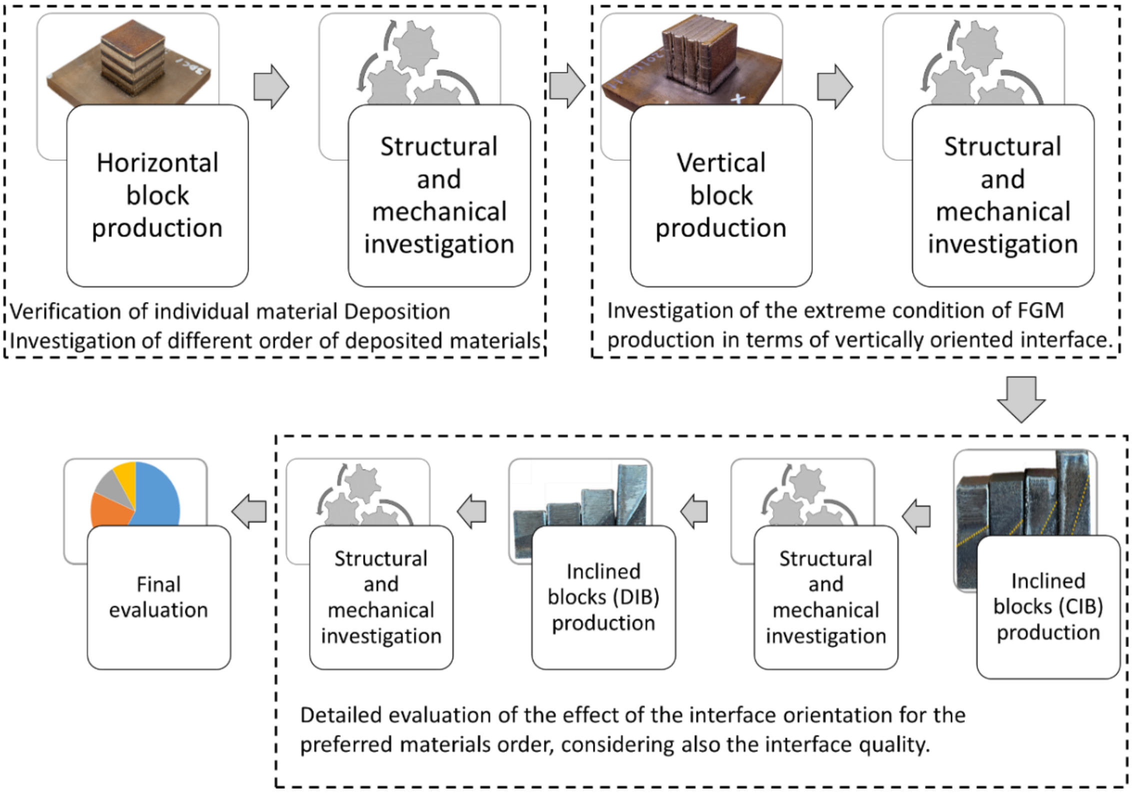

***Figure 4**. Timeline of the experimental part evolution.*

4.1 Machines and systems used in experimental part

Table 4 presents the summary of all used machines and systems that were used during the experimental procedures for measurement and evaluation of obtained results. All systems are part of the laboratories of COMTES FHT a.s. at which the experimental investigations were conducted under the supervision of responsible co-workers of departments: Material analysis, mechanical testing laboratories and material modelling.

DED deposition system used for the FGM fabrication in this thesis was DED system INSSTEK MX 600 (InssTek, Daejeon, Korea), dedicated to the L-DED process. MX 600 is equipped with 2 kW Ytterbium fibre laser. A single nozzle of diameter 800 μm was used. MX 600 use metal powder as feed material that is stored in four separated feeders.

The MX600 system offers two different power output modes. The first mode is the constant power output mode, where the laser power that melts the material remains consistent throughout the entire deposition process. The second mode is called direct metal tooling, and it operates with variable power output. In this mode, two optical sensors monitor the actual height of the deposited layer. Based on this information, the laser power is automatically adjusted to maintain a constant thickness of the deposition layer. If the last deposited layer's thickness is smaller than required, the laser power can be increased, resulting in more melted powder particles and a corresponding increase in the deposited layer thickness. Conversely, if the layer thickness is too large, the laser power can be decreased to achieve the opposite effect. Other DED systems that lack this direct metal tooling mode optimize the deposited layer height in order to maintain constant process parameters.

Limitations of this deposition system is the minimal wall thickness of 2 mm. Minimal size of a hole in the model is 2 mm. Accuracy in the horizontal plane is +0,5 mm for X and Y axes. Accuracy in vertical Z axis is +0, 25 mm in 100 mm length.

The DED system MX 600 is capable to process following groups of materials:

- Steel – P20, P21, H13, D2, 304, 316,420
- Titanium – CP Ti, Ti grade 5

- Nickel alloys – 713, 718, 738, Hastelloy X
- Cobalt – CoCr, Stellite 21, Stellite 25
- Cu
- AlSi10Mg

The materials were subjected to the metallographic preparation of grinding and polishing with the final etching using Glyceregia mixture (15 ml HCl, 10 ml glycerol, 5 ml HNO_3). After the polishing process and before the metallographic specimen was subjected to the etching the porosity measurement was carried out using NIS elements 5.2 software. All light microscopy images were taken using light microscope Nikon ECLIPSE MA200 (Nikon, Tokyo, Japan).

A Scanning Electron Microscope was used to more closely investigate character of the deposited materials. SEM investigation was performed in the YZ plane of the produced blocks as the LM analysis using microscope JEOL IT 500 HR SEM (JEOL Ltd., Tokyo, Japan) with EDAX Hikari Super camera (EDAX LLC, Mahwah, NJ, USA). A chemical microanalysis was done using Energy Dispersive X - ray Spectroscopy. The same system was also used for fractographic analysis of MTT and MCT specimens after the test.

All specimens dedicated for mechanical testing were extracted using an Electro wire cutting machine WEDM FANUC with a wire diameter of 0.25 mm. MTT specimens were polished prior the dimensions measurement and testing. CNC Machining Centre DMU 50 was used for the surface optimization of chosen blocks.

All MTT were conducted using the electro-mechanical universal test machine TiraTest with a load cell capacity of 10 kN. Fracture toughness tests were conducted on the servo-hydraulic machine MTS Landmark 100 with the COD clip gauge and load cell capacity of 10 kN. MTT specimen’s dimensions and MCT fracture surfaces were measured using Nikon – Stereo camera.

Table 4. *List of used machines and systems for the realization of experimental part in COMTES FHT a.s.*

INSSTEK MX 600 DED system

- 2kW Ytterbium fibre laser
- Motion: 3+2 axes
- Working area: 450 x 600 x 350 mm
- Multi-material deposition – 4 powder feeding systems
- Printing modules
- SDM800 (beam diameter 800 µm,
  layer thickness 250 µm)
- Auto-tracking system

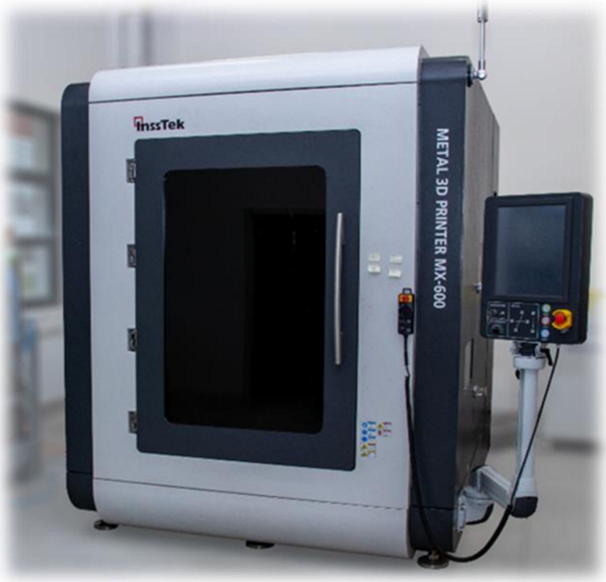

Metallographic preparation

- Grinder/polisher Tegramin
- Metallographic saw Discotom
- High precision metallographic saw with Accutom 50
- Hot mounting presses Citopress, cold mounting also available
- Electrolytical preparation - LectroPol-5
- Vibratory polishing – Buehler Vibromet

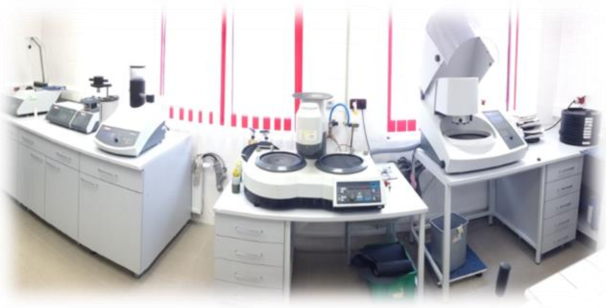

Light microscope observation

- 2x Nikon Epiphot 200 (one with PC controlled motorized stage),
- 1x Nikon MA200 with NIS elements software for image analysis

JEOL IT 500 HR – cold field emission

- EDX analysis EDAX (Octane Elite EDS System), high speed EBSD camera (Hikari Super), Detectors – SE & BSE
- Resolution up to 1,5 nm, AV: 0,1 – 30 kV, STEM detector (for TEM foils)

TiraTest universal testing machine

- Force capacity 5/10 kN
- Tensile, compression, fatigue tests
- Digital extensometer tracking system Mercury
- Possible strain control from camera measurement low cycle fatigue of mini-samples

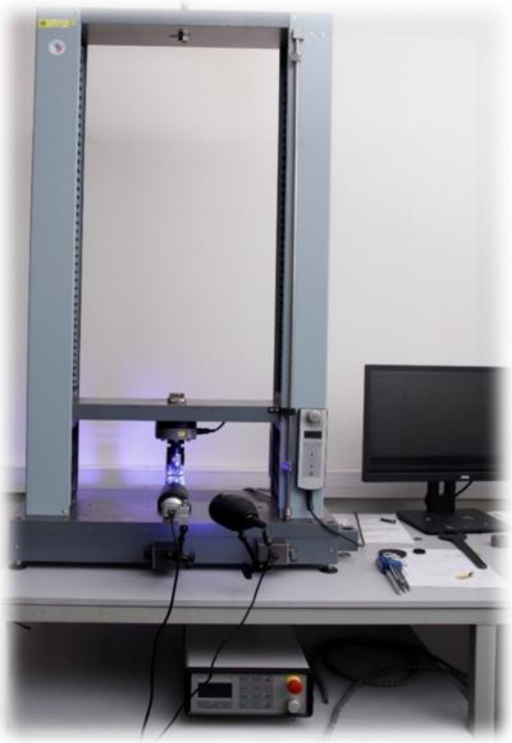

Hydraulic testing machine Landmark 100

- Max force capacity 100 kN
- Quipped with inductive heating system → isothermal or variable temperature during loading
- DCPD system for monitoring of the strain/crack in samples
- low cycle fatigue, fatigue crack growth, Threshold value, Thermo-mechanical fatigue, tensile/compression test

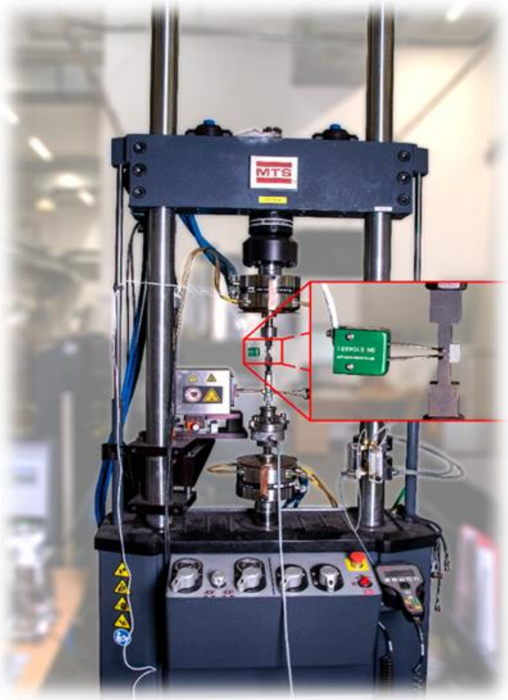

Nikon – Stereo camera

- Measurement of the cross-sectional area of MTT specimens after the test

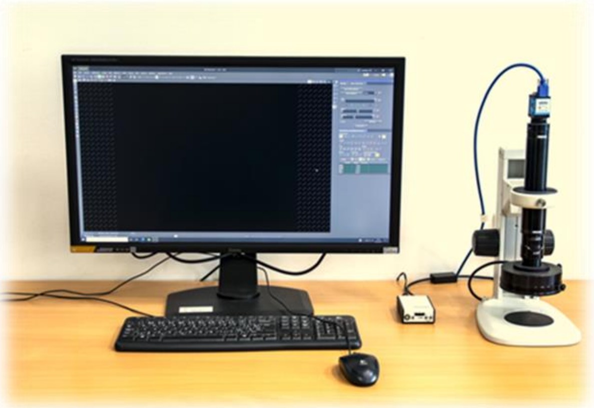

WEDM FANUC

- Maximum work piece weight: 60 kg
- capable of cutting thick, stepped and tapered parts
- multi-work piece machining
- easy-to-use Core Stitch function for even longer unmanned machining
- wire threading in just 10 seconds
- automatic in-path wire re-threading

DMU 50 Machining Center

- 5-axis simultaneous machining with fixed rotary table
- B-axis rotation range -5/ +110°
- Table load capacity up to 661.4 lbs
- Tool magazine for short setup times and downtime16/30 or 60 tool pockets
- X/Y/Z direct path measurement system (optional)

4.2 FGM fabrication process

The used deposition parameters for individual materials are outlined in **Table 5**. Powder materials were stored in two out of the four feeders, allowing for the continuous alteration of the powder type fed to the single nozzle during the deposition process. The powders used for feeding were commercially dedicated to AM techniques: 316L (Sandvik Osprey Ltd., Sandviken, Sweden, Batch: 20D0325) and nickel super alloy Inconel 718 (AP&C, Quebec, Canada, Batch: 191- A0379). The particle sizes of the powders ranged from 53 to 150 µm for 316L and 45 to 150 µm for IN718. The deposition process was managed in DMT (direct metal tooling) mode, which adjusts the laser power to maintain a consistent layer height and nozzle-melt pool distance. The process was supervised by two vision cameras. In essence, the laser power varied during deposition based on the current layer height. If the deposited layer's height fell below the pre-defined level, the laser power was correspondingly increased. The scanning strategy applied for both materials and across all block modifications was the ZigZag pattern with Contour-Filling-Contour and Contour-Filling sequences. Every odd deposited powder layer included an extra contour scan. A 90° rotation of the laser scanning direction occurred between each layer. The deposition parameters provided in **Chyba! Nenalezen zdroj odkazů.** were identical for both the Filling and Contouring p hases. The hatch distance of 0.5 mm remained consistent between the filling and contouring parts of the laser scanning, as well as between laser paths during the filling phase. The dwell time between contour-to-filling transitions and the deposition of 316L to IN718 was consistently set at 3.5 seconds, except for the DIB. The deposition process was carried out within a protective atmosphere using high-purity inert argon gas (purity level: 5.0).

Table 5*. Deposition parameters for both 316L and IN718 of produced FGM.*

Material	Laser power DMT mode [W]	Laser scanning speed [mm/min]	Laser focus [mm]	Hatching distance [mm]	Z step [mm]	Powder feeding rate [g/min]	Shield gas [l/min]	Coaxial gas [l/min]	Feeder gas [l/min]	Zone number
316L	(~417)	849	9	0.5	0.25	3	10	9	3	1, 3, 5, 7
IN718	(~375)					3.5	10	9	3	2, 4, 6

4.3 Cutting schemas and testing procedures

4.3.1 MTT testing

Examples of extraction positions of MTT specimens for all HB, VB, and IBs blocks are presented in **Figure 5**. Five replicates were extracted for each position. In the case of HB, MTT specimens were extracted in two horizontal orientations: XYZ, YZX and vertical ZYX with the body placed within single material zones. For the horizontal orientations, the entire specimen was positioned within the individual material, while shoulders of ZYX-oriented specimens crossed the interfaces. Tensile properties of the interfaces were evaluated using MTT specimens with the parallel section situated across the interface in both vertical (ZYX) and horizontal (YZX) orientations. The designation of each individual specimen is formed by material type/interface type + orientation + number of the material layer/layers boundering the interface + specimen number.

A similar extraction plan was applied to the VB block. MTT specimens located within a single material zones were manufactured in the same manner. The only distinction is that YZX-oriented specimens have shoulders placed across the interface, making them suitable for measuring interface tensile behaviour. The designation system was the same. The IBs MTT specimens were extracted only with a vertical ZYX orientation and positioned across the interface. MTT testing of single material zones was not conducted; only the tensile performance of the interfaces was evaluated. Miniaturized tensile testing setup is depicted in **Figure 6a** and MTT specimen's geometry in **Figure 6b**. The designation of the specimen's orientation follows the standard [2].

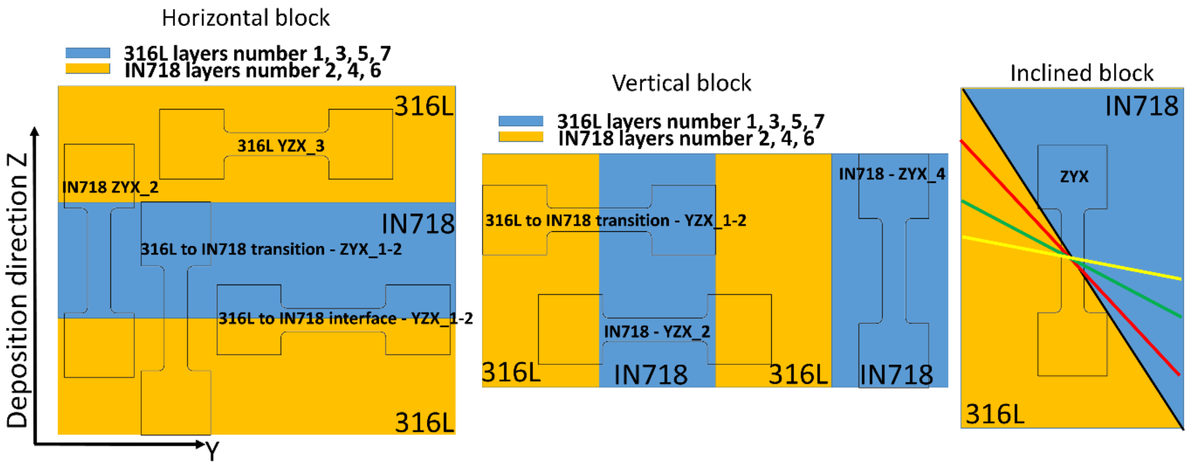

Figure 5. *Extraction plan of MTT specimens production from HB, VB and IBs with the specimen's designation system examples.*

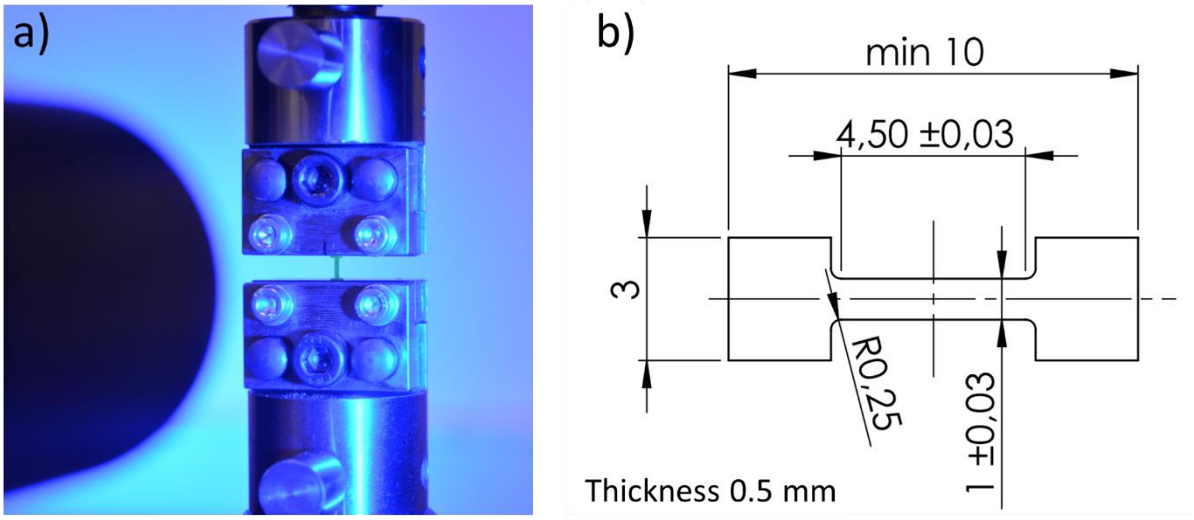

Figure 6*. a) MTT setup; b) MTT specimen geometry.*

The testing procedure followed the methodology outlined in the ČSN EN ISO 6892-1 tensile testing standard [145] and MTT specification in ISO/ASTM 52909 [2]. After production, each specimen's initial dimensions (thickness and width) were measured using a micrometre. The specimen's surface was then prepared for the DIC deformation tracking system by applying a black and white stochastic pattern using conventional sprays on the front side. Deformation was monitored using a single (2Mpix) camera. The specimen's elongation was tracked using the digital extensometer of the Mercury system (Real-time measurement). A gauge length of 4 mm was used, considering the specimen's initial cross-section size of 0.5x1 mm². Each specimen was first attached to the bottom grip, and the opposite side of the specimen was gripped as well during pre-loading with a constant force of 10 N. The tests were carried out at room temperature of 23±5°C, with a constant cross-head speed of 0.07 mm/s, corresponding to a strain rate of $\dot{\varepsilon} = 0.00025\ s^{-1}$. The tests continued until the specimen failed. After the test, each specimen's cross-section was measured using a digital camera.

Based on the recorded force-extensometer signals, engineering stress-engineering strain tensile curves were plotted. Tensile characteristics including percentage elongation after fracture (A), uniform elongation (A_g), tensile strength (R_m), yield strength ($R_{p0.2}$), and percentage reduction of area (Z) were evaluated.

4.3.2 Fracture toughness testing

Miniaturized Compact Tension 0.16T-CT (MCT) specimens were extracted from selected areas of the graded blocks HB and VB. In the case of the fracture toughness test, the resistance of the crack against growth under quasi-static load is measured. Therefore, the decisive factor is the crack plane orientation and crack growth direction within the FGM. Similar to the MTT testing, MCT specimens were extracted in a way that allowed for the measurement of fracture toughness of single material zones, interfaces, and material transitions. The extraction plan for MCT production is depicted in **Figure 7**, (a) and (b), for HB and VB, respectively.

In the case of HB, ZYM and YZS-oriented specimens were extracted for each individual material zone. The crack plane of ZYM-oriented specimens is situated in the horizontal plane (XY). For instance, for single material zone testing, ZYM_3 refers to the specimen with the horizontal crack plane placed in material zone 3 (316L). The example of a specimen with the crack plane situated between single material zones one (316L) and two (IN718), i.e., within a sharp interface, is in the extraction plan designated as ZYM_1-2. The last example and test case is designated as YZS_1-2, which refers to the specimen with the crack growth oriented from material zone 1 across the sharp interface into material zone 2. In other words, it represents the crack growth from material 316L to IN718 across the sharp interface. The three main test cases are the same for VB. The fracture toughness was tested for single material zones, interface planes, and crack growth oriented across the interface. However, due to a different interface orientation (XZ plane), the ZYM orientation refers to crack transition between material zones, while and YZS with XZS refers to interface plane and single material zone located crack growth from bottom to top direction. MCT specimens were not produced, and fracture toughness was not measured for IBs. The designation of the specimen’s orientation follows the standard [2].

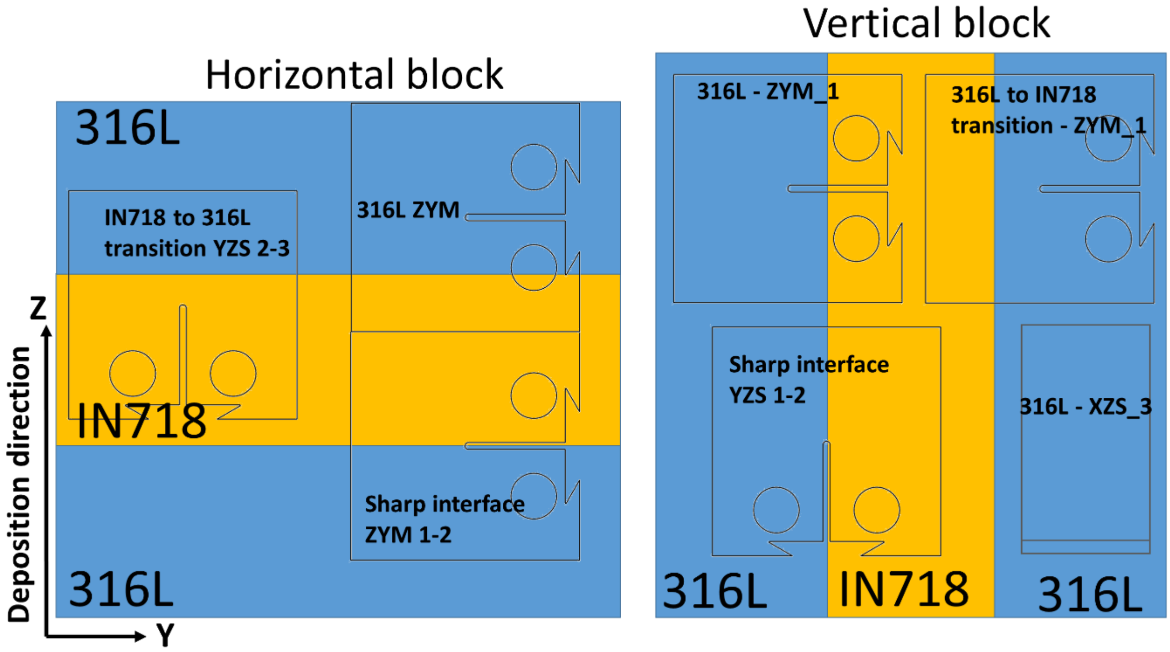

***Figure 7**. MCT specimen’s extraction schema with specific locations and orientations for HB and VB.*

After specimen production, each specimen underwent pre-cracking in fatigue to create a sharp crack. The MCT specimens were prepared through a pre-crack procedure utilizing the magneto-resonant machine Rumul with a load cell capacity of 5 kN. The procedure continued until the crack length-to-specimen width ratio (a/W) reached approximately 0.5. The final pre-cracking loading force was controlled to ensure that the stress intensity factor (K) did not exceed 16 MPa·m$^{1/2}$. Side-grooves, machined on both sides of the MCT specimens to a depth of 10% of the specimen thickness were machined to maintain a straight crack front and reform the stress state at the crack tip. For MCT specimens, a plane stress state dominates the crack tip area during loading, whereas standard specimens transition from plane stress near the surface to plane strain in the middle area due to their thickness. Side-grooves improve the stress state profile of MCT specimens, making them more comparable to standard specimens.

Fracture toughness was measured using the unloading compliance method. During the test, loading and unloading sequences were repeated, with continuous growth of the crack mouth opening displacement (CMOD) of the specimen. Two unloading steps, each at 20% of the actual force level, were performed in each step. Specimen compliance was evaluated based on the unloading slope. Using normalized compliance values, corresponding crack sizes were determined. The J-integral was calculated for each step based on the loading force and crack length. Testing setup is depicted in **Figure 8a** and MCT geometry in **Figure 8b**.

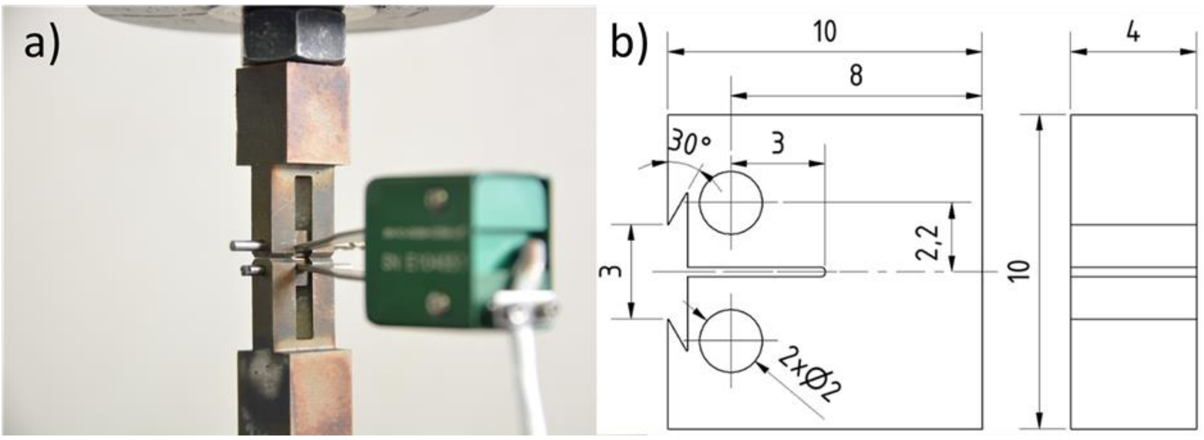

Figure 8. *a) Fracture toughness testing setup; b) MCT specimen geometry.*

Data points representing ductile crack extension (∆a) and J-integral values were plotted on a graph and interpolated using a logarithmic function. The resulting graph represents the energy required for ductile crack growth by a certain distance, known as a J-R curve. Fracture toughness can be evaluated based on the constructed J-R curve, following ASTM E 1820 [146] standard. A blunting line with the slope of the average yield stress and ultimate tensile strength is drawn from the origin of the graph. This blunting line is then offset by 0.2 mm on the X-axis. The intersection of the blunting line and the J-R curve provides a specific J-integral value. These J-integral values can be recalculated as the stress intensity factor parameter, which represents the material's fracture toughness when specific validity conditions are met.

5 Results

This section of the work presents all findings of the experimental investigation of produced materials. Results are divided into five main chapters which are individually dedicated to the results of the structural and mechanical investigation of each produced FGM modification. These are followed by the evaluation of failure mechanism of the two-material interface under the tensile loading.

5.1 Horizontal block results

5.1.1 Horizontal block deposition strategy

In the first FGM modification, a characteristic material distribution was achieved by employing an alternating deposition approach, where one material was deposited on top of the other. This method resulted in the creation of a compositional gradient in the deposition direction. The visual representation of the deposited block can be observed in **Figure 9**. The block itself was deposited onto a platform composed of heat-treated conventionally produced 316L. The deposition process unfolded in the following manner: Initially, a single material zone of 316L was deposited onto a base plate crafted from conventionally produced and heat-treated 316L. The base plate, measuring 100x100x10 mm, was securely affixed to the worktable within the deposition machine's workspace. For each deposited powder layer, the height was adjusted to 250 μm, and the cross-section of the block measured 35x35 mm. As the 316L region attained a height of 5 mm, a layer of pure IN718 was directly deposited onto it until a thickness of 5 mm was achieved. This alternating deposition sequence was iterated until the 7th single material zone had been completed. Following the deposition process, the block was carefully removed from the worktable after it had undergone the necessary cooling phase.

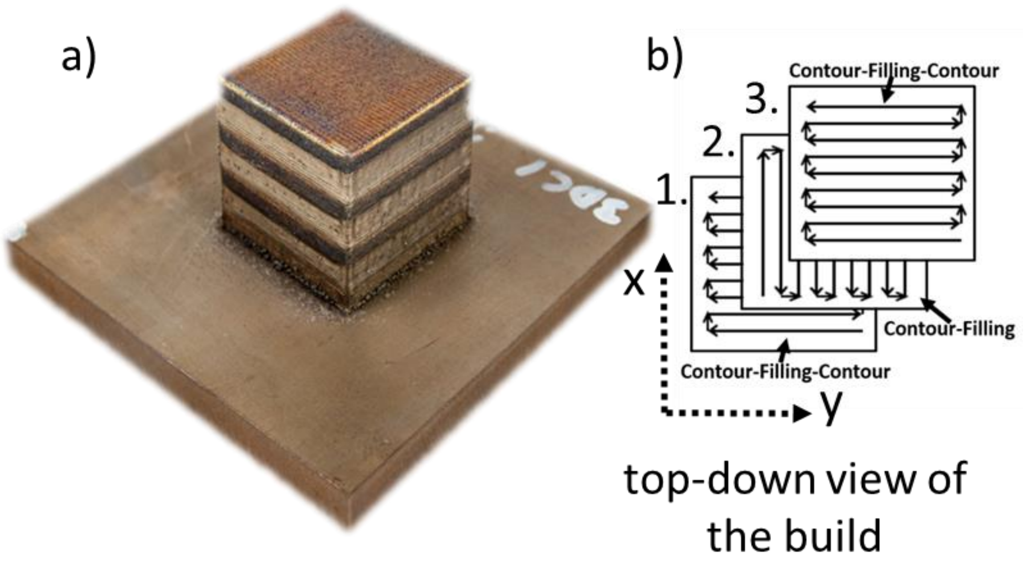

Figure 9. *FGM block with horizontally oriented interfaces between 316L and IN718 referred as HB and schema of the deposition sequences repetition from the top-down view.*

There appears to be a higher concentration of particles on the surface of 316L zones compared to IN718 zones. An elevated number of particles is also observed along the bottom edge of the block and the platform. The overall shape of the blocks is consistently regular, without any unplanned leaning or rounding at the top. The distinct lines of the deposited layers are particularly noticeable in the IN718 zones, which exhibit a cleaner appearance.

5.1.2 Evaluation of porosity of HB

Complex structure of the graded blocks was investigated via Light Microscopy in the vertical YZ plane. Vertical cut through all deposited material zones was performed using WEDM cutting machine in the distance 10 mm from the surface. Image of the examined plane after the metallographic preparation is depicted in **Figure 10**. Detected defects by image analysis are marked by green colour within four measured areas. Areas 1 and 3 contains 0.06 and 0.1 % of defects, respectively. Zones 2 and 4 showed basically free-defect structure. Overall porosity level across all deposited layers was evaluated to be 0.01 %. More than 90 % of observed globular pores were characterized by a diameter below 20 µm.

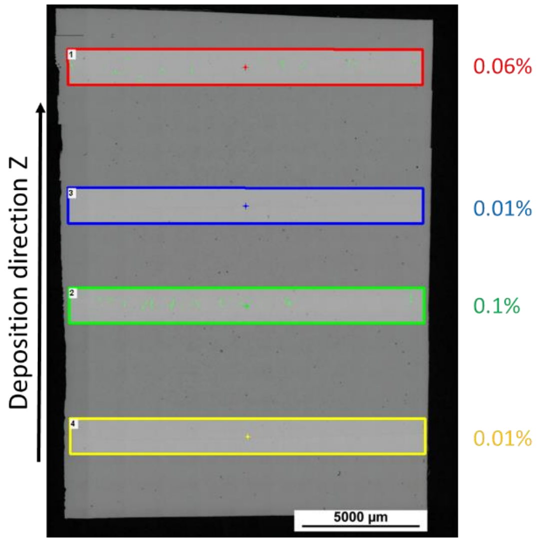

Figure 10. *Image analysis of the defects in the area across the multiple interfaces of HB and within the areas of materials interfaces.*

5.1.3 Light microscope observation of HB

The etched structure of HB is displayed in **Figure 11**, providing insight into the material composition. Through the etching procedure, a clear differentiation between the zones of the base materials, 316L and IN718, is evident. The macrograph of the individual material layers exhibits a compact structure, devoid of significant defects. Beyond the distinct single material regions, the etching process reveals two distinct types of interfaces. Notably, a more discreet distribution of base materials was achieved when IN718 was deposited onto the 316L base. Conversely, a specific transition zone was observed when 316L was deposited on top of IN718. The formation of these differing interfaces appears to be heavily influenced by the distinct temperature intervals of the solidus and liquidus for the steel and nickel alloys. The need for varying laser power due to the disparate melting points plays a crucial role in these interfaces' formation. In the case where the applied laser power for IN718 deposition was insufficient to melt 316L adequately, a sharp interface was formed. This sharp fusion line remains linear and horizontally oriented, highlighting the limited laser penetration during the IN718 deposition process. On the other hand, when depositing 316L directly onto an IN718 layer, partial re-melting of the IN718 layer occurred. This resulted in the presence of melt-pools with mixed chemical compositions and subsequently led to the gradual formation of an interface. Here, visible melt-pool banding indicates varying levels of base material mixture. Equiaxed and columnar dendrite zones are discernible, showcasing their distinct presentations. Notably, cracks spanning multiple melt-pools and grains were observed. Additionally, the direct fusion line between the gradual interface and IN718 exhibits a more curved shape, attributed to the penetration effects of the deposition laser.

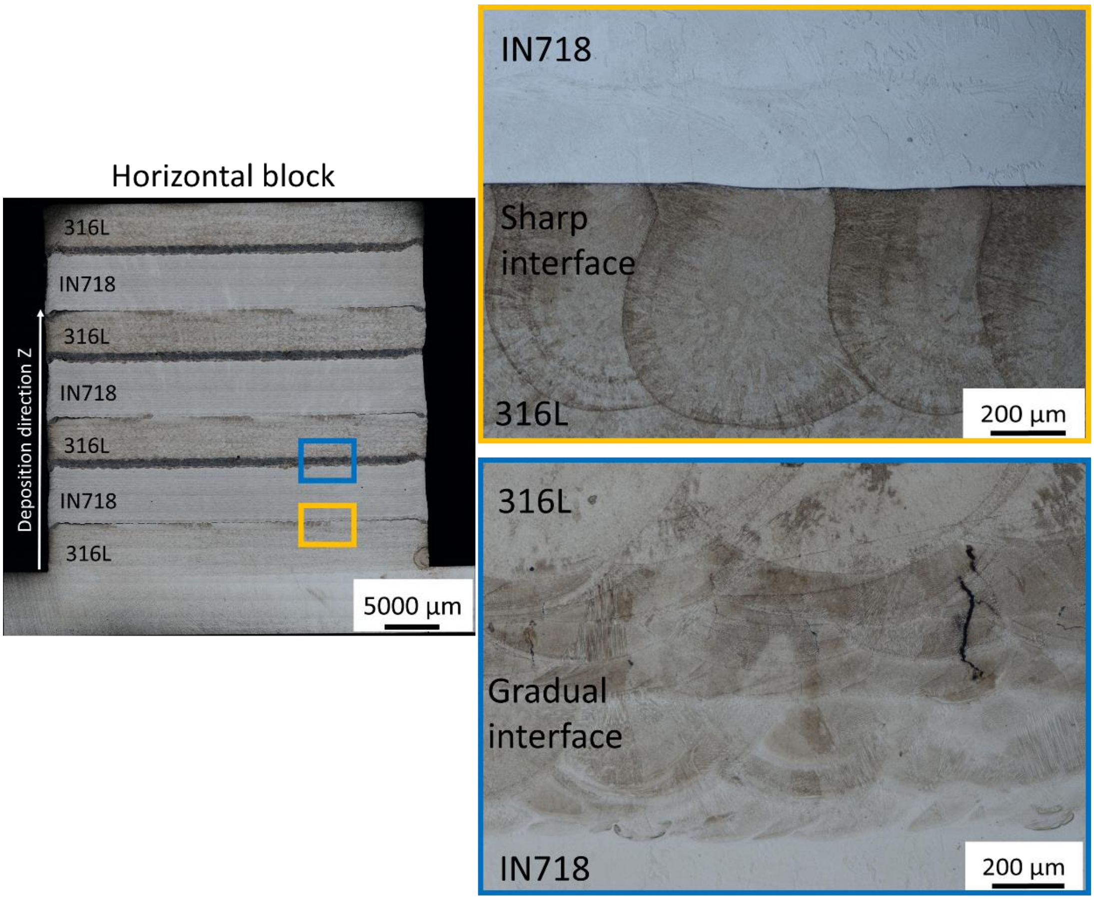

__Figure 11__. Etched structure of the HB with revealed sharp and gradual interfaces between individual materials.

5.1.4 EDS and EBSD mapping of HB

The elemental distribution of the primary elements Fe and Ni at both the sharp and gradual interfaces of HB is depicted in **Figure 12**, with Fe represented by the red colour and Ni by the green colour. The EDS maps provide clear visualization of the discrete elemental distribution present at the sharp interface, where each main element resides within its corresponding material zone. A zone of mixture is evident in the EDS maps for the gradual interface.

These EDS maps are substantiated by EDS line analyses that extend to include Cr and Mo in addition to Fe and Ni in **Figure 13**. The chemical composition remains stable within the first deposited zone for both interface types. Immediately after reaching the fusion line, a decrease in Fe content and an increase in Ni content become noticeable. In the case of the sharp interface, this transition occurs within a distance of 180 μm from the fusion line. However, within the IN718, the Fe and Ni content exhibits less stability than observed in the 316L, with a continuous change spanning an additional 600 μm. Analysing the gradual interface through EDS line analysis reveals a two-step alteration in Fe and Ni content. Initially, at the fusion line, a sudden change occurs corresponding to the region with a mixture of 316L and IN718 melt-pools. Consequently, Fe and Ni content experiences corresponding increases and decreases, respectively. Upon completion of the gradual interface and entry into the 316L zone, Fe and Ni content continues to change in a manner consistent with the initial sudden change. However, this time, the change persists gradually until a stable level is achieved, aligning with the single 316L zone. The content of Cr and Mo remains seemingly stable for both interface types, displaying no observable trend.

Examining the EBSD results of the HB modification for both sharp and gradual interfaces, **Figure 14** showcases distinctive characteristics. Commencing from the 316L zone of the sharp interface, a fine-grain structure characteristic of steel is observed, while on the opposing side of the interface with IN718, coarse grains are evident. In the case of the gradual interface, grains within the mixed zone match the size of individual IN718 zones. Fusion lines for both interfaces are highlighted by yellow dashed lines. A detailed focus on grain orientation reveals that at the sharp interface, IN718 grains exhibit continuous growth. Conversely, when 316L is deposited onto a pre-existing IN718 layer, complete material melting occurs, leading to the formation of a melt-pool material mixture. Consequently, the appearance of crystallographic traceability is infrequent for the new grains at the gradual interface. However, in both interface types, the new grains grow perpendicular to the fusion line. Nonetheless, subsequent deposition of IN718 or 316L alters the grain shape due to the impact of the melt-pool. The acceleration of coarse grain growth in 316L is attributed to the differing thermal conductivities of 316L and IN718. As additional layers of 316L are applied, gradual refinement becomes evident. Examination of the plotted pole distribution on the pole figures uncovers a higher degree of preferential orientation (texture) for IN718 in the studied sample.

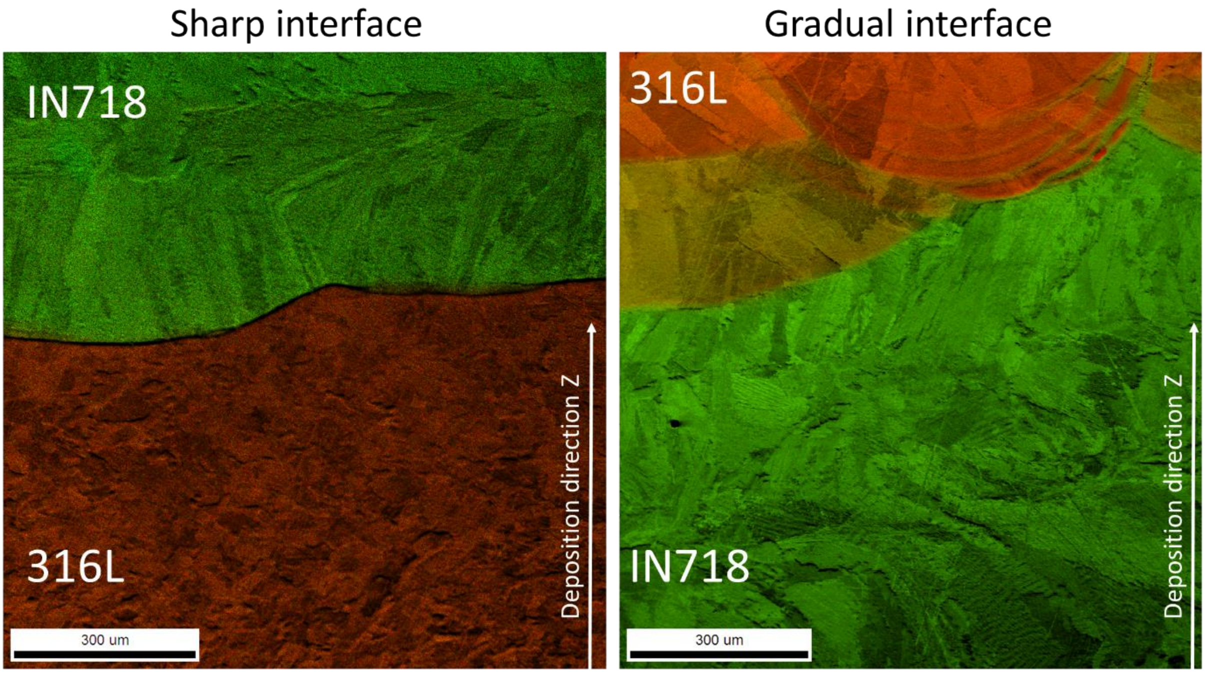

***Figure 12**. EDS mapping of Fe (red) and Ni (green) elements at the two types of interface of HB.*

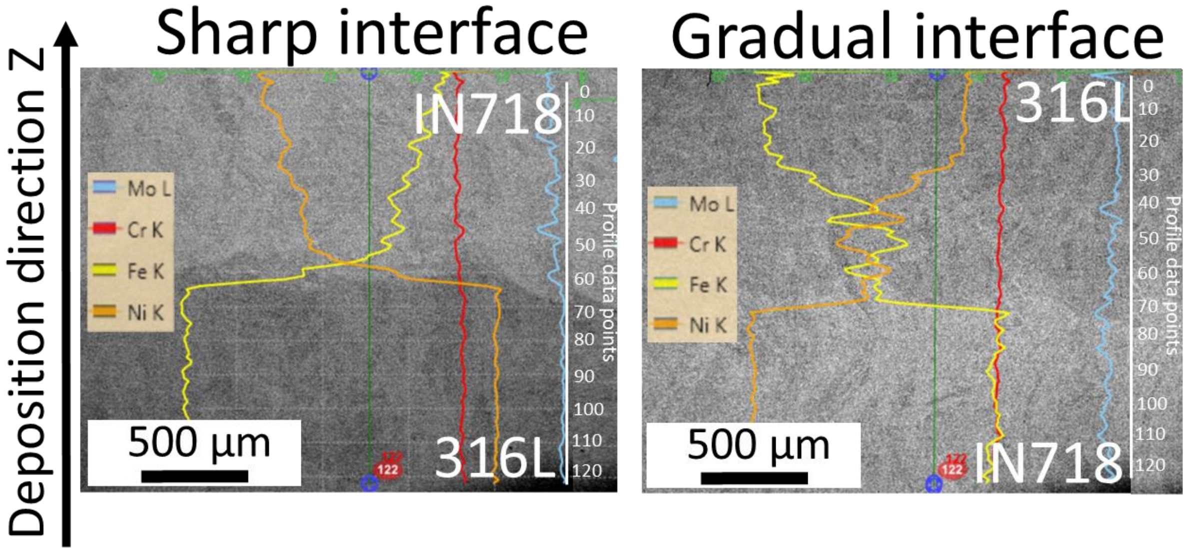

***Figure 13**. EDS line scan across the sharp and gradual interface of HB.*

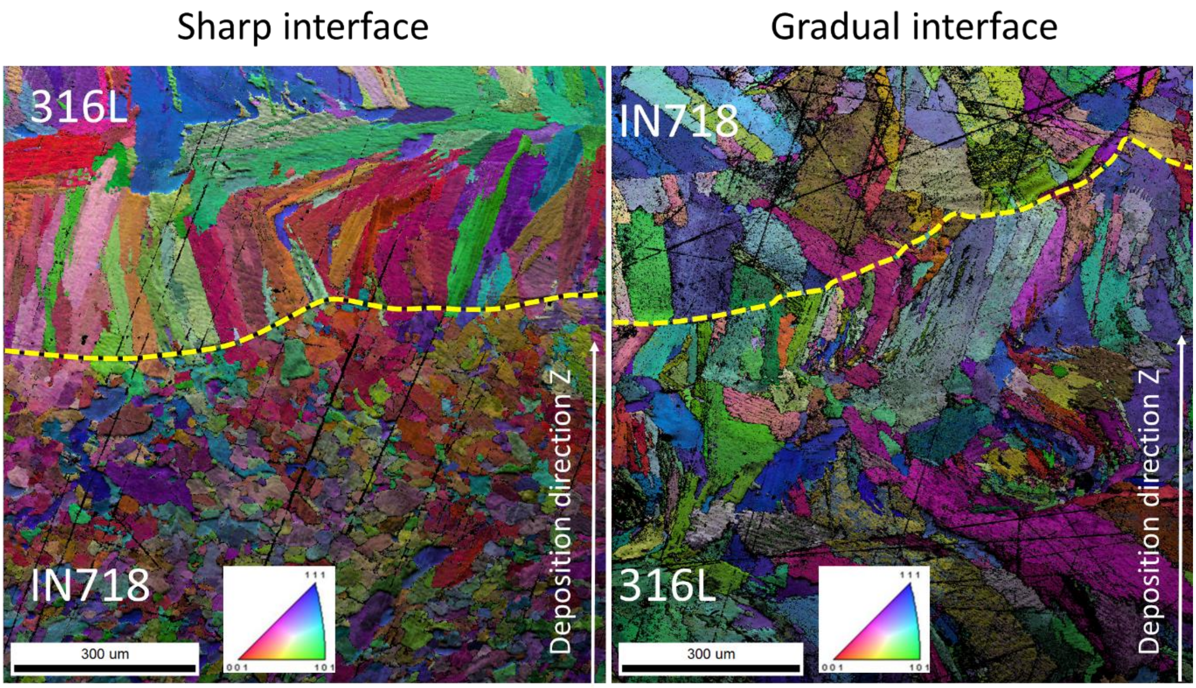

Figure 14*. EBSD images of sharp and gradual interfaces of HB with fusion line highlighted by dashed yellow line.*

5.1.5 Miniaturized tensile testing of HB

In total, over 100 specimens was machined and tested from HB. Representative tensile curves for each significant material section are displayed in **Figure 15**. Column graphs in **Figure 16**, **Figure 17** and **Figure 18** show the average tensile characteristics values per each material zone and interface. The column graphs show great consistency of R_m, $R_{p0.2}$ and A_g and Z for all deposited layer of 316L (1, 3, 5 and 7) in horizontal orientation (XYZ and YXZ). ZYX-oriented specimens showed similar consistency. However, there is two exceptions in the case of zones 3 and 5, where significant drop of R_m was observed. Despite the R_m drop, $R_{p0.2}$ did not exhibit such a value decrease. In the case of IN718 material zones, similar consistency was observed with distinct R_m and $R_{p0.2}$ decrease for ZYX oriented specimens. For both materials the highest tensile values were recorded for horizontally oriented specimens. In the case of ZYX-oriented specimens, the strength decrease might be attributed to the fact that the specimens were crossing the interfaces between single material zones. Where higher concentration of defects might be presented.

Results of at the interface-located specimens are summarized in column graphs in **Figure 18**. Here the brawn colour stands for sharp interface results, green colour represents gradual interface. Pattern of columns depends on the tensile parameter, which is defined by the graph legend. Clearly, R_m and $R_{p0.2}$ are higher for sharp interface across all investigated positions. In terms of specimens orientation, horizontally oriented specimens yielded higher R_m and $R_{p0.2}$, compare to ZYX-oriented specimens. Besides the possible effect of the defects, the probable cause is attributed to the mutual orientation of interface and load. In the case of ZYX-specimens the load is perpendicular to the bonding plane of 316L/IN718. Thus, the strength is dependent on the quality of the bonding. In the case of XYZ and YXZ-oriented specimens, the load is parallel to the load direction and the strength of the interface bonding has lower effect on the measured tensile properties. The trend of engineering tensile curves can be observed in **Figure 15**. The difference in tensile behaviour of vertically and horizontally oriented specimens is evident. While the ZYX-oriented specimen's curve follow the trend of pure 316L. Tensile curves of horizontally oriented specimens lies above 316L, but still below the pure IN718. This is due to the fact, that the arrangement of materials in a tensile sample 316L/IN718 = 50/50 causes the specimens to be strengthen. Thus, the strength value is right between pure IN718 and 316L. However, the elongation is clearly lower, compared to pure IN718. Comparing the two types of interface between each other shows the dominance of a sharp interface, which surpasses the gradual interface in terms of its strength and the achieved deformation to fracture.

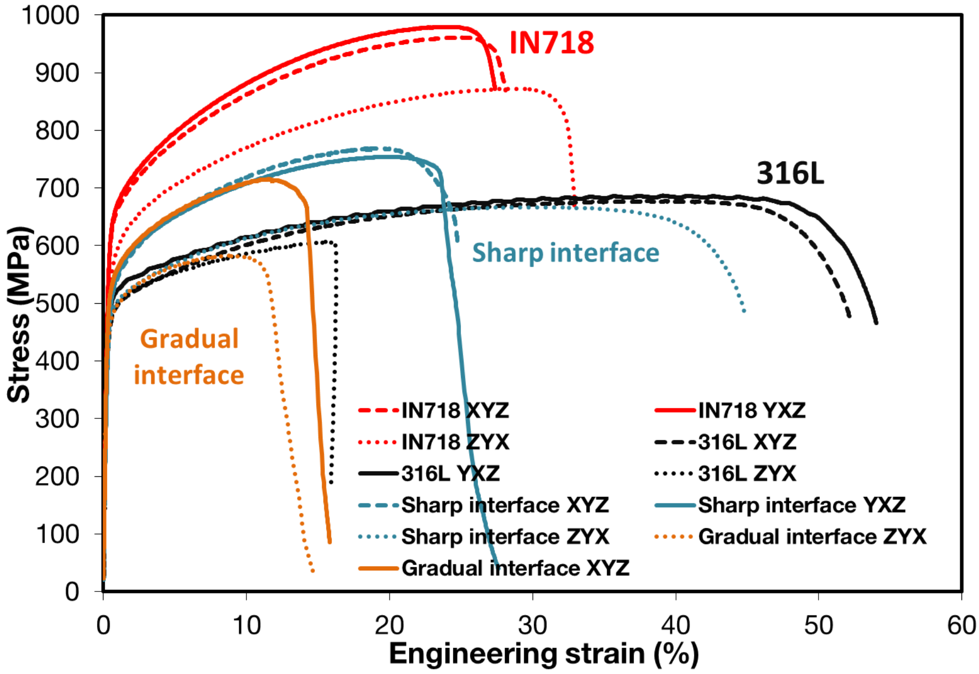

Figure 15. *Representative engineering tensile curves of individual materials and interfaces of HB.*

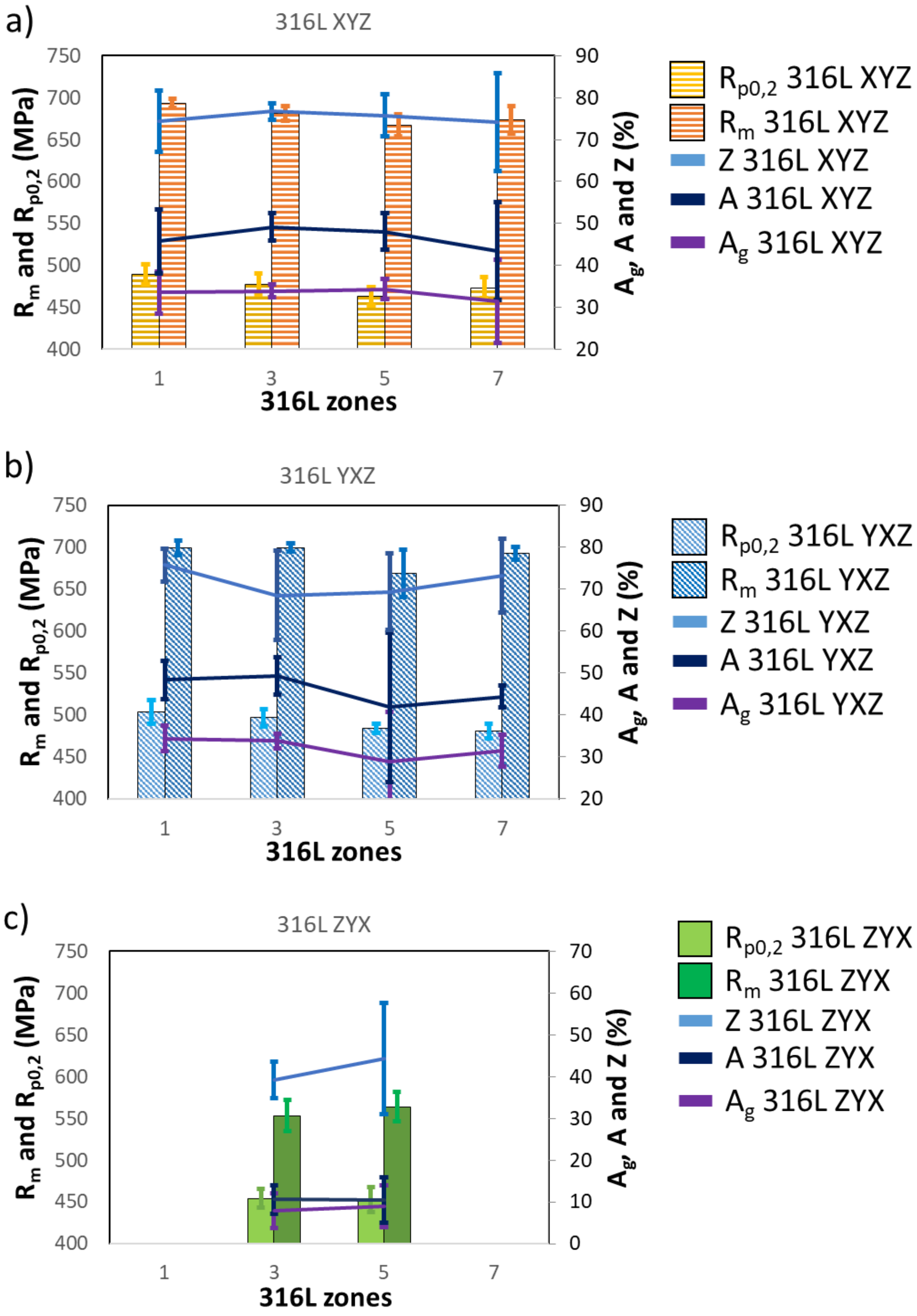

Figure 16*. Column graphs of MTT results of HB for 316L material: a) XYZ-oriented, b) YXZ-oriented and c) ZYX-oriented.*

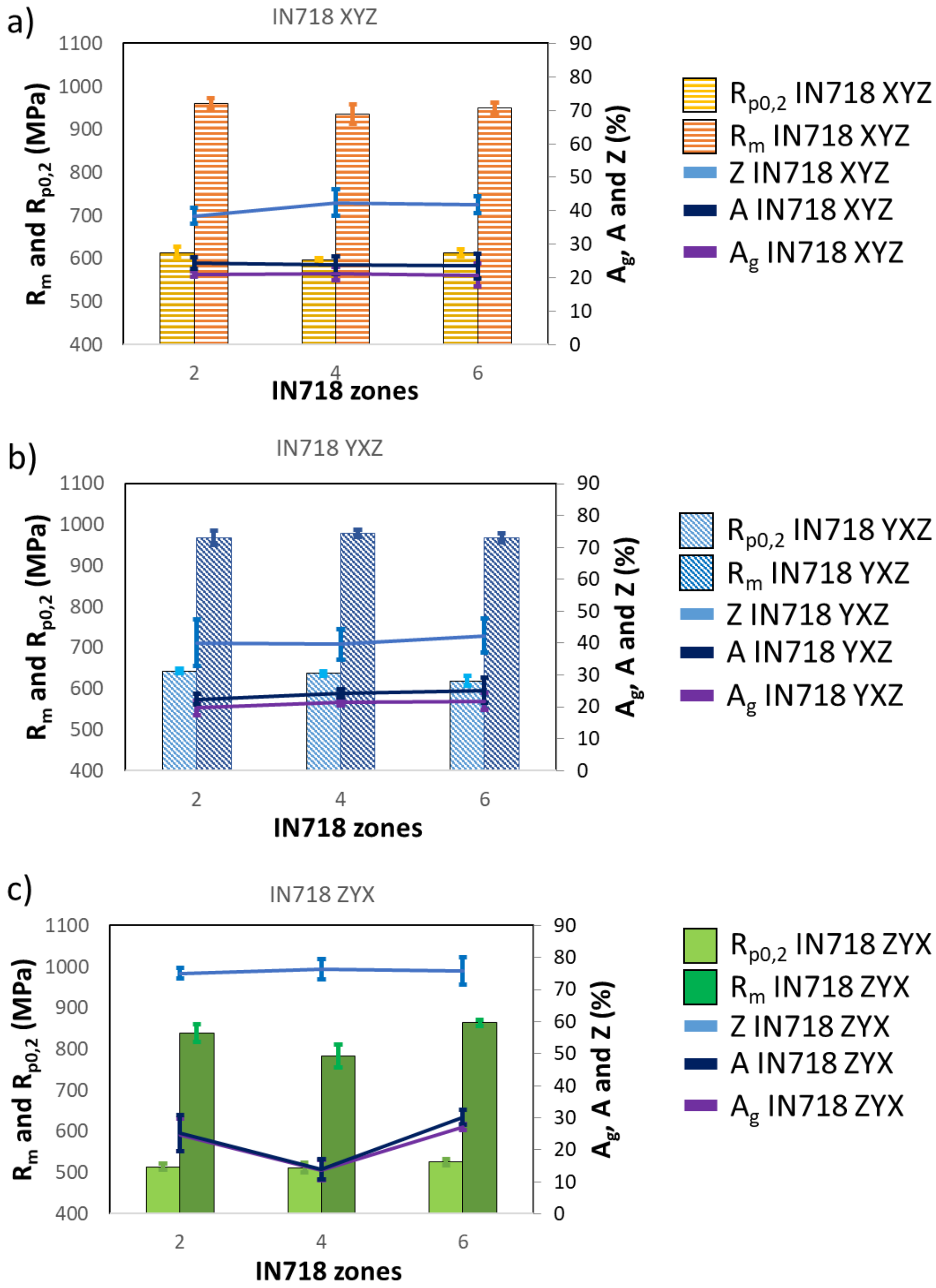

Figure 17. *Column graphs of MTT results of HB for IN718 material: a) XYZ-oriented, b) YXZ-oriented and c) ZYX-oriented.*

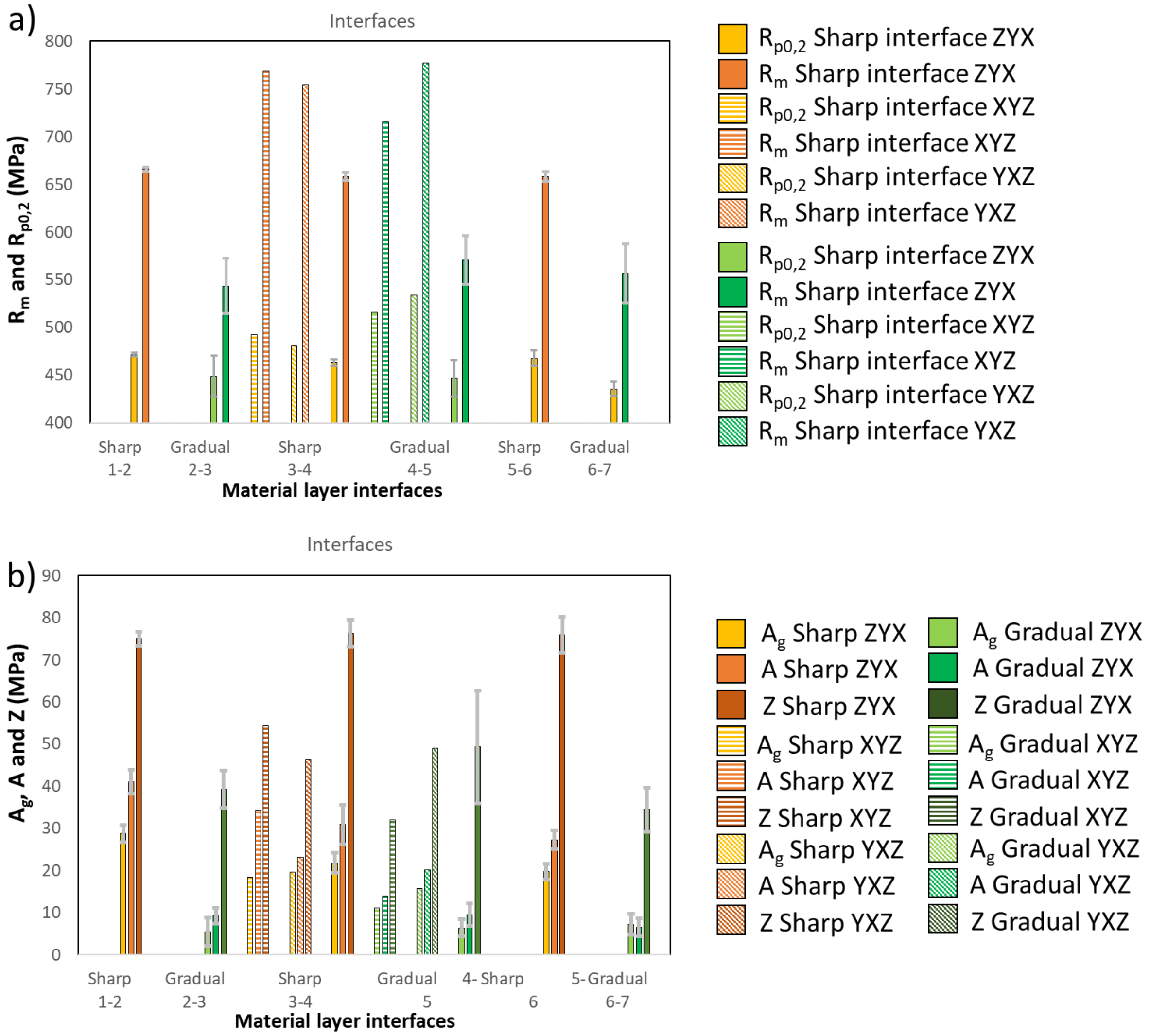

***Figure 18**. Column graphs of MTT results of HB for interface located specimens: a) R_m and $R_{p0,2}$ parameters; b) A, A_g and Z parameters.*

5.1.6 Fracture toughness test of HB

In total, 15 MCT specimens were tested for HB, and 12 were tested for VB. **Figure 19** displays representative J-R curves for all single material layers in HB. The evaluated J_Q, K_Q, J_{IC}, and K_{IC} values for each sample are presented in **Table 6**. A slight anisotropy in fracture behaviour was observed for 316L between the ZYM and YZS orientations. In contrast, IN718 exhibited a higher J_{IC} difference between ZYM and YZS directions, which aligns with the results from MTT, showing higher anisotropy in UTS and YS between YXZ and ZYX orientations.

The fracture behaviour of both single materials did not show any unexpected or unusual events during the test, indicating a low level of structural defects within the single material layers of 316L and IN718. This was further demonstrated by the smooth Force-CMOD records.

J-R curves for sharp and gradual interfaces between layers 3-4 and 4-5 are depicted in **Figure 20**. Despite the significant differences observed in the MTT results for these interfaces, the fracture toughness behaviour of sharp and gradual interfaces was comparable. Additionally, the Force-CMOD records revealed lower crack growth resistance within the interface, as the CMOD increment between unloading steps was non-uniform. Compared to individual material zones, the J-R curves were positioned below both 316L and IN718. Notably, we observed the YZS-oriented crack growth mechanism across the interface. It was shown that as the crack entered the material layer interface, the crack propagation mechanism was influenced by the direction (i.e., 316L to IN718 or IN718 to 316L) and by the type of interface.

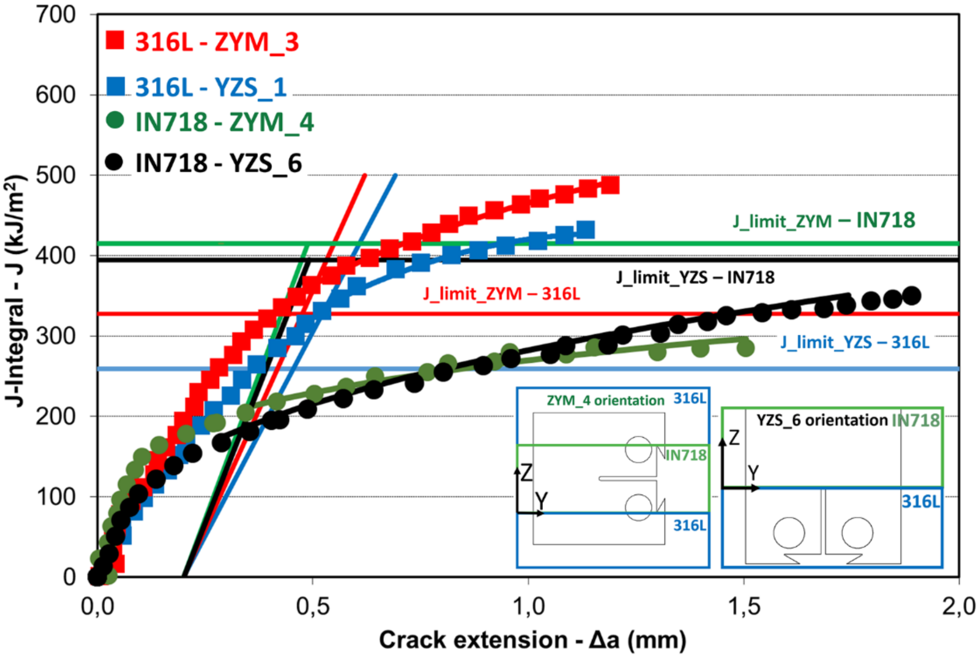

Figure 19. *Summary of J-R curves for single material-located MCT specimens of HB.*

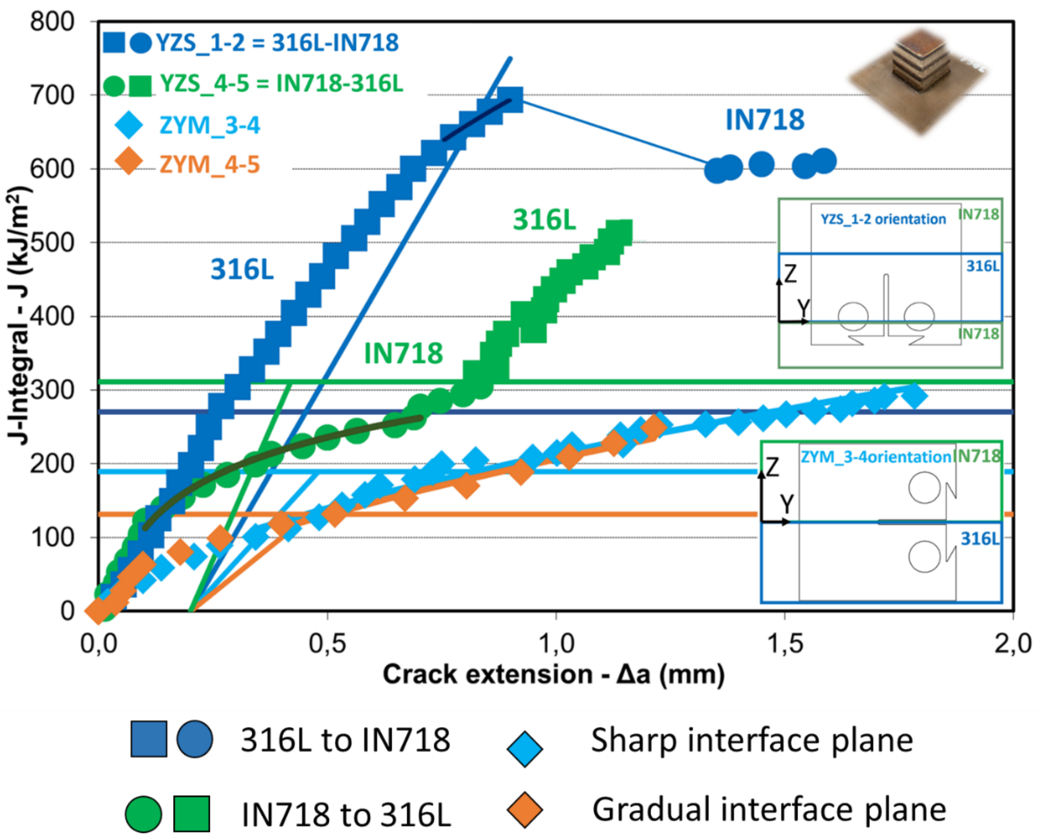

Figure 20. *Summary of J-R curves for at the interface-located MCT of HB.*

Table 6. *Summary of fracture toughness results for HB.*

Material	**Process**	**Orientation**	**K_{JQ}** MPa·m$^{1/2}$	**Ref.**
316L HB	BP DED	ZYM	281±2	[142]
		YZS	268±2	
IN718 HB	BP DED	ZYM	201±3	[142]
		YZS	172±18	
HB sharp	BP DED	ZYM	148	[142]
HB gradual			131	
		XZE	145	

5.1.7 Fractography of MTT and MCT specimens of HB

HB fracture surfaces of MTT specimens for single materials (XYZ) and across the interface oriented (ZYX and YXZ) specimens are depicted in **Figure 21**. Fractures of 316L and IN718 are characterized by a ductile fracture mode with dimple morphology which either follow the dendritic structure of the IN718, or are positioned stochastically in the case of 316L. Fracture surfaces of both materials contain insignificant number of structural defects. On the contrary, fracture surfaces of ZYX oriented MTT specimens depicted in C and D show higher defect concentration. The defects in the case of sharp interface occupy about 2.5% of the fracture, whereas it is 15% for gradual interface. The additional EDX analysis revealed that the chemical composition of the fracture is close to the 316L material. However, for both specimens there is detected higher content of Ni, which is above the initial amount of fed powder composition. For gradual interface fracture the Nb content is approximately 5 % which corresponds to IN718 composition.

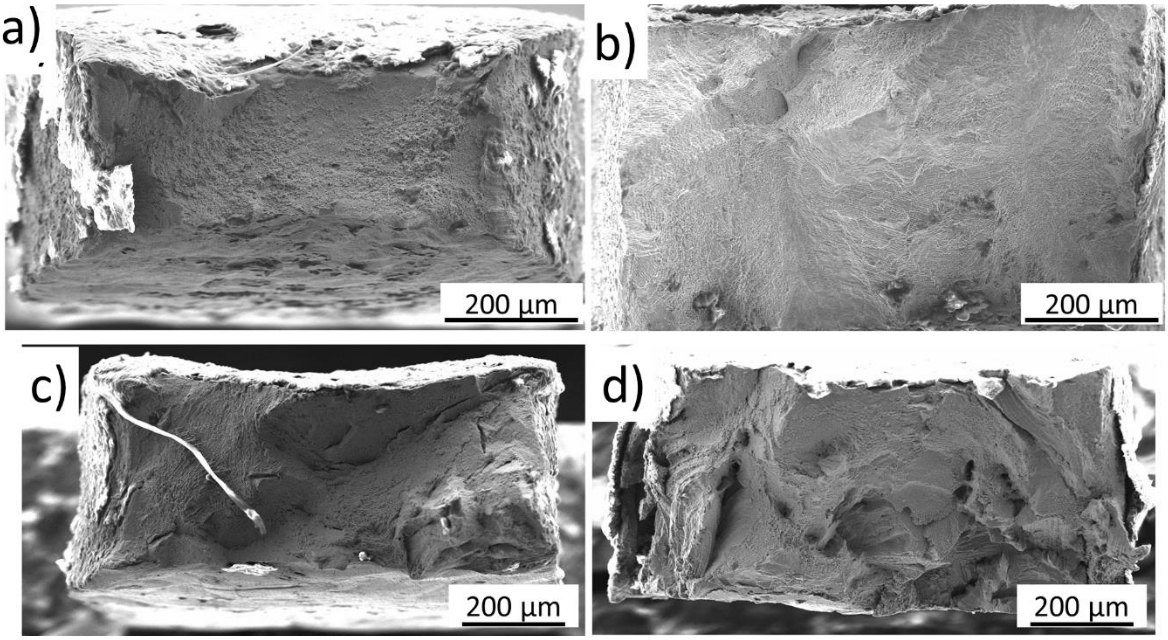

Figure 21*. a) Fracture morphology of 316L-located MTT; b) Fracture morphology of IN718-located MTT; c) Fracture morphology of sharp interface-located MTT; d) Fracture morphology of gradual interface-located MTT.*

Last observation was conducted for XYZ-oriented specimen at the sharp and gradual interface in **Figure 22**. In the case of sharp interface the fracture surface is divided to the two large areas where dimple morphology follows the dendritic structure (IN718 side) or are stochastically distributed (316L). Compare to that, ductile fracture without sharp change of the fracture surface appearance across the specimen was observed for MTT XYZ-oriented specimen of gradual interface. EDS line scan across the thickness of the fracture was conducted. The signal of the element content is scattered as a result of the uneven surface. However, EDS analysis divides the sample into three distinctive areas – one belongs to steel, one to the Inconel and one intermediate seems to be the layer of melt-pools with mixed composition.

Sharp interface XYZ

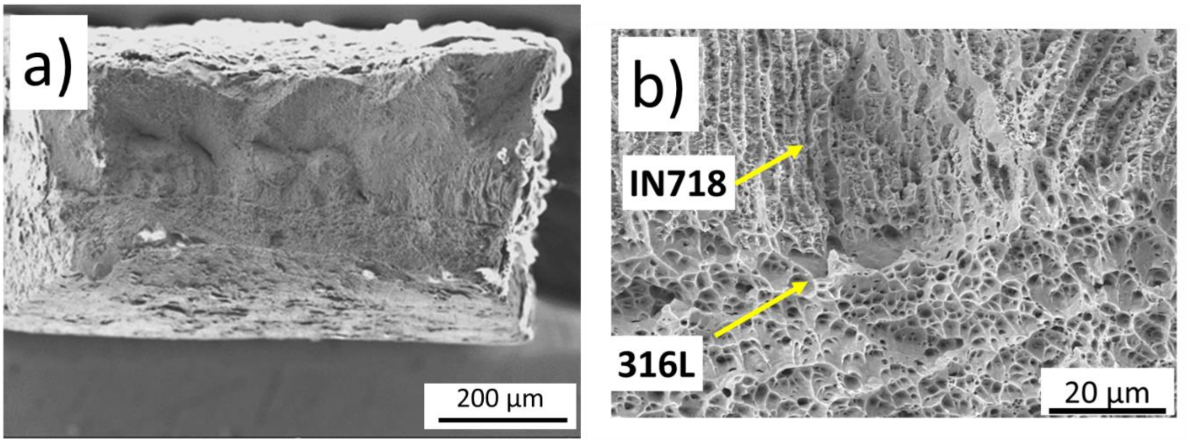

Gradual interface XYZ

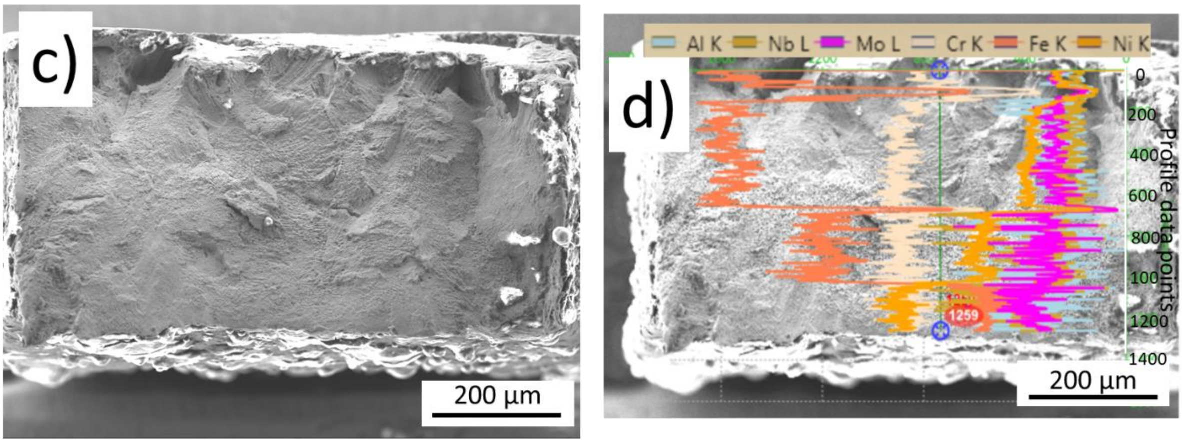

***Figure 22**. a) Fracture morphology of horizontally oriented MTT at the sharp interface; b) detail of fracture morphology transition of sharp interface; c) Fracture morphology of horizontally oriented MTT at the gradual interface; d) EDS line scan analysis of gradual interface located MTT specimen.*

Representative fracture surfaces of selected MCT specimens from HB are shown in **Figure 23**. The fracture surfaces displayed clear, fine dimple morphology as a result of ductile crack growth in 316L. However, distinct structural defects were also visible on the fracture surface due to the lack of fusion during the deposition process. Similar defects were observed on the fracture surface of the IN718 specimen, where dimple morphology was also present. Comparatively, the dimples in IN718 were coarser and followed the dendritic structure of the grains. Aside from localized defects, the fracture surface did not exhibit any inconsistencies. Fracture surfaces of the specimens in which ZYM-oriented crack growth was investigated within both sharp and gradual interfaces were also analysed. The fracture surface of the sharp transition was topographical and inconsistent in appearance, containing numerous structural defects. In contrast, the fracture surface of the gradual transition appeared flatter and lacked distinct structural defects. Additionally, the dimple morphology did not appear as deep or developed as that of the 316L single layer. The fracture surface resulting from crack growth from 316L to IN718 across the sharp interface is presented. A rapid change in fracture mode from fine dimples of 316L to dimples following the dendritic structure of IN718 was observed. The fracture surface resulting from ductile crack propagation from IN718 to 316L through the gradual interface is visualized in Fig. 13. In this case, the fracture surface was more complex. As the crack reached the interface of the IN718 single material layer, smooth zones without specific features were observed (1). The following zone of the fracture surface was characterized by dimple morphology, but the dimples were mainly parabolic (2). At a certain distance from the interface, areas of fine dimple morphology in 316L were visible.

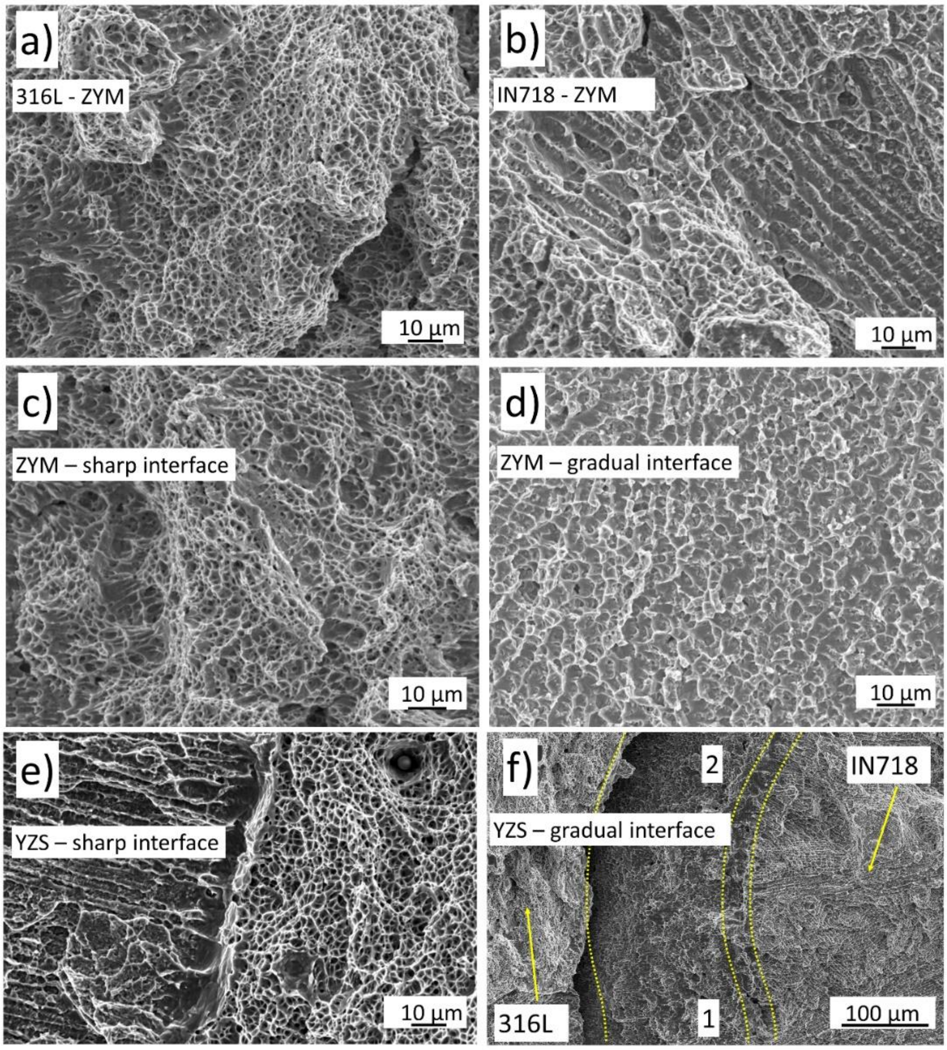

***Figure 23**. Fracture morphology of MCT specimens of HB: a) 316L-located MCT specimen; b) IN718-located specimen; c) at the sharp interface-located MCT specimen; d) at the gradual interface-located MCT specimen; e) from 316L to IN718 crack morphology; f) from IN718 to 316L crack morphology.*

5.2 Vertical block results

5.2.1 Vertical block deposition strategy

The 316L/IN718 block modification designated as VB underwent a rotation of 90°, resulting in a configuration where the interface between 316L and IN718 resided in a vertical plane. The compositional gradient was subsequently oriented in the horizontal direction along the Y-axis. This alteration necessitated a substantial adjustment to the production process, which is outlined in schematic form in **Figure 24**. The revised process entailed depositing each individual material layer alternately from left to right, commencing with 316L, until a height of 250 µm was achieved. This approach was mandated by the need to ensure adequate space for the deposition of the adjacent zone. The deposition of the previous zone at its final height would have rendered it impossible to deposit the subsequent zone, as the nozzle dimensions would not have accommodated the confined space situated between the platform and the material zone's corner. After the initial layer of each material zone had been deposited, the process was repeated iteratively until the final block height of 35 mm was attained.

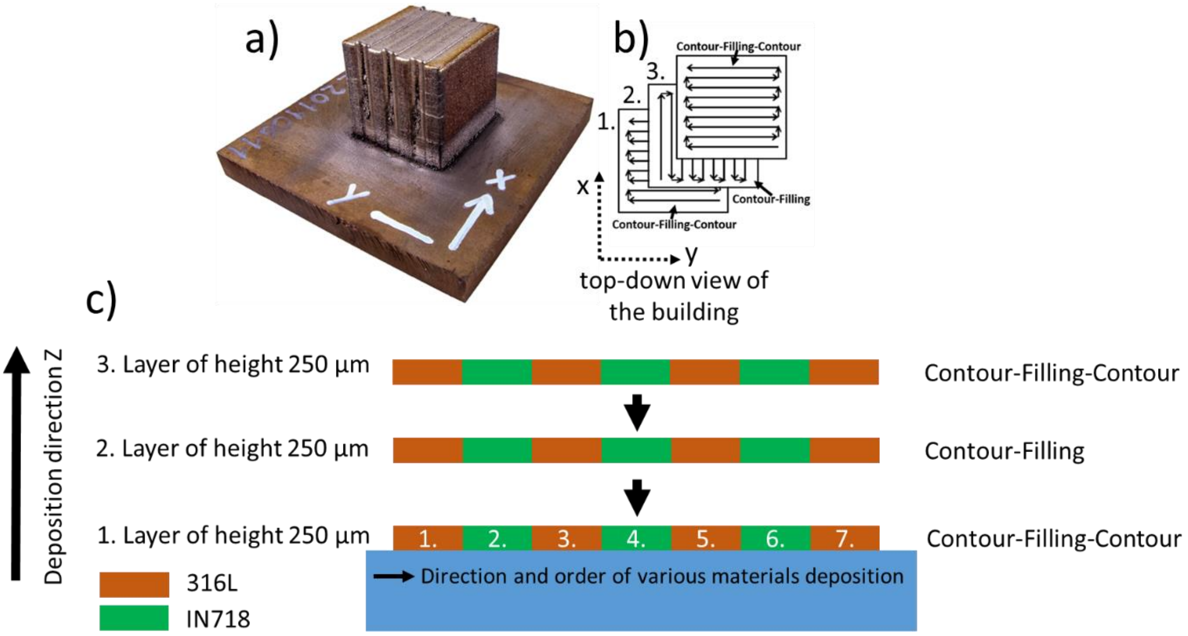

***Figure 24**. a) FGM block with vertically oriented interfaces between 316L and IN718 referred as VB, b) schema of the deposition sequences repetition of each layer from top-down view, c) schema of the deposition process.*

Similarly, the VB block shares these characteristics – a uniform shape, partially melted particles distributed across the surface, visible layering, and clear material boundaries. However, within the IN718 zones of the VB blocks, significant changes in surface topology become prominent starting approximately 10 mm from the bottom. These changes stem from instability in the melt-pool during contour laser scanning, leading to the development of significant surface defects.

5.2.2 Evaluation of porosity of VB

Porosity measurement results of VB are displayed in **Figure 25**. The polished YZ plane of the block showed considerable loss of integrity in the form of cracks. The cracking was observed along the full height of the block in deposition direction. Besides the distinct cracks, globular pores were detected to be distributed regularly across the investigated plane. The higher magnifications (50x and 100x) were used in order to focus on the shape and character of single discontinuities. These defects seems to be aligned in the specific zones in the direction along the different deposited materials. Furthermore, based on the observation, it seems that the defects were regularly oriented. For most of these defects, the angle between the deposition direction and direction of their central axis vary from 10° to 35°. The overall porosity of the cross-section (Area 1) was measured to be 0.45%. Seven cracking zones were measured for porosity individually. The results are presented in **Table 7**. Based on the porosity value zones were divided into two types (A and B). A higher incidence of defects was detected in the type A with average porosity of 2.23%. Zones B showed average porosity of 1.24%.

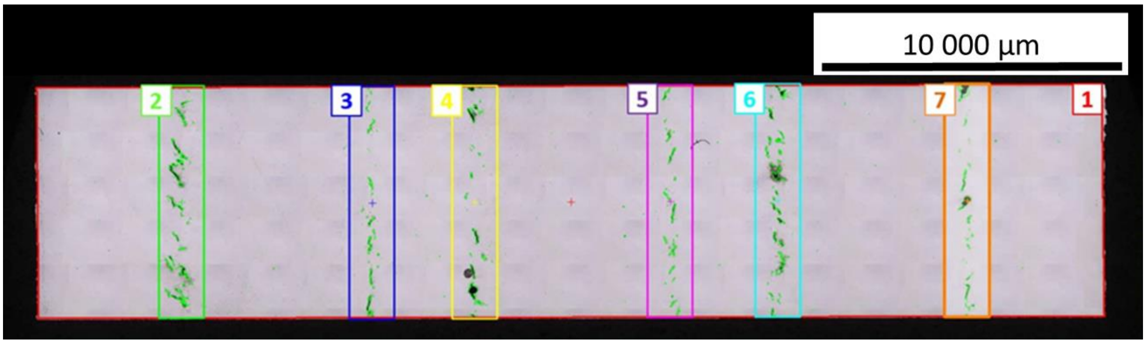

***Figure 25**. Image analysis of the defects in the area across the multiple interfaces of VB and within the areas of materials interfaces.*

Table 7. *Evaluated defects fraction in the individual areas of the VB specimen.*

Porosity measurement area	Interface type	Pore fraction [%]
1	-	0.45
2	A	2.50
3	B	0.97
4	A	2.08
5	B	0.82
6	A	2.11
7	B	1.93
Average	**A**	**2.23**
	B	**1.24**

5.2.3 Light microscope observation of VB

The micrograph of the same specimen after etching is depicted in **Figure 26**. The microstructure of the single material zones of IN718 showcases robust fusion with minimal defects, aside from uniformly distributed globular pores. Conversely, the fusion quality of 316L material bears resemblance to the IN718 zone in the central section delimited by the yellow lines in **Figure 27**. Notably, the etching process unveiled that the previously observed zones of cracking were concentrated within the 316L zone, particularly near its transition to the IN718 single material region. These cracks manifest between the central 316L section and the interface zone. Upon closer examination in **Figure 28** at higher magnification, it's evident that these defects weren't confined to a single 316L melt-pool; rather, they often spanned over two or three pools. Two types of interfaces, denoted as A and B, have been identified based on previous porosity measurements. Both material interfaces exhibit a zigzag pattern resulting from the alternating deposition of base materials. Interestingly, the sequence of base material deposition appears to have a relatively minor impact on interface appearance compared to the HB case. Notably, no distinctly sharp interface was observed. In both deposition orders (316L to IN718 and IN718 to 316L), melt-pools of the respective base materials are observable. Between these individual material melt-pools, regions exhibiting a mixed appearance are marked by yellow dashed lines. Particularly, at interface type B, these mixed zones are situated within the full extent of the melt-pool, whereas in interface type A, they occupy only half of the melt-pool. **Figure 26**, delineated by the red dashed line, highlights the interface region between 316L and IN718. The brightest zones (1) correspond to IN718, while the darker zones

(2) correspond to material 316L. Notably, between them, mixed zones (3) are observable. The material melt-pool type alternates between (1) and (3) within the interface zone along the deposition direction. Further examination of the interface at a higher magnification in **Figure 28** reveals islands with a cellular structure (1) dispersed across various melt-pools. Additionally, islands with a columnar grain structure (2) have formed at the boundaries of 316L and IN718, along with their respective melt-pools. These boundaries are demarcated by dotted yellow curves.

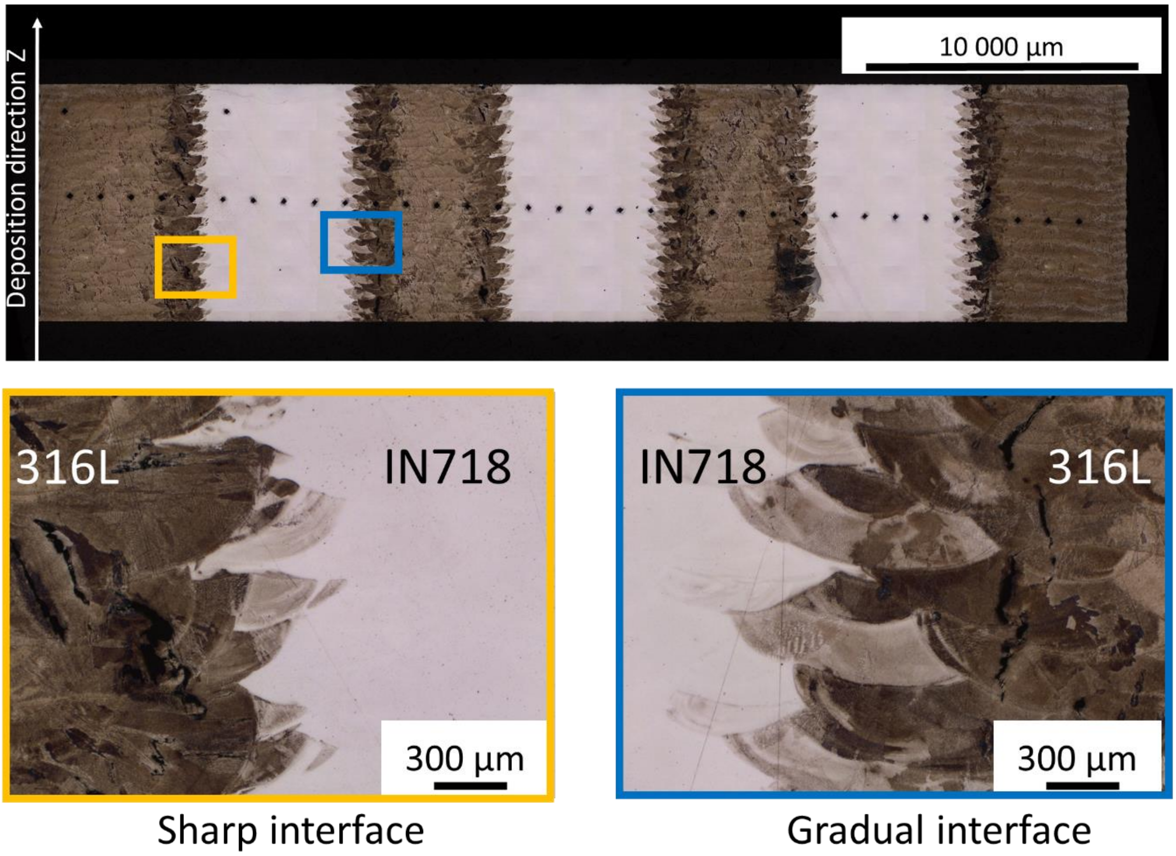

Figure 26*. Etched structure of the VB with revealed sharp and gradual interfaces between individual materials.*

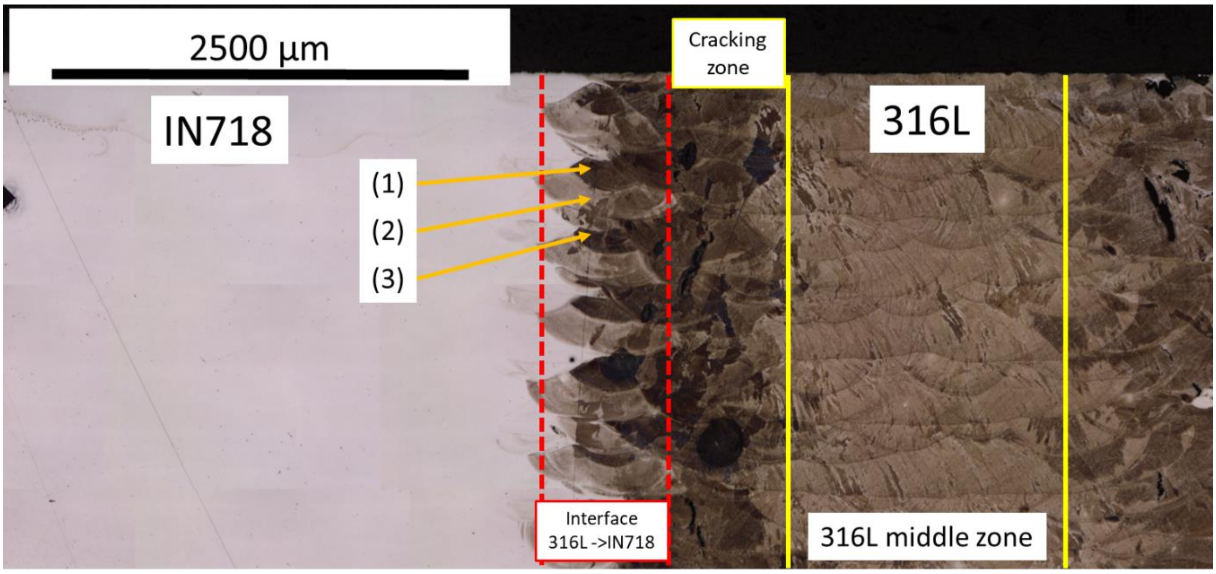

***Figure 27**. Detail of gradual interface of VB with marked 316L zone, cracking zone, and interface zone.*

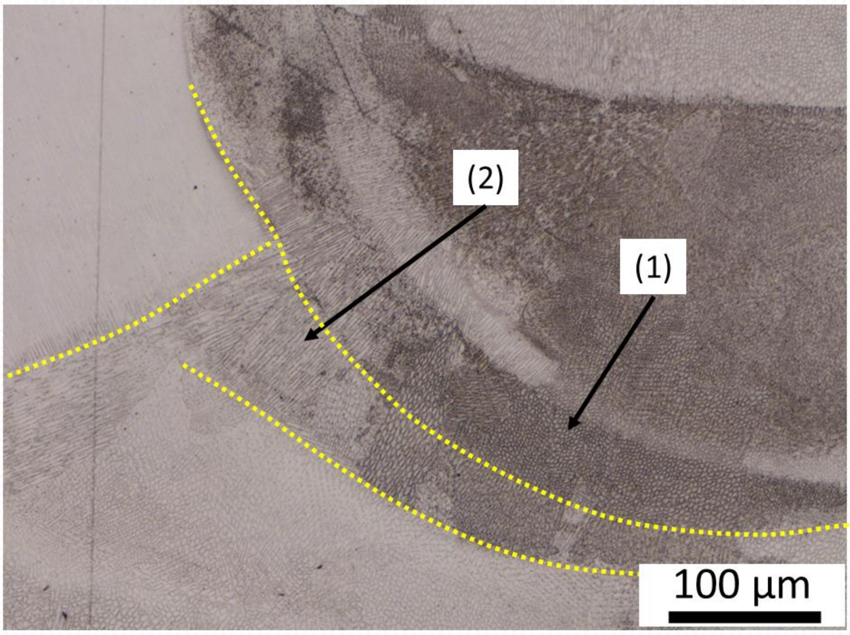

***Figure 28**. Detail of the structure variability within the single melt-pool of VB.*

5.2.4 EDS and EBSD mapping of VB

VB EDS maps of elemental distribution are depicted in **Figure 29**. For both interfaces a distinct fusion line was observed as a border between red field (Fe) and green field (Ni). The fusion line follows the earlier commented zigzag shape of the interface. In addition, Fe and Ni elements were also detected in the zone of their neighbour. Ni and Fe were detected in the distance of 500 µm and 900 µm from the fusion line of interfaces A and B. Furthermore, EDS line scans across the interface were performed and displayed in **Figure 30**. It showed rather sudden change of Fe/Ni content for sharp interface and two-step change for gradual interface.

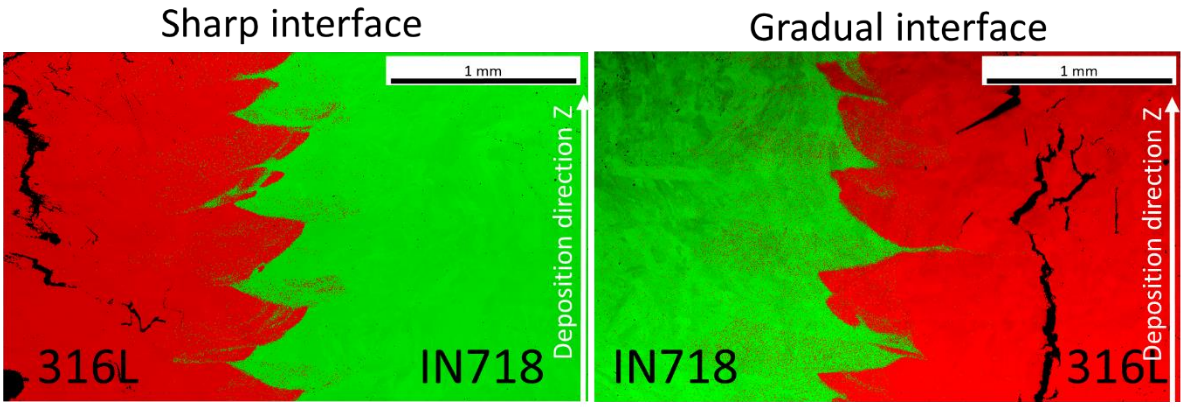

Figure 29. *EDS mapping of Fe (red) and Ni (green) elements at the two interfaces of VB.*

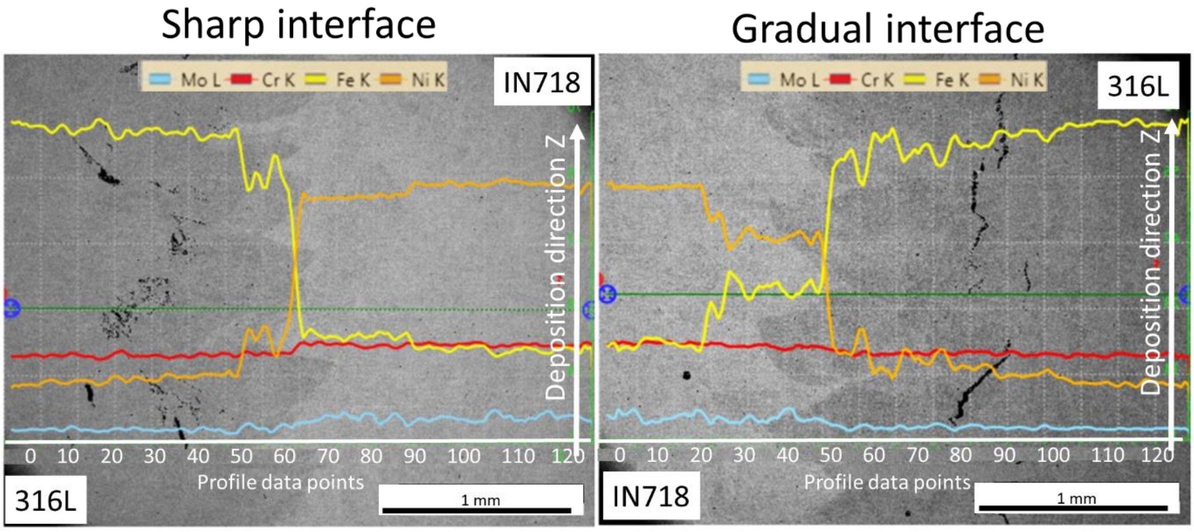

Figure 30. *EDS line scan across the sharp and gradual interface of VB.*

EBSD maps illustrating VB interfaces are presented in **Figure 31**, with yellow dotted lines aligning with the fusion line and discrete elemental distribution as presented in EDS maps. Examining interface type A, the 316L region reveals mostly coarse grains characterized by a lack of preferential orientation and elongation predominantly in the direction of deposition. Additionally, intergranular cracks were identified in the 316L area for both interface types. For interface type A, the grains of deposited IN718 generally mirror the original orientations of the 316L grains. Notably, an intriguing grain pattern in the IN718 emerges in proximity to interface A. Prominent large grains exhibiting the (111) orientation and twisted configurations are formed along the material boundary (1). Adjacent to these distinct curved grains, rapid refinement zones of IN718 grains are evident (2). Further from zone (2), coarse IN718 grains develop alongside smaller columnar grains. Shifting focus to interface type B on the IN718 side, a combination of coarse and fine columnar grain zones is notable. At the sharp transition point between materials, certain formed 316L grains exhibit the same crystallographic orientation as the IN718 grains on the opposite side. However, in specific areas at the sharp interface, new columnar, smaller 316L grains emerge with differing orientations. Progressing further from the boundary on the 316L side, exclusively coarse 316L grains form. Notably, intergranular cracks are observed in the pure 316L area (3). For both interface types A and B, a comparable trend of continuous grain growth across the sharp material boundary is evident. Some of the larger grains extend across the boundary (1), while the size of smaller grains is usually influenced by the interface (2).

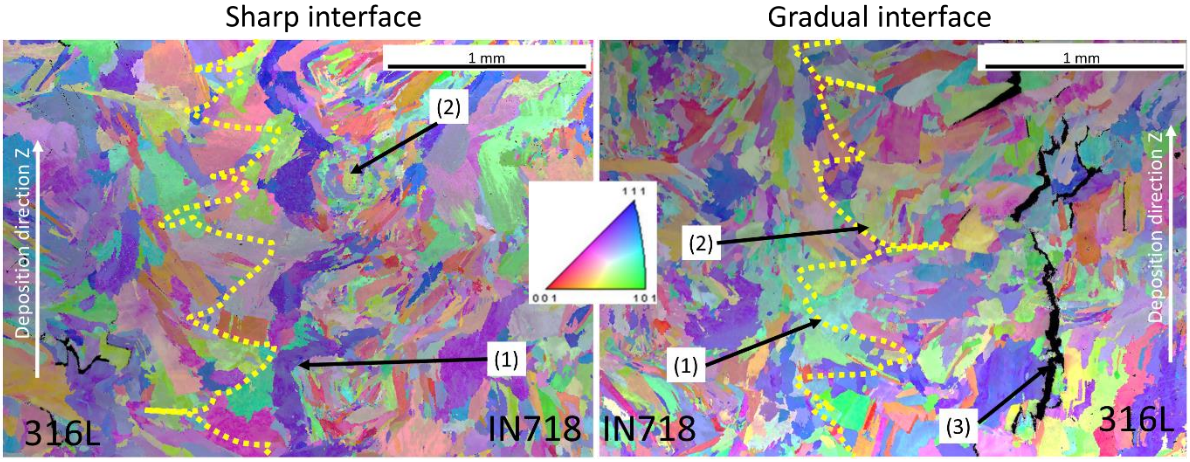

***Figure 31**. EBSD map of grain distribution and orientation across the two interfaces of VB with fusion line marked by yellow dotted line.*

5.2.5 Miniaturized tensile test results of VB

Figure 32 presents representative tensile curves for each domain material zone. The tensile results of VB are summarized using a similar approach as for HB. Column graphs in **Figure 33**, **Figure 34** and **Figure 35** provide a comparison of the main tensile characteristics for 316L, IN718, and the interfaces. In this case, only ZYX and XZY-oriented specimens were statistically evaluated, while YZX-oriented specimens within a single material zone were included only in the representative tensile diagram due to the significant impact of defects. A consistent and stable tensile behaviour was observed for both 316L and IN718 zones across all deposited layers in terms of strength and elongation.

As mentioned earlier, the material response to the tensile load was notably distinct for YZX-oriented specimens. As depicted in **Figure 32**, all specimens exhibited considerably poorer tensile properties, both in terms of strength and elongation, when oriented in the YZX direction, regardless of their position within a single material zone or interface. These YZX-oriented specimens reached approximately 50% of the tensile strength and around 20% of the elongation values compared to other orientations. Generally, $R_{p0.2}$ and R_m ranged from 225 to 325 MPa and from 255 to 375 MPa, respectively. Interface type A (sharp) yielded slightly higher $R_{p0.2}$ and R_m values compared to interface type B (gradual). However, the repeatability of the evaluated values was notably lower compared to the single material zones. This can be attributed to the presence of random defects, which critically affect the integrity of the MTT specimens. From this perspective, it's challenging to draw a definitive conclusion regarding whether the diffusion of elements and melt-pool geometry at the interface significantly influence the tensile properties.

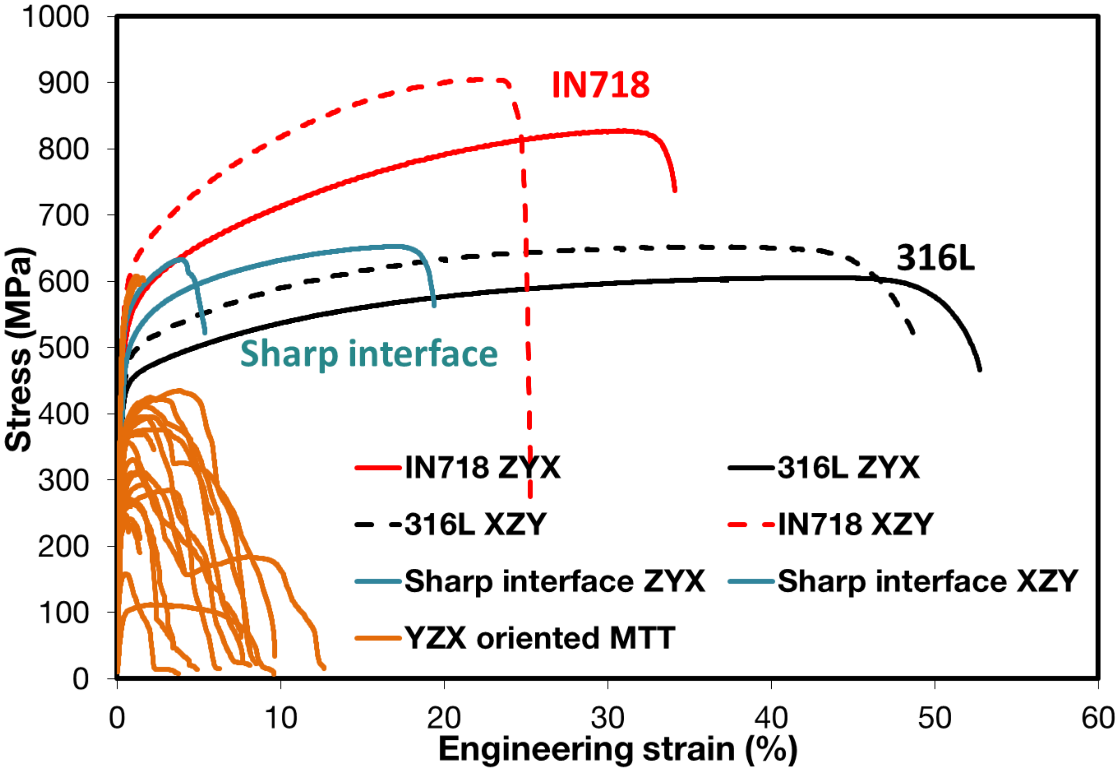

***Figure 32**. Representative engineering tensile curves of individual materials and interfaces of VB.*

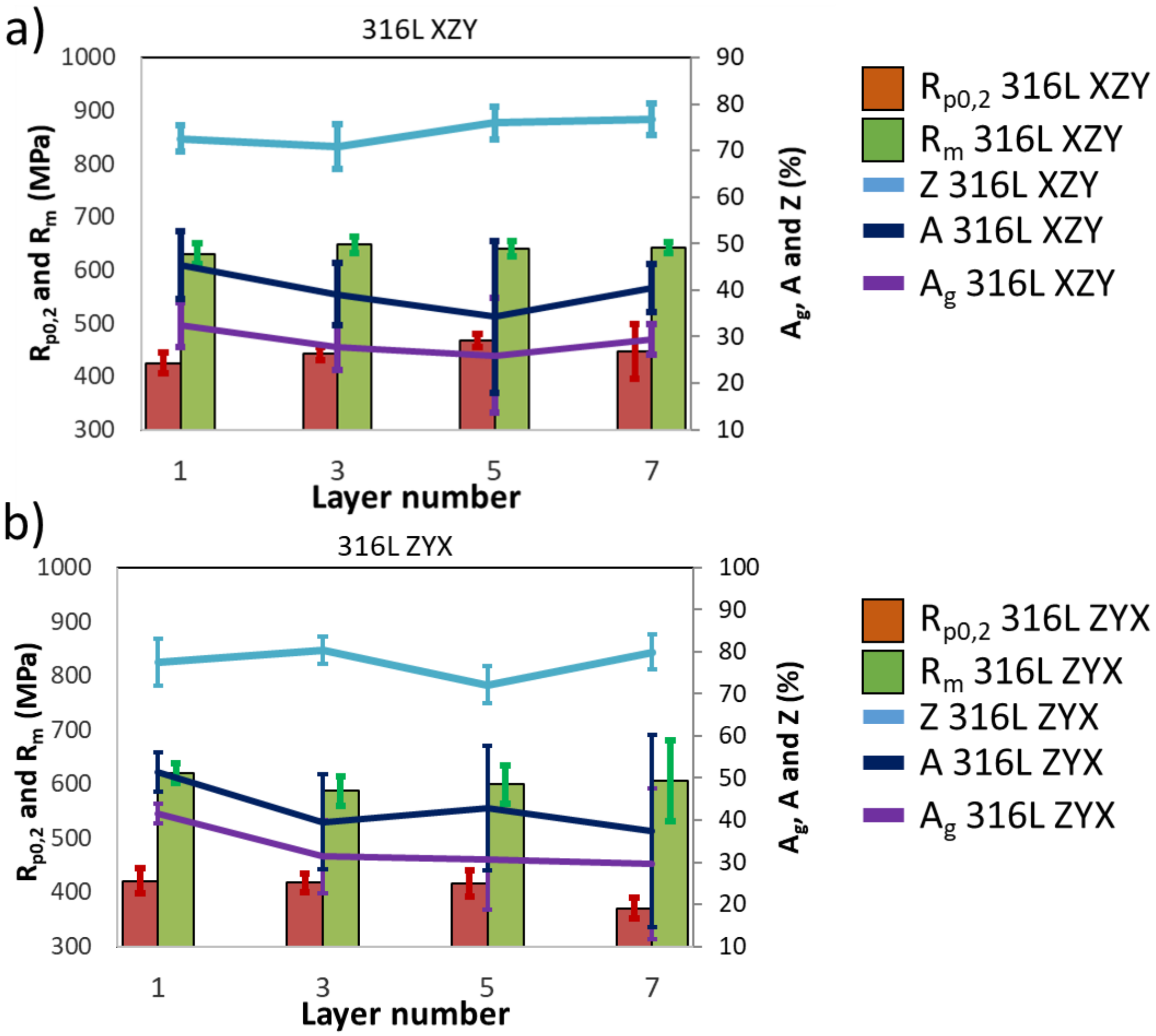

***Figure 33**. Column graphs of MTT results of VB for material 316Ll: a) XZY-oriented, b) ZYX-oriented.*

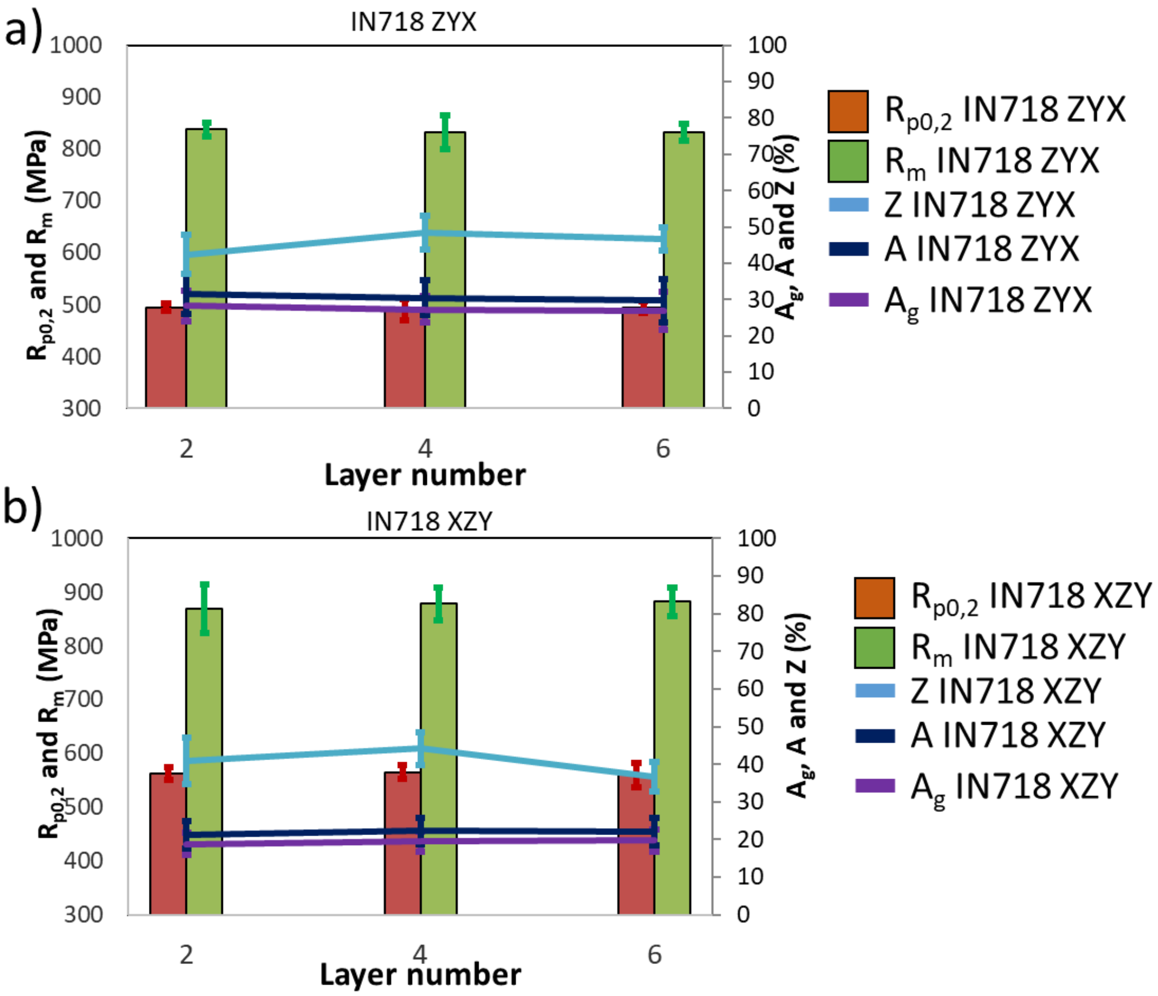

***Figure 34**. Column graphs of MTT results of VB for material IN718, a) ZYX-oriented, b) XZY-oriented.*

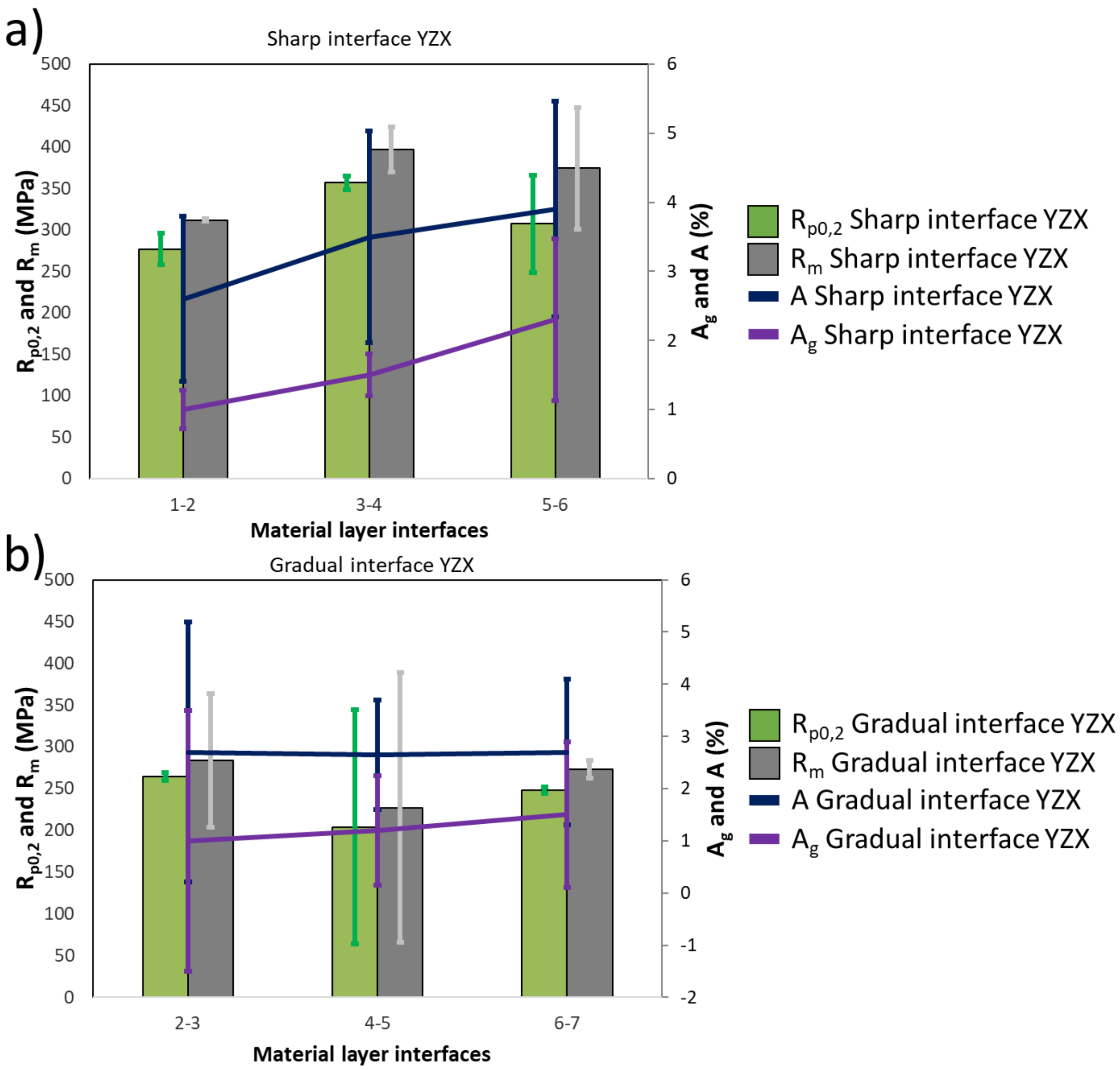

***Figure 35**. Column graphs of MTT results of VB for interface located specimens: a) Sharp interface YZX-oriented, b) Gradual interface YZX-oriented.*

5.2.6 Fracture toughness test results of VB

Fracture toughness results for VB specimens are displayed in **Figure 36**. The results for single material layers showed similar crack growth resistance as for HB specimens. A slight difference in fracture toughness between HB and VB was observed for IN718. However, it's essential to consider the different crack growth directions and orientations of the specimens. HB represents crack growth in a horizontal plane, while VB represents a vertical plane. A rapid drop in fracture toughness was observed for specimens located at the interface. This observation aligns with what was noted for HB. However, the decrease for VB seems to be more rapid in interface fracture behaviour. Evaluated fracture toughness values are summarized in **Table 8**.

Despite the production and testing of specimens with crack growth oriented across the interface, the results could not be evaluated due to the presence of significantly developed defects, as reported in the earlier sections of the thesis.

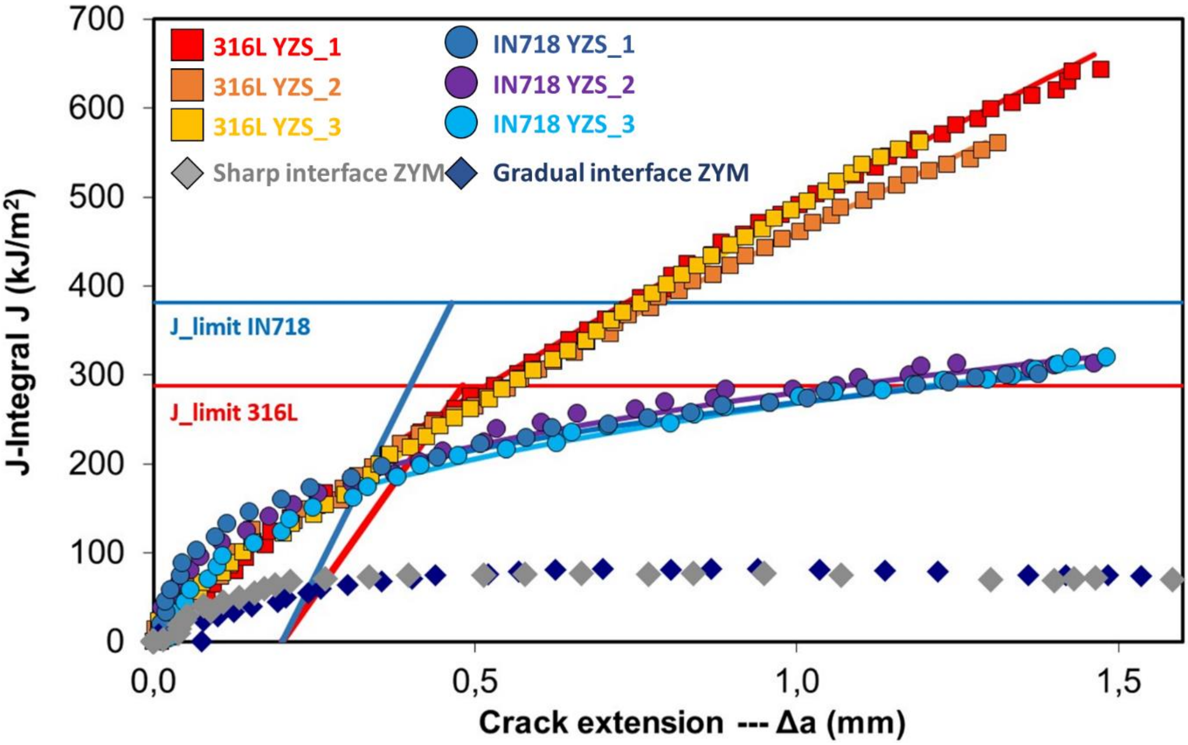

Figure 36. *Summary of J-R curves for single material-located and interface-located MCT specimens of VB.*

Table 8. *Summary of fracture toughness results for VB.*

Material	**Process**	**Orientation**	**K_{JQ}** MPa·m$^{1/2}$	**Ref.**
316L VB	PB DED	YZS	**231±7**	[143]
IN718 VB	PB DED	YZS	**212±8**	[143]
VB Sharp	PB DED	ZYM	114	[143]
VB gradual			125	

5.2.7 Fractography of MTT and MCT specimens of VB

Comprehensive fractography of MTT specimens from VB was conducted for representative specimens of XZY and ZYX of single material zones and YZX-oriented specimens of single material zones and interface areas. Representative specimens fracture surfaces are displayed in **Figure 37a-f**. EDX chemical analysis was conducted to verify the location of the specimen failure. The fracture surfaces of the analysed samples in the X and Z directions are indicative for a high-energy trans crystalline ductile fracture with dimpled morphology. The shape of the fracture surfaces also shows relatively pronounced percentage reduction of area, indicating good plasticity of both materials. Fractographic analysis of YZX-oriented specimens revealed that all specimens in this testing direction exhibit the presence of solidification cracking (SC), which propagated along the grain boundaries, having a detrimental effect on the quality of the interface between 316L and IN718 materials and vice versa. The areas marked with a dashed red line highlight the presence of ductile material failure, the rest of the fracture area had the character of SC. The presence of the areas of SC was a regular feature of YZX-oriented MTT specimens due to the fact that the specimens were placed across the cracking zone in close proximity of 316L material zones. The surface of the defects clearly shows smooth, rounded features indicative dendritic nature of SC fracture surfaces. In the case of SCs, EDS analyses determined that material failure occurred in all cases in 316L material. The presence of ductile failure with dimpled morphology was also observed to varying degrees on the fracture surfaces.

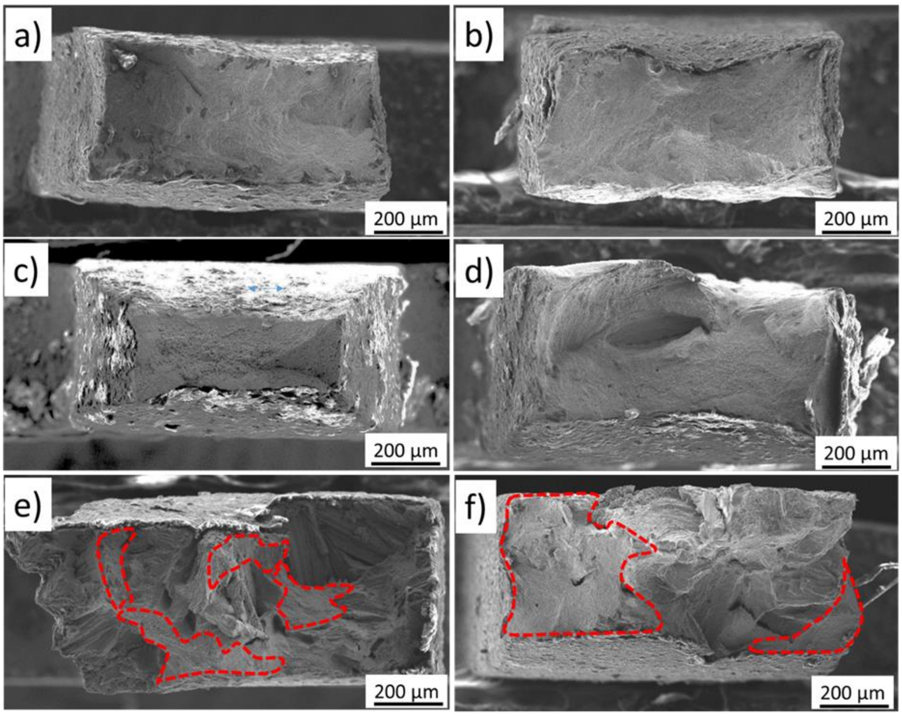

***Figure 37**. SEM images of MTT fracture surfaces with red marked areas highlighting the presence of ductile material failure and solidification cracking areas: (a) XZY IN718, (b) ZXY IN718, (c) XZY 316L, (d) ZXY 316L, (e) YZX 316L, (f) YZX IN718.*

Figure 38 shows an overview of fracture surfaces of MCT specimens for VB modification. It is clearly visible, that the 316L surface exhibit distinct defects, which were observed to be present in the structure. On contrary to that no defects could be seen on the surface of IN718. Enormous number of defects occupied crack plane of MCT specimens with crack located at the interface. However, considering the cracks position in the VB block, which were observed to be in the zone of 316L, it means the crack growth direction was deflected to the plane occupied by these defects. This is visualized in **Figure 39**, where two half of tested MCT specimen are putted together. Since the crack grows in the direction along which the maximum potential energy is released [147]. The pre-defined crack growth direction was changed, due to a large number of cracks in the structure. This gives the explanation on the significantly poor fracture resistance of the interface of VB block that was evaluated. Fracture surface of ZYM oriented MCT with the crack growing across the interface did not showed any similar fracture characteristic as were observed for HB. This is probably due to the enormous SC that were presented in the MCT specimens and significantly affected the crack growing process during the loading. Another reason might the fact that the zone of mixed chemical composition is quite wide for the VB interfaces. Thus, the observation is similar to the MTT Fractography for HB, where gradual interface was not discernible using the visual features of the fracture.

The fracture surface of the ZYM-oriented MCT specimen with the crack growing across the interface did not exhibit any visible transition between 316L and IN718 fracture mechanism, visible in HB. This difference is likely attributable to the presence of extensive SC in the MCT specimens, which significantly influenced the crack propagation process during loading. Another possible contributing factor may be the relatively wide zone of mixed chemical composition in the VB interfaces. Consequently, this observation aligns with the MTT Fractography results for HB, where the gradual interface was not discernible based on the visual features of the fracture.

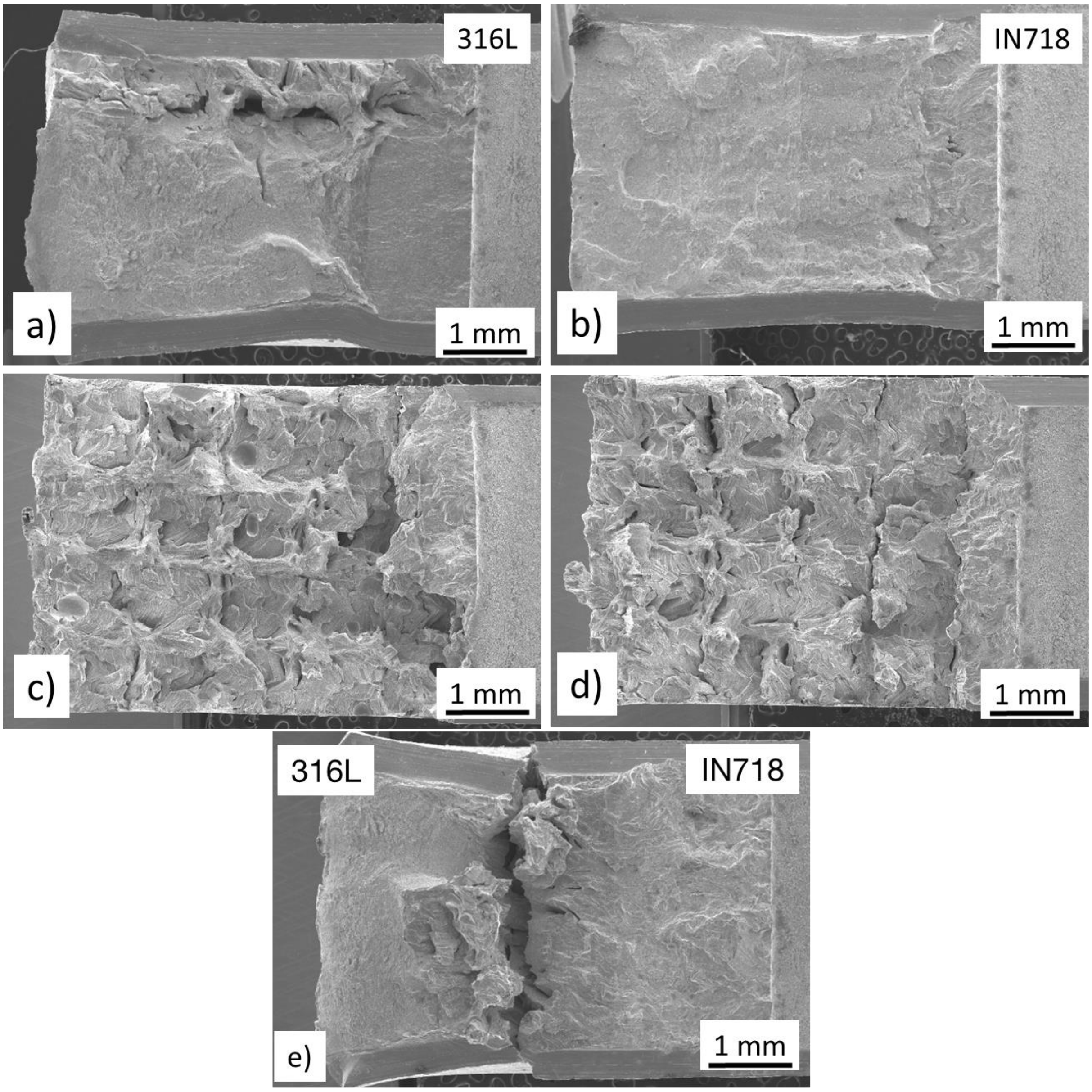

Figure 38. *Fracture morphology of VB MCT: a) 316L, b) IN718, c) Interface sharp, d) interface gradual, e) transition from IN718 to 316L.*

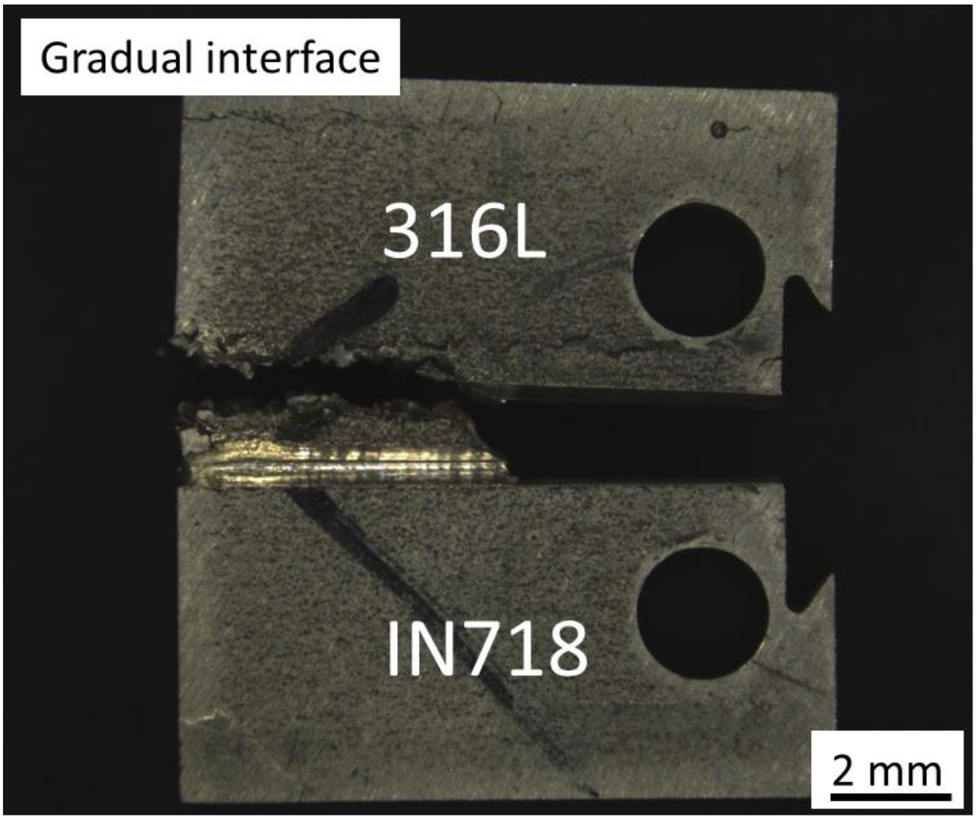

Figure 39. *MCT specimen after the fracture toughness test with clearly deflected crack propagation plane.*

5.3 Inclined continuous blocks results

Considering the results of HB and VB modifications, representing the limit cases for interface orientations, set of blocks with increasing interface angle orientation were produced. A continuous manufacturing process was employed to create four inclined interfaces (15°, 30°, 45°, and 60°) between 316L and IN718 referred as CIB15, CIB30, CIB45 and CIB60. The deposited material type changed correspondingly to the individual material zones bordering the fusion line. Due to the fact that the sharp interface clearly exceeds the gradual one, both in terms of structural integrity and mechanical behaviour, the following modifications were made only in the form of a sharp interface, where 316L was substrate for IN718. The deposited blocks are depicted in **Figure 40**.

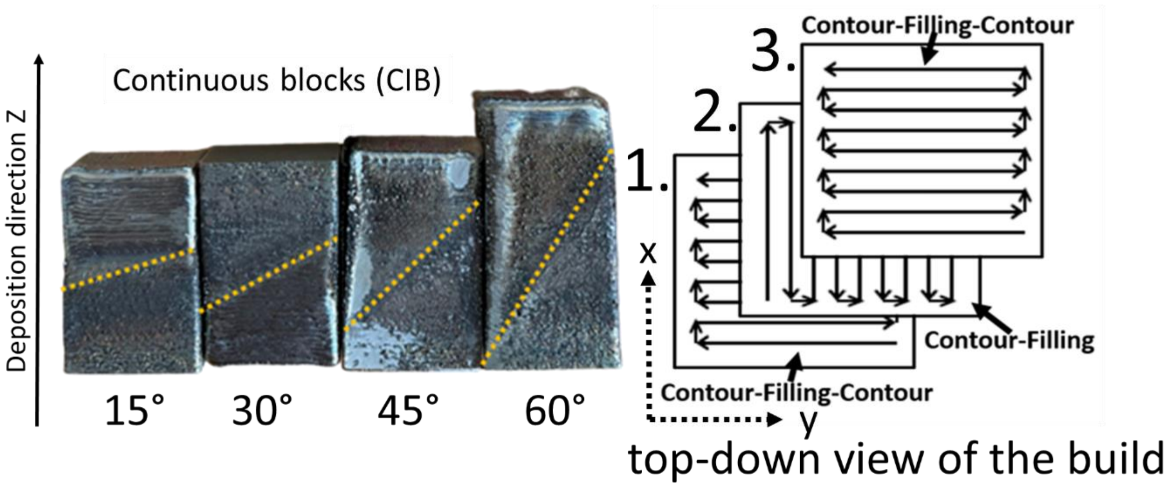

***Figure 40**. a) FGM blocks with inclined interfaces between 316L and IN718 ranging from 15° to 60° deposited continuously CIB, b) schema of the deposition sequences repetition from the top-down view of the build..*

The CIB blocks exhibit partially melted particles on the surfaces of both the 316L and IN718 segments. Additionally, the interface between the two materials is less distinct in CIB blocks, likely due to differences in the deposition strategy. Notably, there were no observed instances of cracking effects in either the DIB or CIB blocks.

5.3.1 Evaluation of porosity of CIB

After cutting and metallographic preparation, the porosity of CIB blocks was assessed within the YZ plane. A comparison of porosity and defect distribution is presented in **Figure 41**. The porosity measurements were consistently performed across four distinct regions: the 316L zone, IN718 zone, interface zone, and an overall porosity assessment. Macrographs in the figure vividly illustrate that the distribution and size of pores are influenced by the incline angle of the interface. An even distribution of relatively small globular pores is noticeable at an interface angle of 15°. As the angle increases to 30° and 45°, larger defects become apparent, along with an elevated concentration of these defects in the measured interface zone. The highest porosity is observed in the case of a 60° interface, reaching a value of 1%. For a comprehensive overview, **Table 9** provides a comparison of porosity evolution based on the angle of the interface. This comparison encompasses the single material zones as well as the interface region.

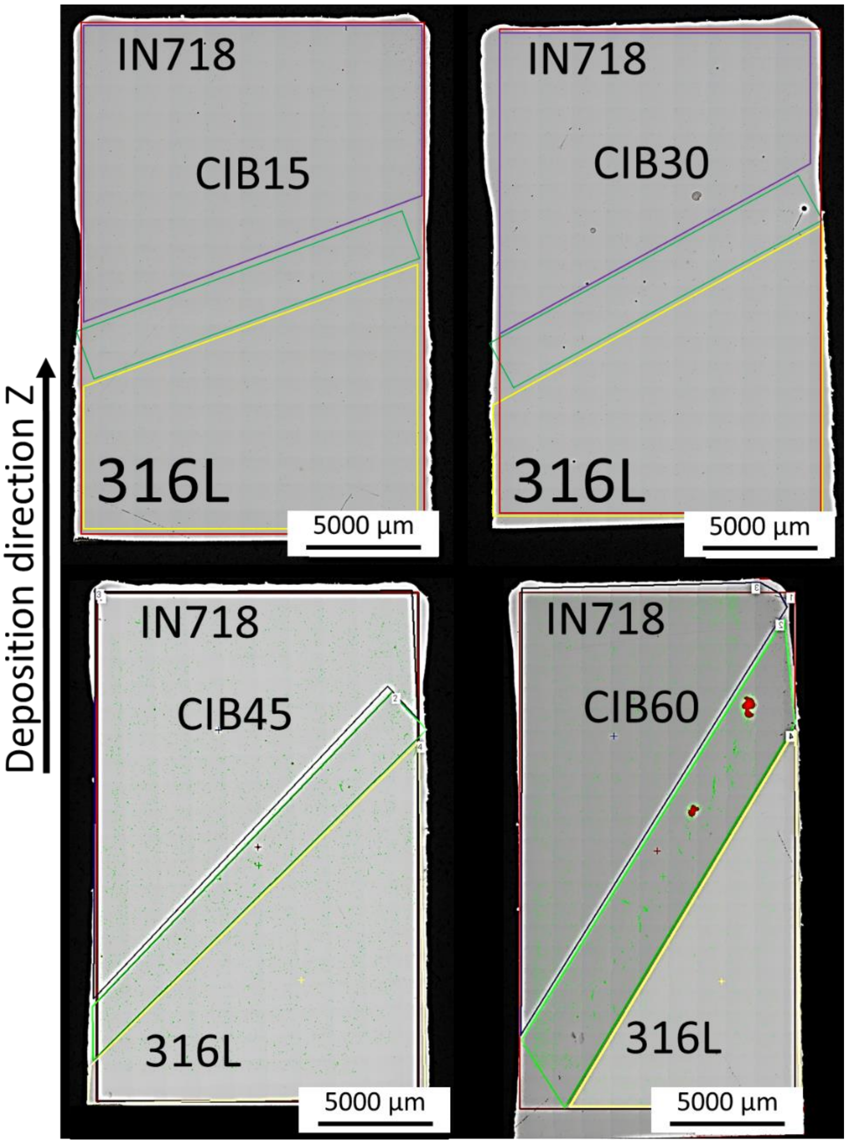

***Figure 41**. Macrographs of CIB blocks in polished state with designated areas of measured porosity.*

***Table 9**. Porosity values at the interface and individual material zones of CIB.*

Sample	Binary Area Fraction/%				
	Angle	Interface	316L SS	IN718	Whole
CIB15	15	0.062	0.042	0.051	0.048
CIB30	30	0.102	0.017	0.020	0.032
CIB45	45	0.227	0.052	0.075	0.086
CIB60	60	1.023	0.016	0.031	0.249

5.3.2 Light microscope observation of CIB

The nature of the joint zone between 316L and IN718 is captured in the macrographs in **Figure 42**. The interface of continuously deposited blocks takes on a gradual, step-wise transition from 316L to IN718. This interface exhibits a wavy or irregular character. The presence of a wavy or irregular interface can result in stress concentrations, thereby increasing the potential for localized deformation and points of potential failure under loading conditions. The wavy shape is more pronounced with the increasing angle. Additionally, such an interface might undermine the efficient transfer of loads between constituents, ultimately impacting mechanical properties and overall strength. Consequently, a straight interface is generally favoured due to its more desirable characteristics. Furthermore, the melt-pools adjacent to 316L exhibited dissimilar visual characteristics compared to both 316L and IN718 melt-pools. This visual disparity hints at potential differences in elemental distribution when compared to the corresponding side of continuously deposited blocks. This observation was subsequently confirmed through SEM EDS line scans conducted across various interfaces.

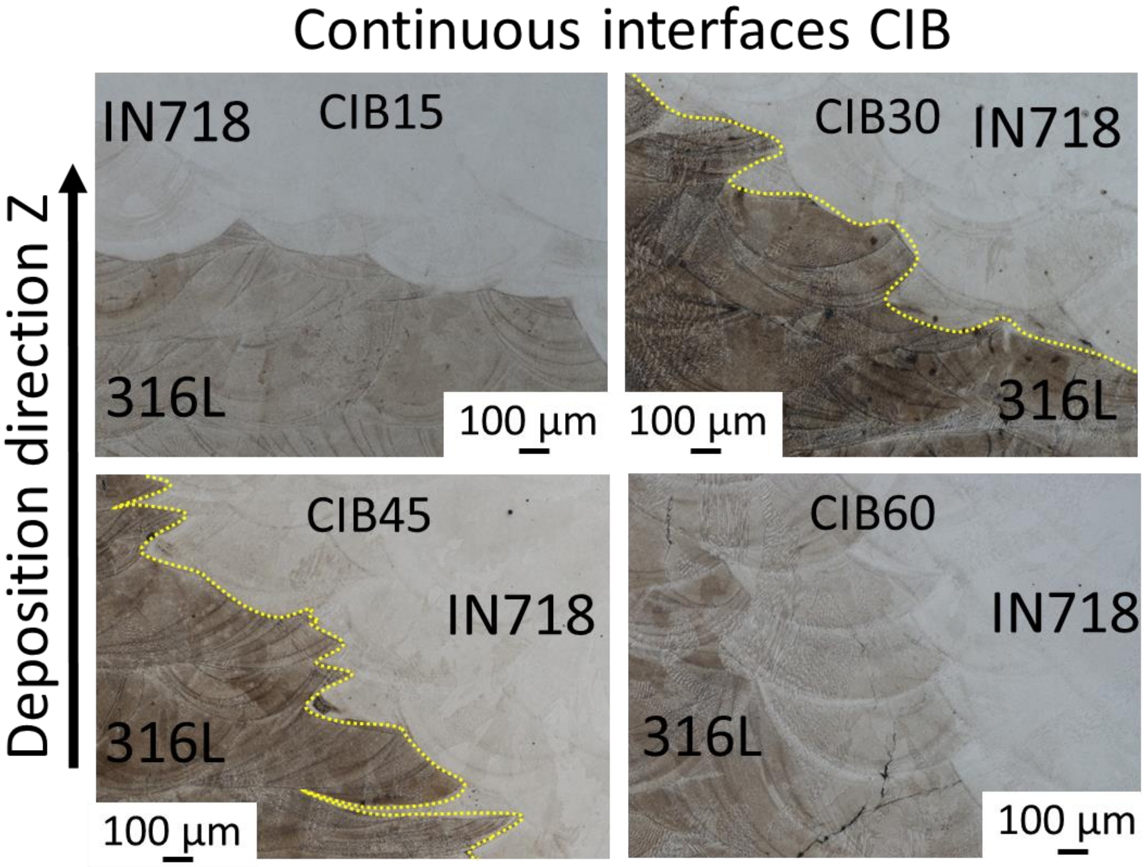

Figure 42. *Light microscope images of CIB interfaces.*

5.3.3 EDS and EBSD mapping of CIB

The EDS compositional maps of CIB interfaces for interface angle of 15° and 60° as extreme cases are displayed in **Figure 43**. The elemental distribution of Fe and Ni is gradual and changes within three zones, which are marked by yellow dotted lines for Fe mapping part.

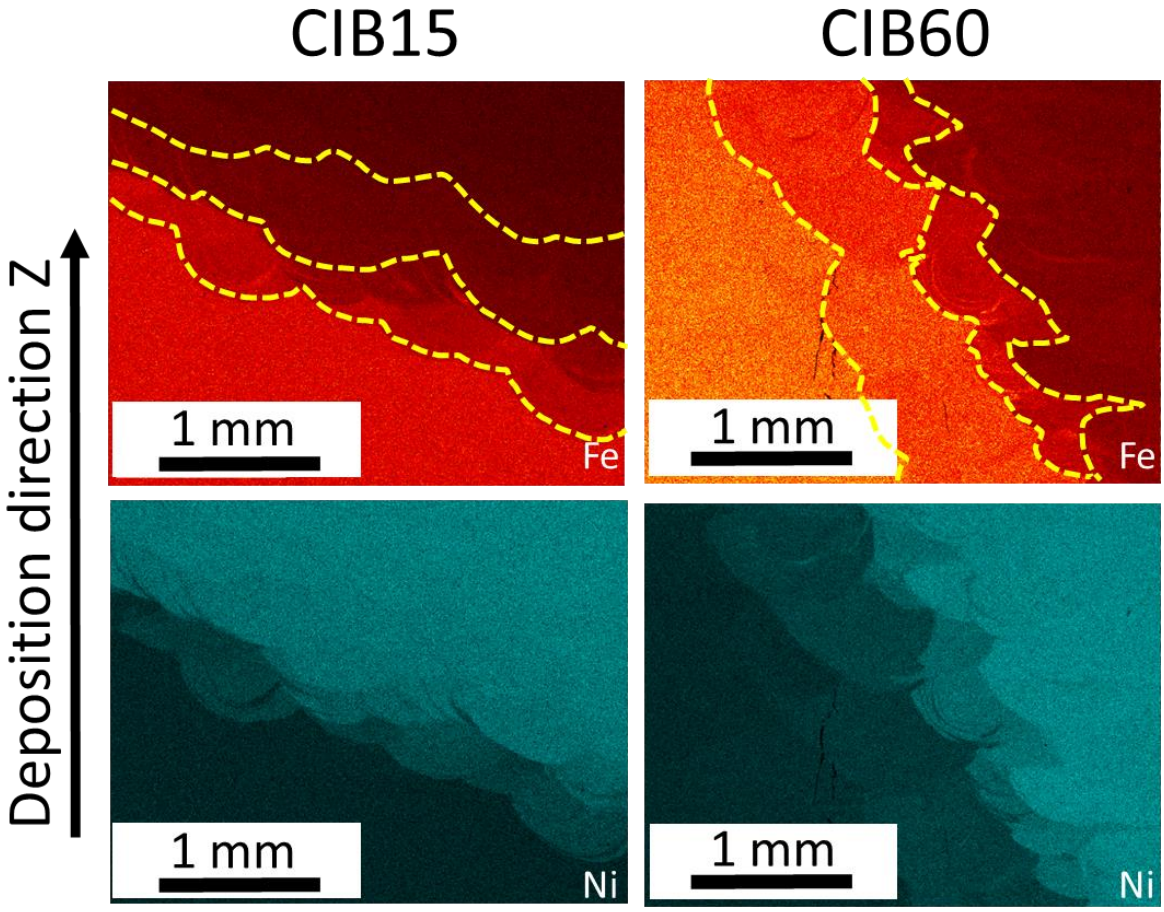

Figure 43. *EDS mapping of Fe (red) and Ni (green) elements at the interface of CIB15 and CIB60.*

EDS maps are supplemented by the EDS line analysis of Fe, Ni, Cr, Mo and Nb of all interface angle that were produced in **Figure 44**. The width of the transition zone between individual 316L and IN718 is the most visible with change of elements Fe and Ni. Continuously deposited interfaces showed certain band width, within which the content of Fe and Ni changes stepwise. The band is wide from 100 to 900 µm, based on the angle, until the Fe and Ni content is stabilized again. The Mo and Cr content was consistent across the interface.

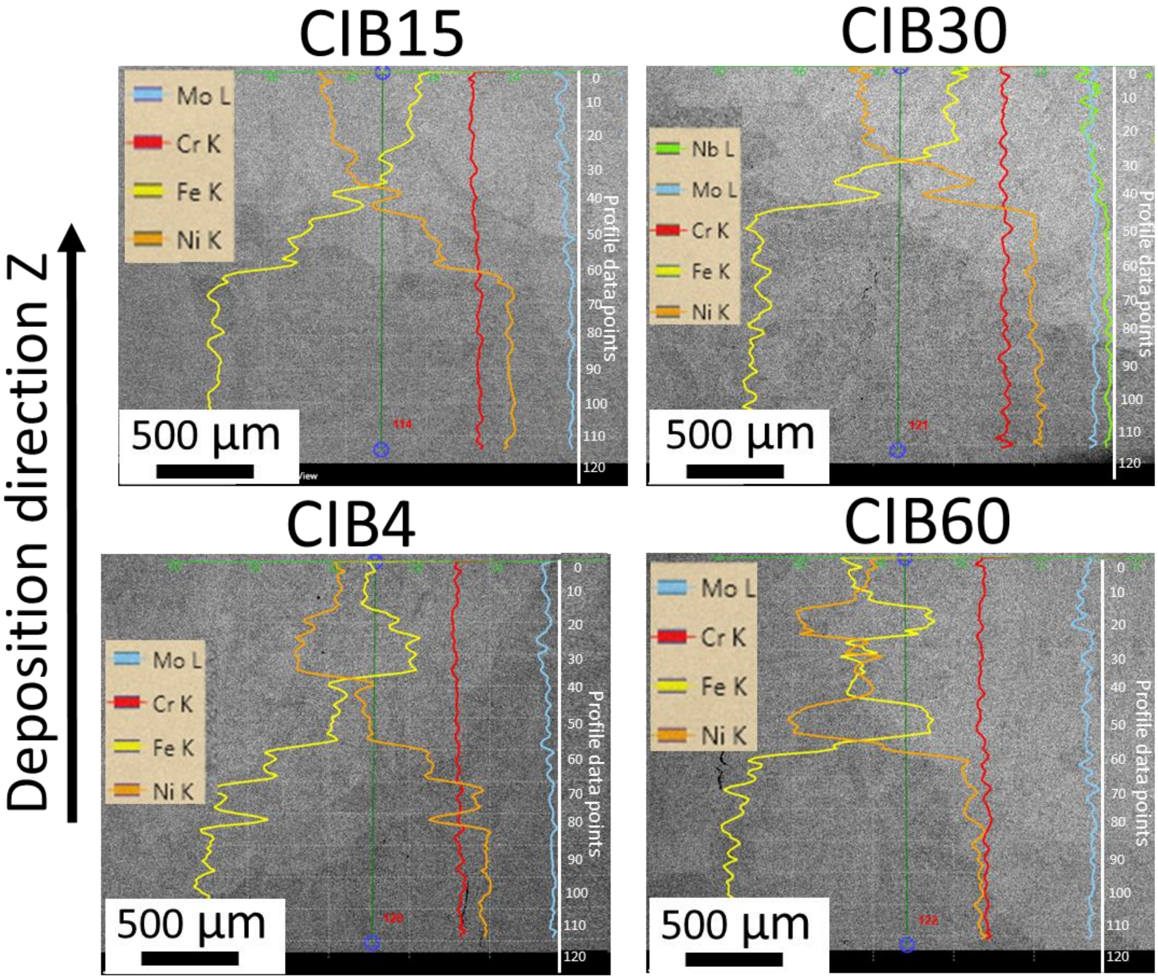

Figure 44. *EDS line scans across the CIB interfaces.*

EBSD maps illustrating CIB interfaces at both 15° and 60° inclinations are presented in **Figure 45**. The fusion lines between 316L and IN718 are highlighted using yellow dotted lines. Certain refinement is apparent in the third zone of compositional change of CIB15. Regions with refined grains are situated at the end of the material mixture zone, adjacent to the commencement of the pure IN718 zone. At the onset of the mixture zone, no notable change in grain orientation or size is observable. In the case of CIB60, the grain size distribution closely resembles that of CIB15. The fusion line is barely discernible. The grain refinement is not situated within certain area but seems to be more spread all over the compositional change zone, which seems to be caused by the higher degree of mixture. Across all mapped interfaces, no distinctive preferential crystallographic orientation was detected. All new grains retained a consistent, random orientation.

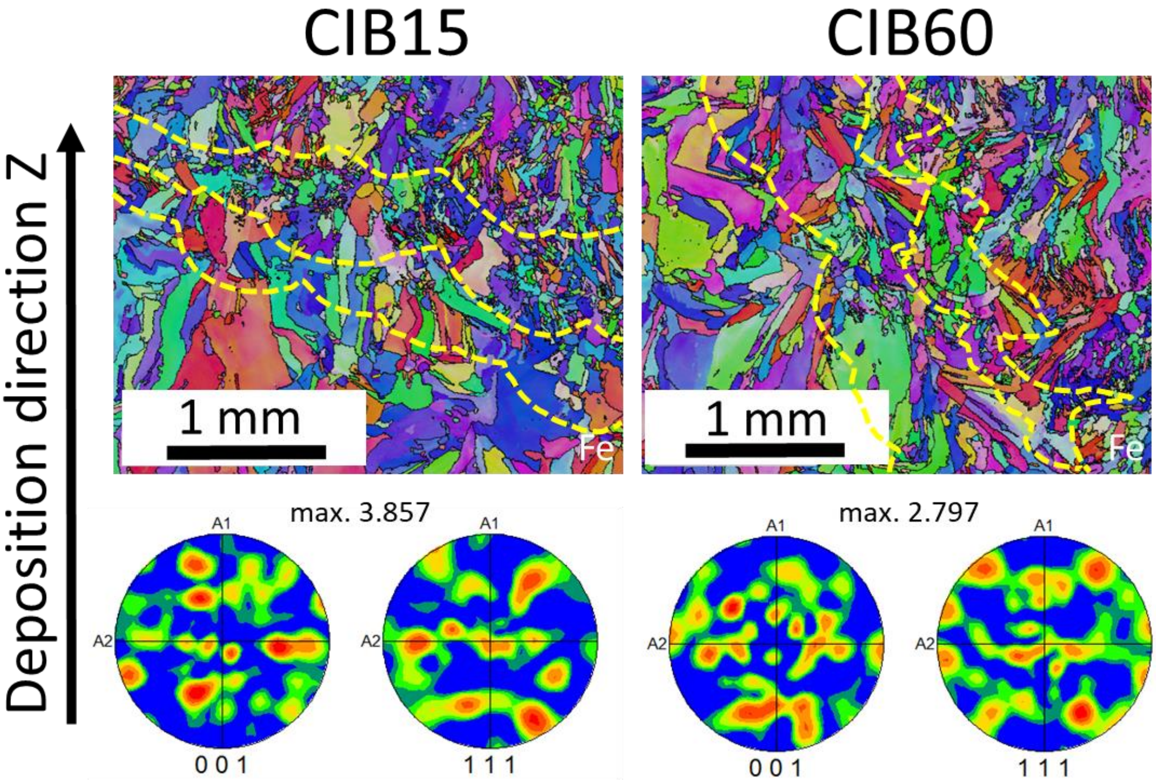

Figure 45. *EBSD images of CIB15 and CIB60 with the fusion lines marked by yellow dashed lines.*

5.3.4 Miniaturized tensile test results of CIB

Representative tensile curves of CIB modification are displayed in **Figure 46**. The tensile results are summarized in the column graph depicted in **Figure 47**. Starting from the left side of the graph, it becomes evident that although the 15° angle of CIB does not exhibit the highest strength, it outperforms others in terms of ductility. Additionally, $R_{p0.2}$ values ranging from 396 to 464 MPa and R_m values ranging from 519 to 562 MPa show only marginal variation with changes in the interface angle from 15° to 60°. Conversely, the elongation experiences a substantial decrease as the interface angle increases. Notably, the elongation drops by 80% for the steepest interface angle of 60°. Furthermore, a 70% decrease is observed even for the 30° interface angle. This indicates that while stress-related characteristics remain relatively stable, the ability of the specimens to deform significantly decreases with larger interface angles.

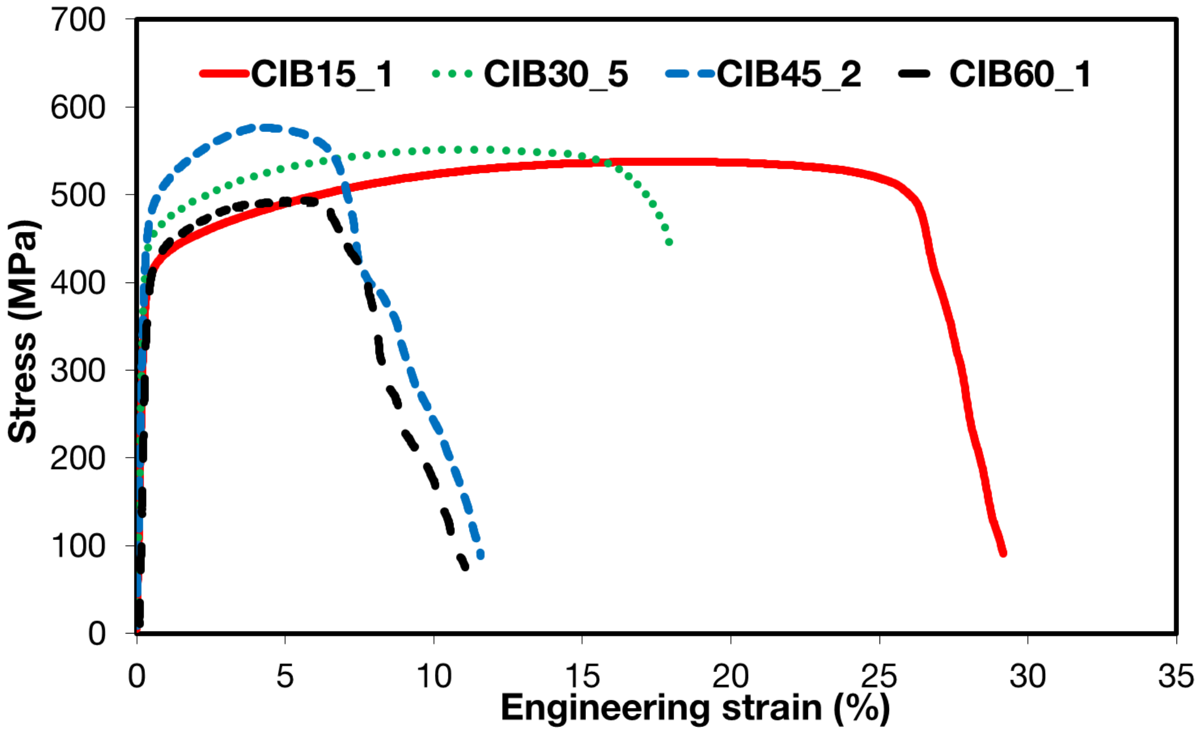

Figure 46. *Representative tensile curves of CIB MTT specimens.*

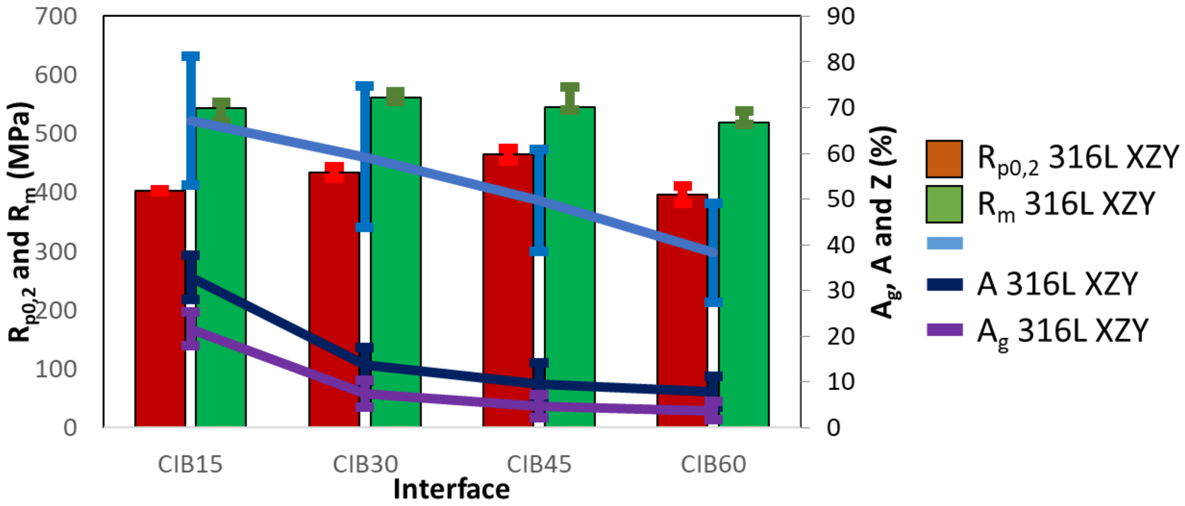

Figure 47. *Columns graphs of tensile parameters evaluated for CIB MTT specimens.*

5.3.5 Fractography of MTT specimens of CIB

Table 10 summarizes the representative MTT specimens selected for fractographic examination and EDS analysis. Typically, two specimens per batch were chosen—one exhibiting predictable behaviour and another that deviated from the rest of the group. The **Table 10** specifies the nature of the fracture and identifies the fracture location. The presence of SC was discovered near the interface zone on the side of pure 316L. It can be concluded that SC formed locally only in cases of CIB15. As the interface angle increased, both the quantity and size of SC increased, and they were observed in almost every tested MTT specimen. The interface angle also influenced the location of the specimen's fracture. While 316L was a definite location of failure for the CIB15 and CIB30 interfaces, the higher angles with more SC resulted in failure location to be situated partly at the interface.

***Table 10**. Results of SEM fractography of representative MTT CIB specimens with evaluated fracture location.*

M-TT	Sample		The character of the fracture	Location of the fracture
CIB	CIB15	1	Ductile dimple fracture, locally SC	316L
	CIB15	5	Ductile dimple fracture	316L
	CIB30	1	Ductile dimple fracture + SC	316L
	CIB30	5	Ductile dimple fracture	316L
	CIB45	2	Ductile dimple fracture + SC	interface + 316L
	CIB45	3	Ductile dimple fracture + SC	316L
	CIB60	1	Ductile dimple fracture + SC	interface + SS316L
	CIB60	5	Ductile dimple fracture + SC	interface + SS316L

The SEM images of fracture surfaces for representative MTT specimens are depicted in **Figure 48**. The images clearly show the evolution of SC presence with the increasing interface angle.

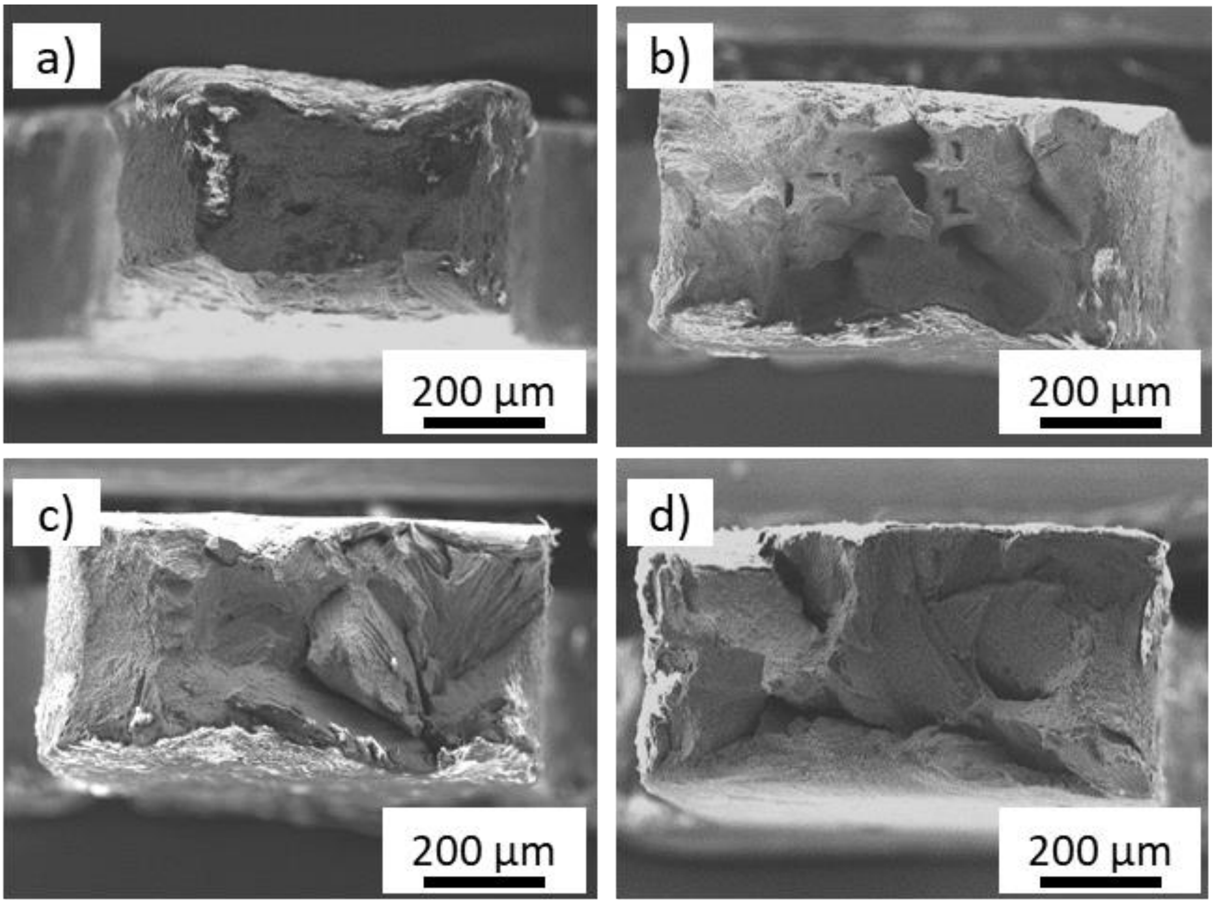

Figure 48. *SEM images of MTT specimen's fracture surfaces for continuous blocks, a) CIB15; b) CIB30; c) CIB45; d) CIB60.*

5.4 Inclined discontinuous blocks results

The DIB blocks constituted the final segment of the experimental part and were designed based on the key insights gleaned from the HB, VB and CIB blocks. This particular modification exclusively focused on the transition from 316L to IN718. Four blocks featuring a complete 316L material zone were created, each with a top plane inclination of 15°, 30°, 45°, and 60°. The results of CIB showed, the fusion line shape is strongly affected by the continuous deposition process and variable interface angle. Therefore, effect of the substrate surface treatment on the interface properties was investigated. The top surface of 316L underwent CNC machining to achieve a final roughness of 1.6 µm, after which the IN718 zone was deposited atop of the 316L region. Considering the repair operation of predefined geometry this approach is expected to ensure stability of the deposition process at the interface zone. This batch is referred to as discrete blocks (DIB) with blocks DIB15, DIB30, DIB45 and DIB60. Deposited blocks are depicted in **Figure 49**.

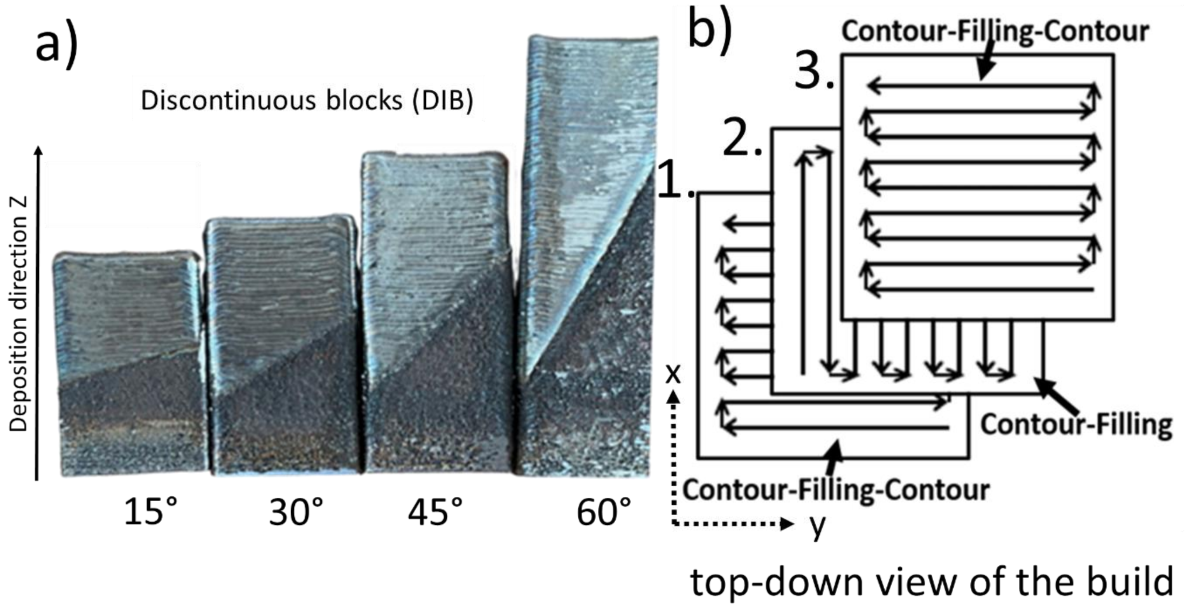

***Figure 49**. FGM blocks with inclined interfaces between 316L and IN718 ranging from 15° to 60° deposited discontinuously (DIB) and schema of the deposition sequences.*

For the DIB blocks, there is a high concentration of partially melted particles in the bottom half where 316L material was deposited. In contrast, the upper portion, made of IN718, is largely free from these particles and displays well-defined individual layers. The interface between individual materials is clearly visible compare to previous CIB blocks.

5.4.1 Evaluation of porosity of DIB

Macrographs of the polished DIB specimens are displayed in ***Figure 50***, allowing for a comparison. The porosity values for single materials zone and interface are summarized in **Table 11**. Results demonstrated that the defects concentration at the interface is stabilized for angle 15, 30 and 45° with the level below 0.06 %. Conversely, a rapid escalation in both porosity and cracks was observed for the 60° interface. Remarkably, even though the 60° interface exhibited a porosity value of 0.49%, this still amounted to less than half of the porosity observed in CIB specimens featuring a 60° interface. This reduction in defects' progression during deposition is attributed to the surface machining carried out prior to the deposition of IN718.

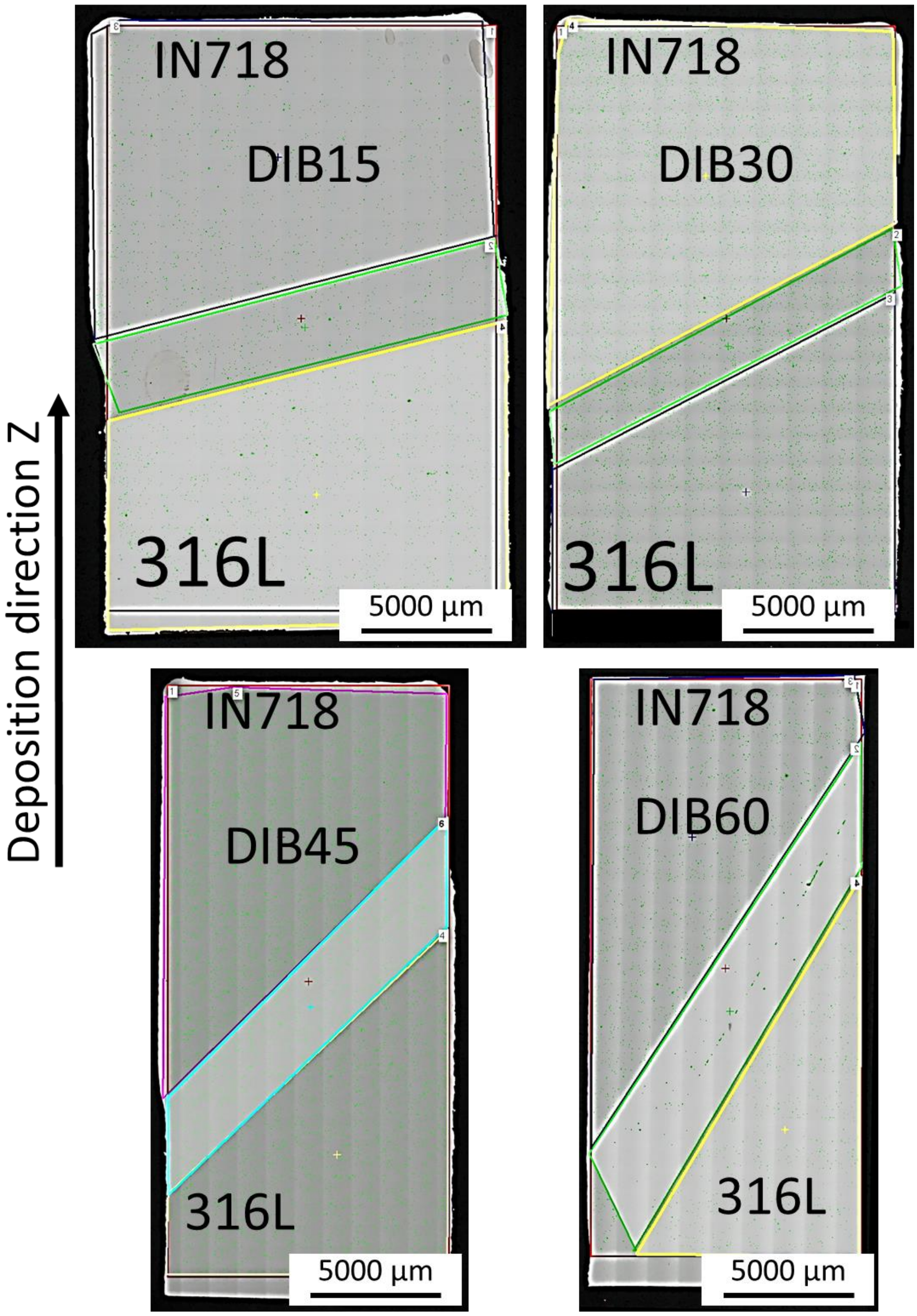

Figure 50. *Macrographs of DIB blocks in polished state with designated areas of measured porosity.*

Table 11. *Summary of porosity values per each measured area of inclined interfaces DIB.*

Sample	**Binary Area Fraction/%**				
	Angle	Interface	316L	IN718	Whole
DIB15	15	0.04	0.074	0.031	0.051
DIB30	30	0.06	0.050	0.081	0.067
DIB45	45	0.04	0.024	0.044	0.035
DIB60	60	0.49	0.023	0.056	0.210

5.4.2 Light microscope observation of DIB

The nature of the joint zone between 316L and IN718 is captured in the macrographs in **Figure 51**. In this case, the fusion lines separating the individual material are conclusively recognizable thanks to their sharp nature for all interface angles. Furthermore, no material mixture was visualized by the etching procedure.

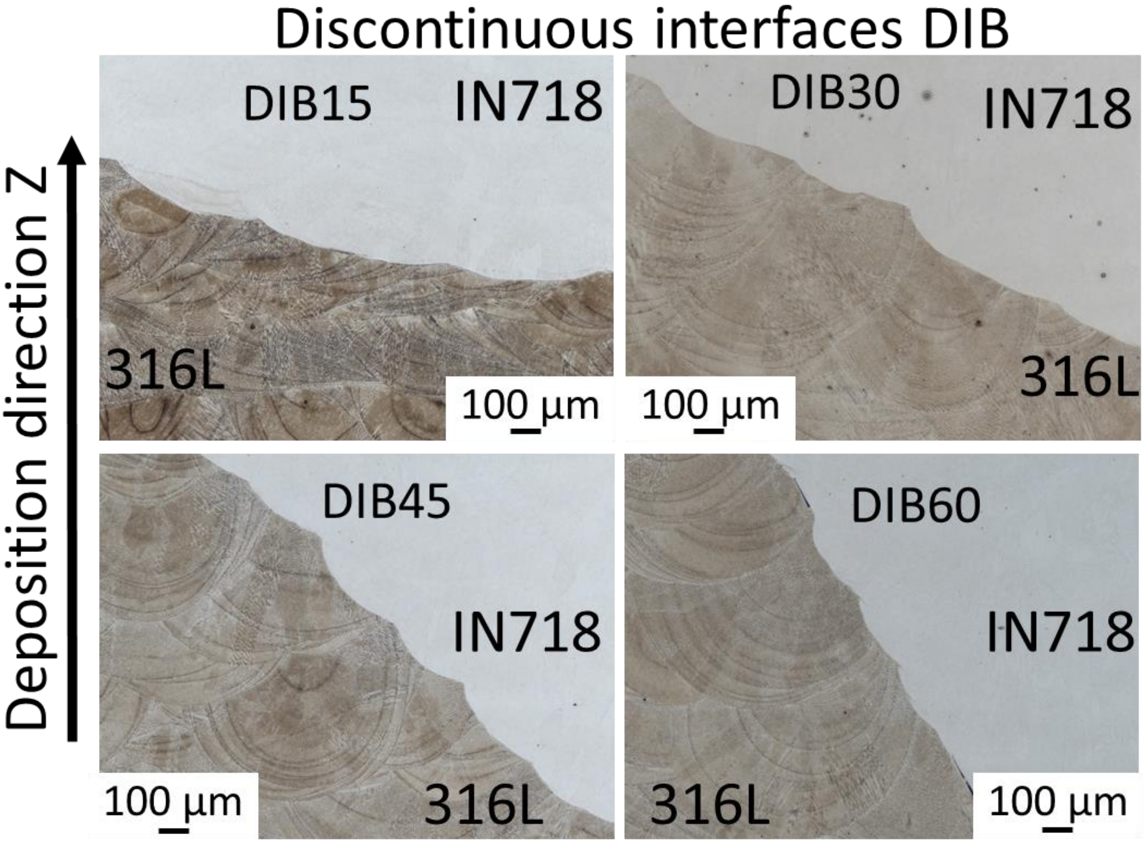

Figure 51. *Light microscope images of DIB interfaces.*

5.4.3 EDS and EBSD mapping of DIB

The EDS compositional maps of DIB for interface angle of 15° and 60° are displayed in **Figure 52**. EDS maps showed mostly discrete distribution of Fe and Ni in their primary material zones. In the case of DIB15 a local areas of Fe and Ni content are presented and marked by yellow arrows.

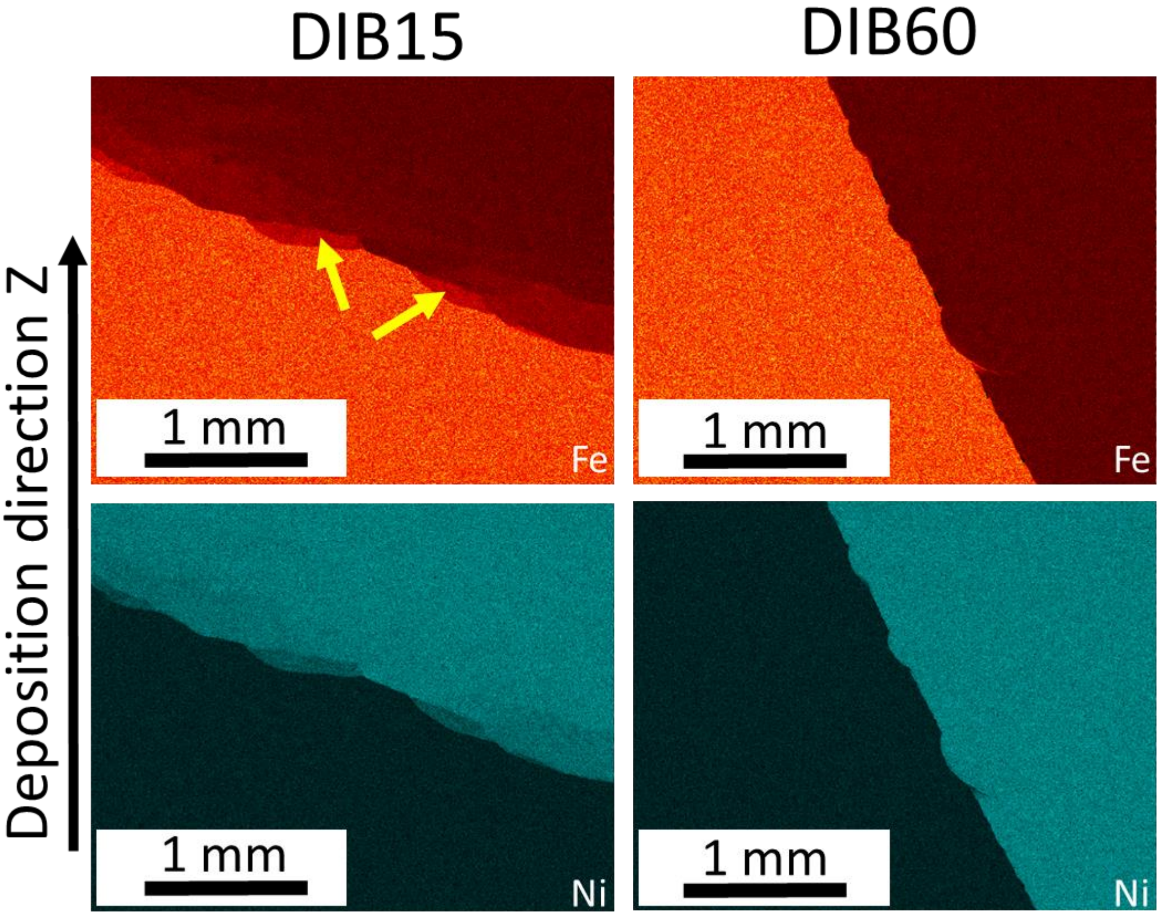

Figure 52. *EDS mapping of Fe (red) and Ni (green) elements at the interface of DIB15 and DIB60.*

EDS maps are supplemented by the EDS line analysis of Fe, Ni, Cr, Mo and Nb of all interface angles in **Figure 53**. The width of the transition zone between individual 316L and IN718 is the most visible with change of elements Fe and Ni. Mostly steep change of Fe and Ni content was observed, except the DIB30 where two step chemical change was observed and DIB15 where the composition on IN718 is more gradual.

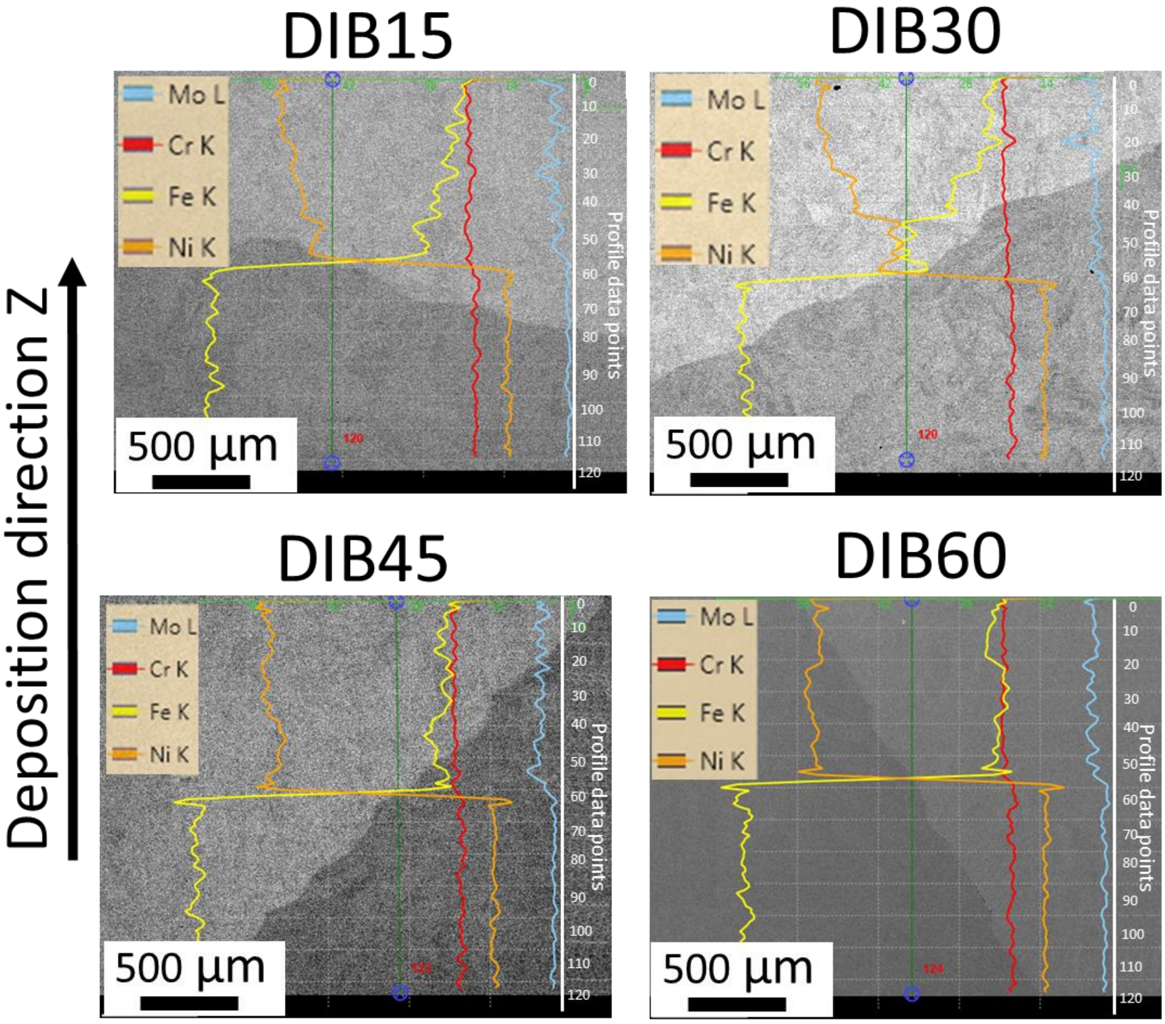

Figure 53. EDS line scans across the DIB interfaces.

EBSD maps illustrating DIB interfaces at both 15° and 60° inclinations are presented in **Figure 54**. The fusion lines between 316L and IN718 are highlighted using yellow dotted lines. Strong grain traceability is evident across the fusion line for DIB15, akin to what was observed in the HB case. These grains are generally elongated in the deposition direction, maintaining consistent sizes across the marked interface. However, a refinement zone is notable in the centre of the micrograph. In contrast, the fusion line of DIB60 predominantly features refined grains on the IN718 side, growing perpendicular to the fusion line. Subsequent to this, coarsening occurs in grains that were already elongated in the deposition direction. Notably, the rapid refinement effect observed at the fusion line of DIB60 was not witnessed in any other modification to such an extent. Across all mapped interfaces, no distinctive preferential crystallographic orientation was detected. All new grains retained a consistent, random orientation.

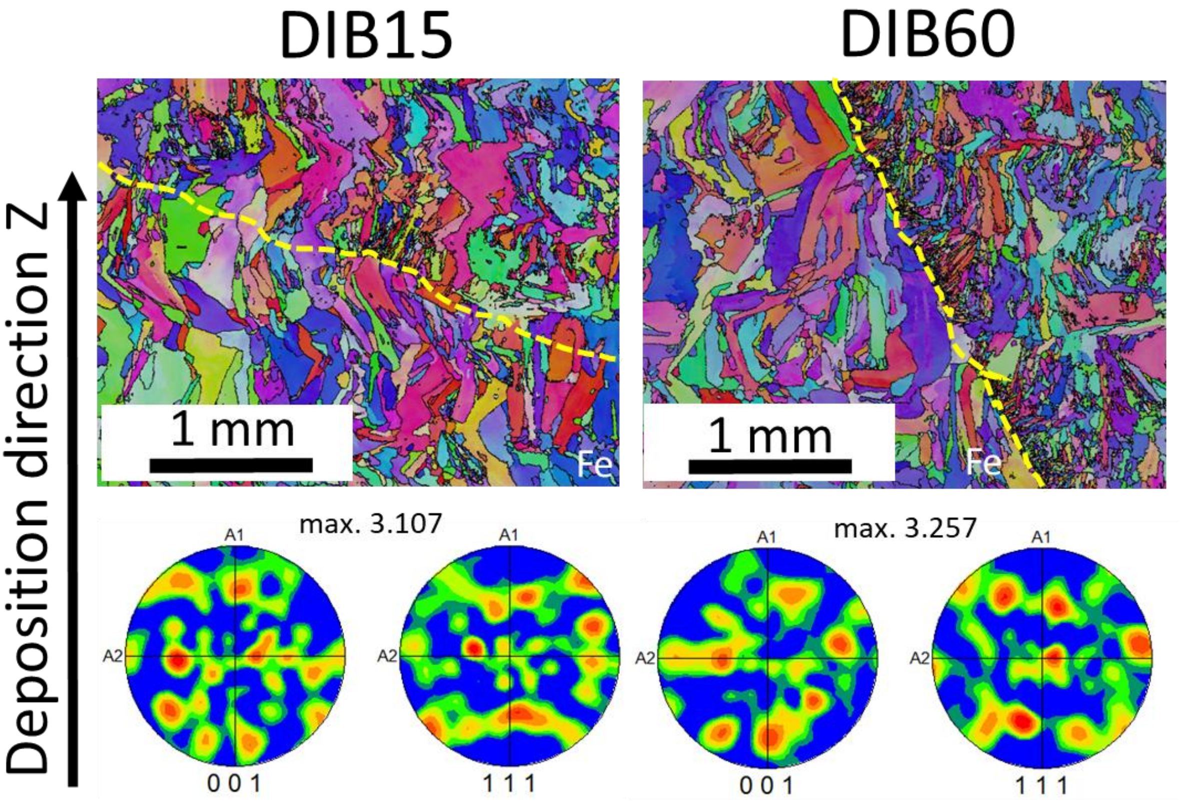

***Figure 54**. EBSD images of DIB15 and DIB60 with the fusion lines marked by yellow dashed lines.*

5.4.4 Miniaturized tensile test results of DIB

The representative tensile curves are displayed in **Figure 55**. Tensile parameters are summarized in column graphs in **Figure 56**. While R_m and $R_{p0.2}$ values closely resemble those of continuous blocks, the deviations of $R_{p0.2}$ and R_m across different angles are notably lower (ranging from 422 to 473 MPa and 554 to 580 MPa, respectively). This reduction in deviation can be attributed to the lower concentration of defects, which contributes to increased repeatability in material behaviour within the test batch. For all interface angles of DIB, the elongation values fall below those of CIB15. However, the values are more consistent for angles of 15°, 30°, and 45°, with values hovering around 25% higher than the elongation of the IN718 zone from HB. Despite the elongation improvement observed for 30° and 45° angles, there is a decline in elongation for the 60° angle. Nevertheless, the final value of 14% is twice as high as that of the 60° continuous block angle.

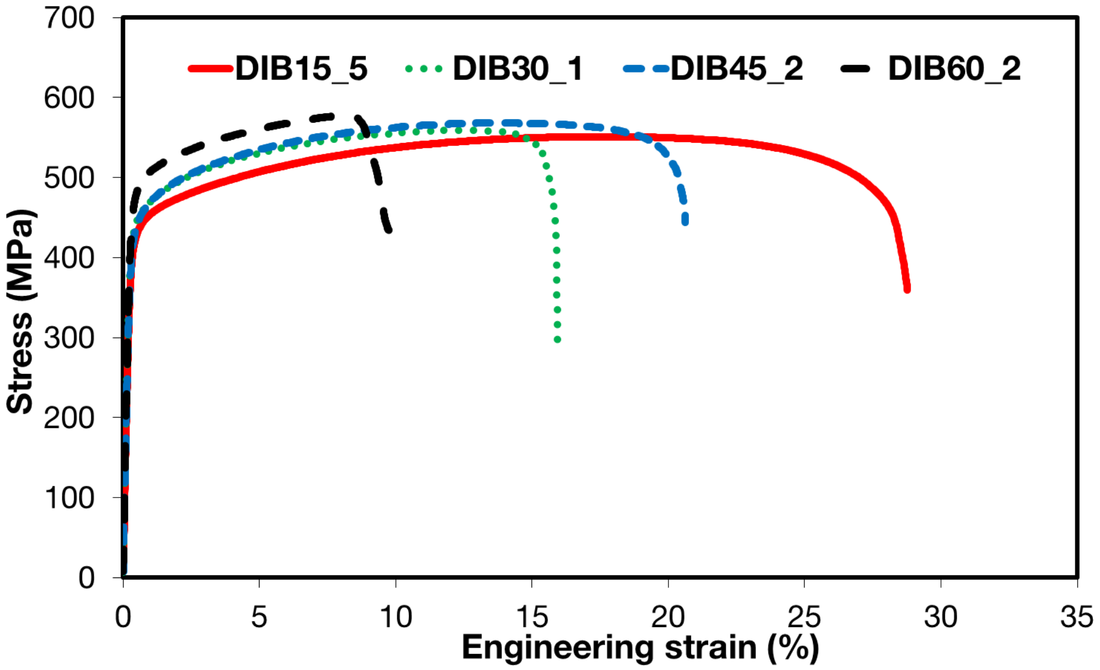

Figure 55. Representative engineering tensile curves of interface located MTT of DIB.

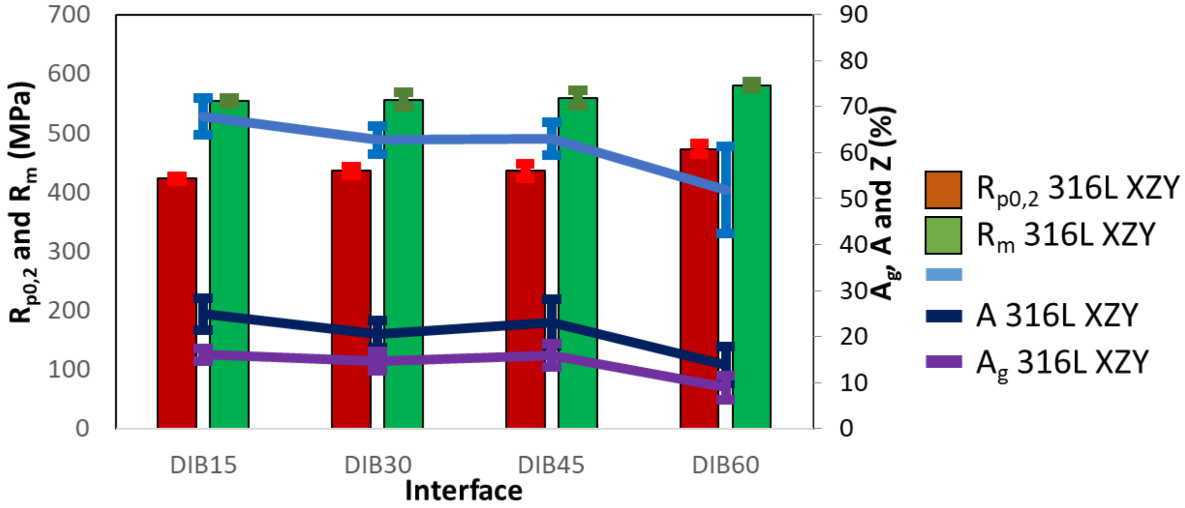

Figure 56. Column graphs of MTT results of DIB for interface located specimens.

5.4.5 Fractography of MTT specimens of DIB

Table 12 summarizes the representative MTT specimens selected for fractographic examination and EDS analysis. The **Table 12** specifies the nature of the fracture and identifies the fracture location. The presence of SCs was discovered near the interface zone on the side of pure 316L only in the case of DIB60. For previous interface angles the fracture appeared to have strictly ductile dimple morphology. In addition, the specimen's failure location was situated always within 316L part of the specimen. The exception was precisely the specimens from the DIB60 interface, where the presence of SCs moved the fracture area closer to the interface.

***Table 12**. Results of SEM fractography of representative MTT DIB specimens with evaluated fracture location.*

M-TT	Sample		The character of the fracture	Location of the fracture
DIB	DIB15	1	Ductile dimple fracture	316L
	DIB30	1	Ductile dimple fracture	316L
	DIB45	3	Ductile dimple fracture	316L
	DIB60	1	Ductile dimple fracture	316L
	DIB60	2	Ductile dimple fracture + SC	interface + 316L

The fracture surfaces of MTT specimens after the test are displayed in ***Figure 57***. The fractographic analysis confirms the EDS fracture measurement since no SC were observed for DIB15, 30 and 45, while DIB60 showed presence of SC affecting the tensile performance. The part of the fracture surface containing SC is marked by red dashed line.

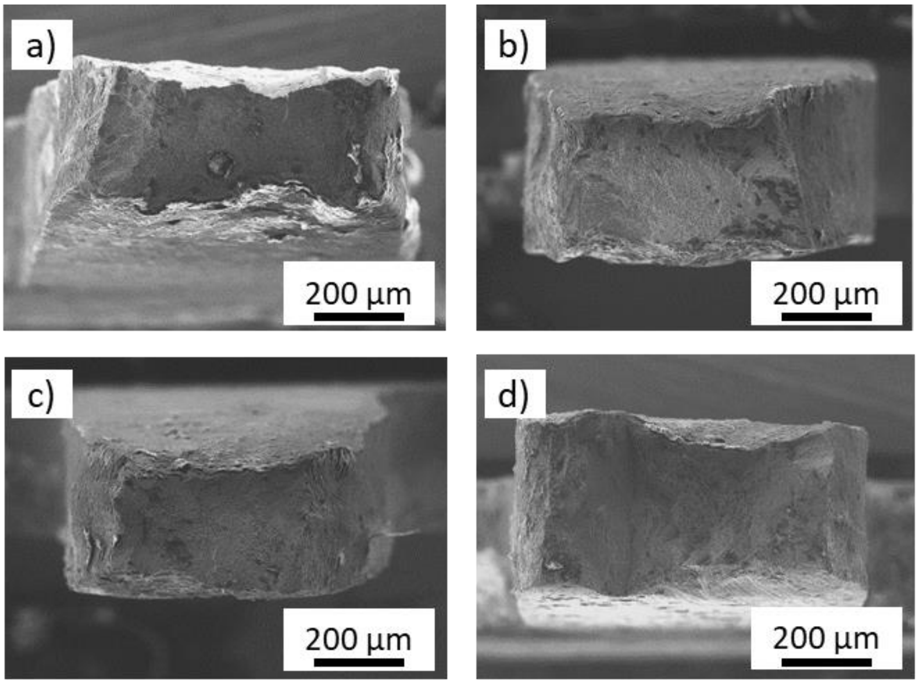

***Figure 57**. SEM images of MTT specimen's fracture surfaces for DIB, a) DIB15; b) DIB30; c) DIB45; d) DIB60.*

5.5 HB sharp interface failure analysis

Previous chapters presented the mechanical performance of various FGM modifications. VB showed critical tensile performance for all interfaces and CIB and DIB showed significant impact on the elongation values. The HB results demonstrated significant difference in strength and elongation between sharp and gradual interfaces. Therefore, the analysis of HB interfaces under tensile loading is provided in this chapter, to fully understand the failure mechanism considering various specimens orientations.

MTT specimens were recorded using DIC software to evaluate the deformation behaviour of the interface-located specimens and analyse the failure mode principles of the FGM under various orientations. The fracture of the specimens extracted from the sharp interface showed a relatively defect-free structure, with only a few globular pores. ZYX and XZY oriented specimens were analysed to identify the failure process. The strain distribution on the MTT specimens for the selected samples is depicted in **Figure 59** and **Figure 62**. For reference, in **Figure 58**, the strain distribution for the ZYX-oriented specimen across the gradual interface is presented. The strain distribution is influenced by a higher number of defects detected on the fracture surface. These defects cause the concentration of deformation from the very beginning of the test until the specimen fails. This leads to a rapid decrease in the material's plastic potential during tensile loading.

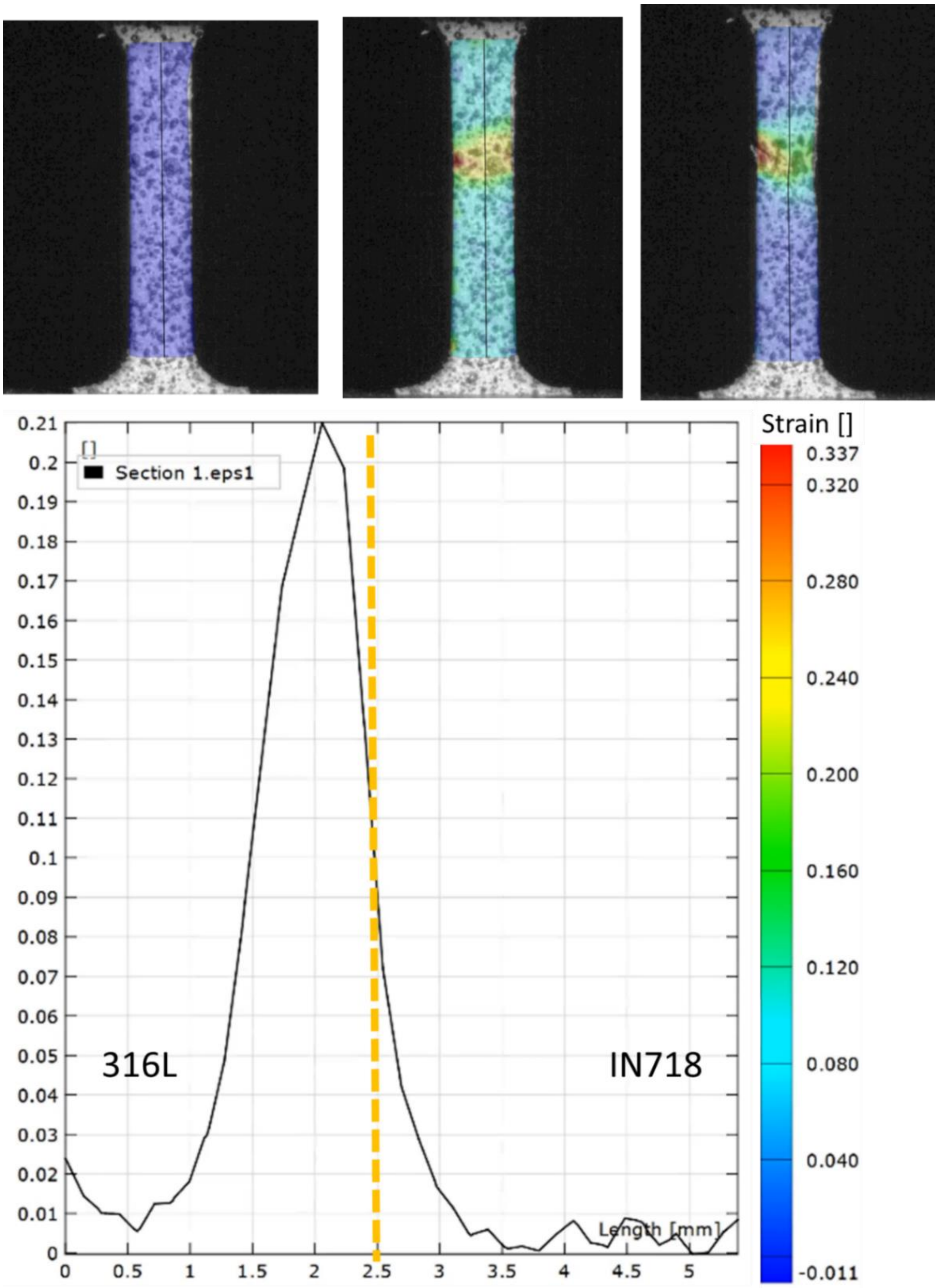

Figure 58. *Strain distribution of MTT specimen located across the gradual interface (ZYX) a) before loading; b) elastic part of the test; c) at fracture; d) major strain profile at the elastic stage of tensile load.*

The deformation process of the ZYX MTT specimen extracted from the sharp interface differs significantly. During the application of tensile load, the strain primarily occurs within the steel portion of the specimen, even in the early stages when elastic loading is predominant. Since IN718 is a generally stronger material, necking occurred within the 316L part, leading to the initiation of fracture. This is corroborated by the evolution of the DIC strain map. A comparison of the extensometer-time evolution among the entire specimen, the 316L part, and the IN718 part is presented in **Figure 60**. This comparison demonstrates that IN718 reaches its maximum deformation value of 2.5% at the moment when the 316L part reaches a deformation of 20.7%. When comparing tensile curves for MTT specimens made of individual materials in **Figure 61**, it is observed that a 2.5% deformation corresponds to a stress of 650 MPa for IN718 and approximately 540 MPa for 316L. Based on the tensile curve of the sharp interface MTT specimen, the stress-strain evolution corresponds to that of the 316L material. Therefore, if the defect concentration is below the critical level and the fusion between materials is stronger with 316L, the fracture will always occur within the 316L portion.

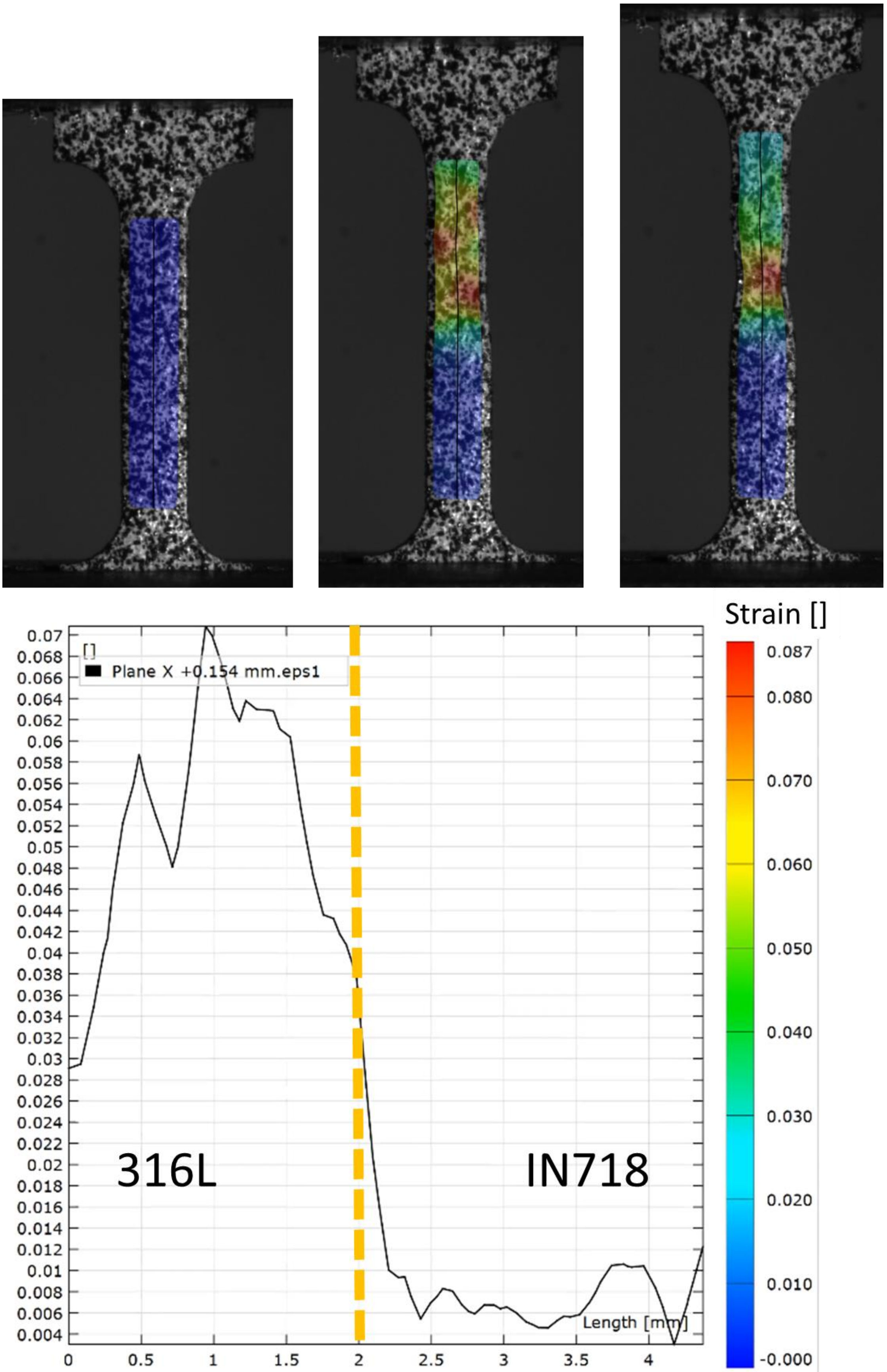

***Figure 59**. Strain distribution of MTT specimen located across the sharp interface (ZYX) a) before loading; b) elastic part of the test; c) at fracture; d) major strain profile at the elastic stage of tensile load.*

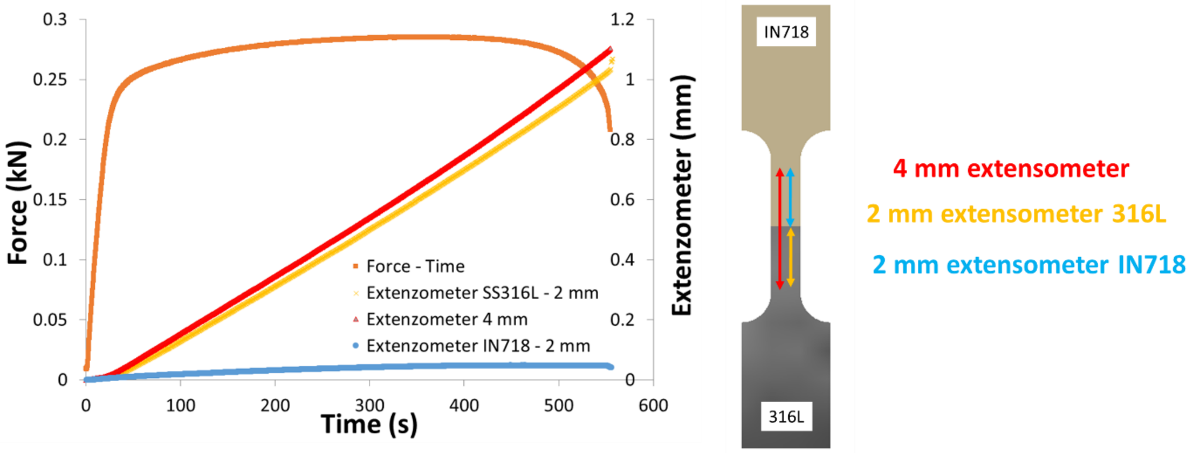

Figure 60. *Comparison of the extensometer-time evolution between full extensometer length (4 mm) and half extensometer gauge length of 2 mm for individual halves of the specimens.*

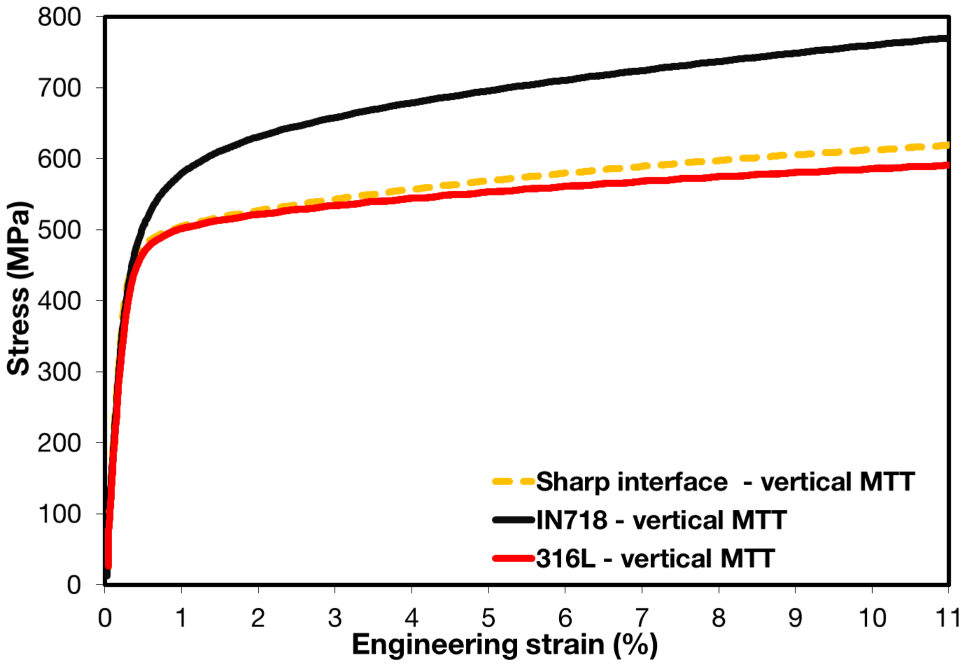

Figure 61. *Comparison of the engineering tensile curves between individual materials and sharp interface.*

The failure mode of the MTT specimen changes when the tensile load is applied along the interface plane. The strain map evolution for horizontally oriented MTT (XZY) specimens is presented in **Figure 62**. In this case, the strain map shows a uniform distribution of deformation across the material zone. In other words, both the 316L and IN718 halves of the specimen deform evenly. When comparing the tensile curves of the interface specimen to those of the individual materials, it becomes apparent that the tensile curve falls between those of the single materials. This suggests that the MTT specimen benefits from the strength of the IN718 portion, and thus, stress distribution across the sample cross-section may not be entirely uniform. Analysis of DIC maps revealed that these specimens consistently failed from the side of the specimen, as shown in **Figure 62**. The tensile curves for the 316L specimens indicated an ultimate tensile strength of 620 MPa, while the current curve exhibited R_m of 750 MPa. Consequently, it is assumed that the failure did not occur within the 316L portion. Another critical factor to consider is the potential for plastic deformation. IN718 generally exhibits a lower potential for plastic deformation, as evidenced by its significantly lower elongation compared to 316L. Additionally, the strain hardening is also more pronounce to the IN718 based on the plastic part of the tensile curve. During the test, the load is predominantly carried by IN718, which depletes its capacity for plastic deformation first. The elongation of the interface-located specimen closely resembles that of the IN718 single material. Therefore, all the evidence suggests that the fracture process occurs on the side of the IN718.

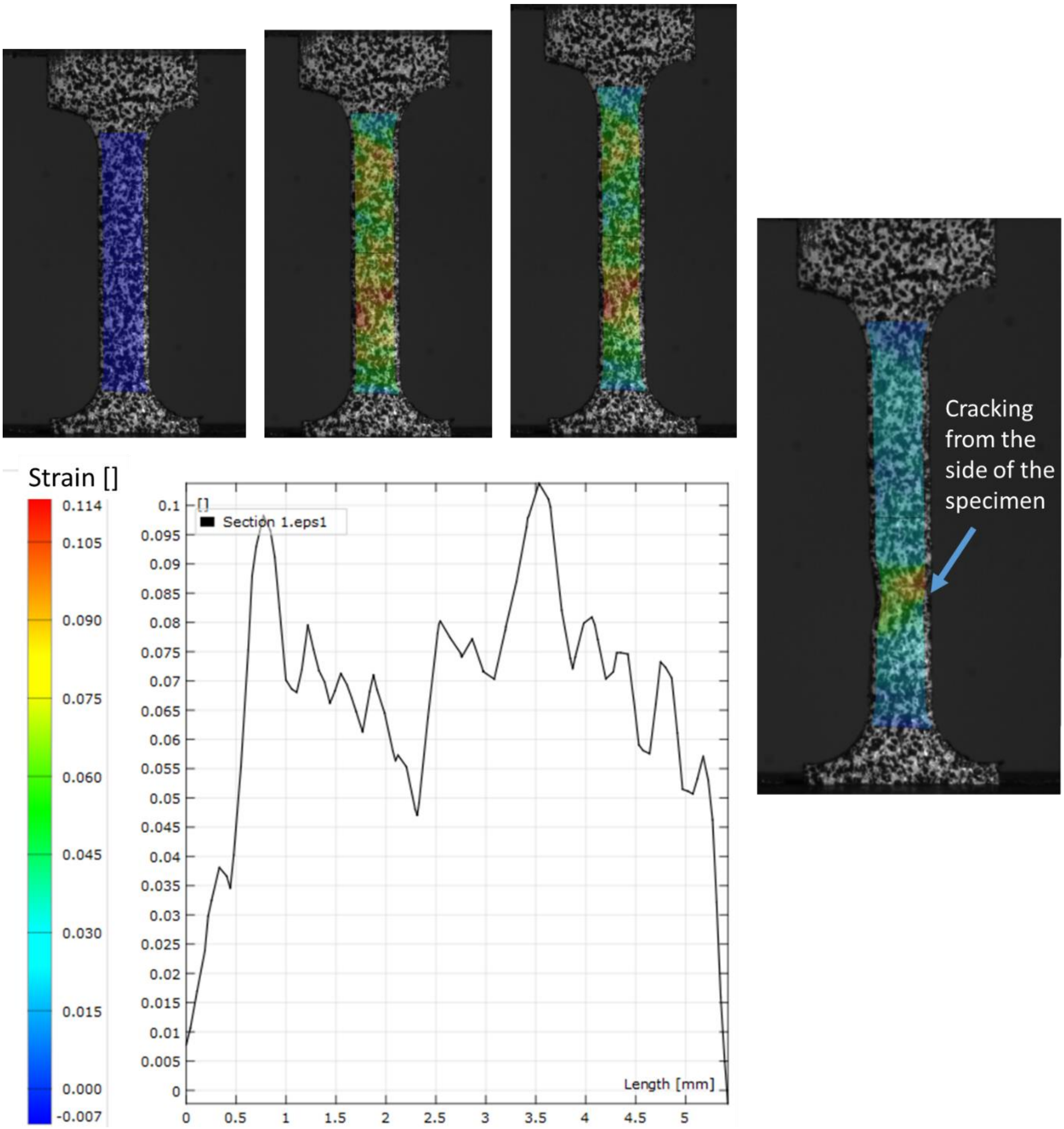

***Figure 62**. Strain distribution of MTT specimen located across the sharp interface (YXZ) a) before loading; b) elastic part of the test; c) at fracture; d) major strain profile at the elastic stage of tensile load.*

The strain map overview displayed in **Figure 63** clearly demonstrates that the deformation process for the gradual interface is confined to a small zone due to the higher concentration of defects. This is also evident from the strain map, which shows that the sections of the specimens near the head are coloured blue, indicating a low strain level. In the case of the sharp interface, the strain profile along the specimen reveals a gradual increase in strain level from the shoulder to the centre (316L) with a sudden decrease within the IN718 part. The yellow lines indicate the position of the material interface.

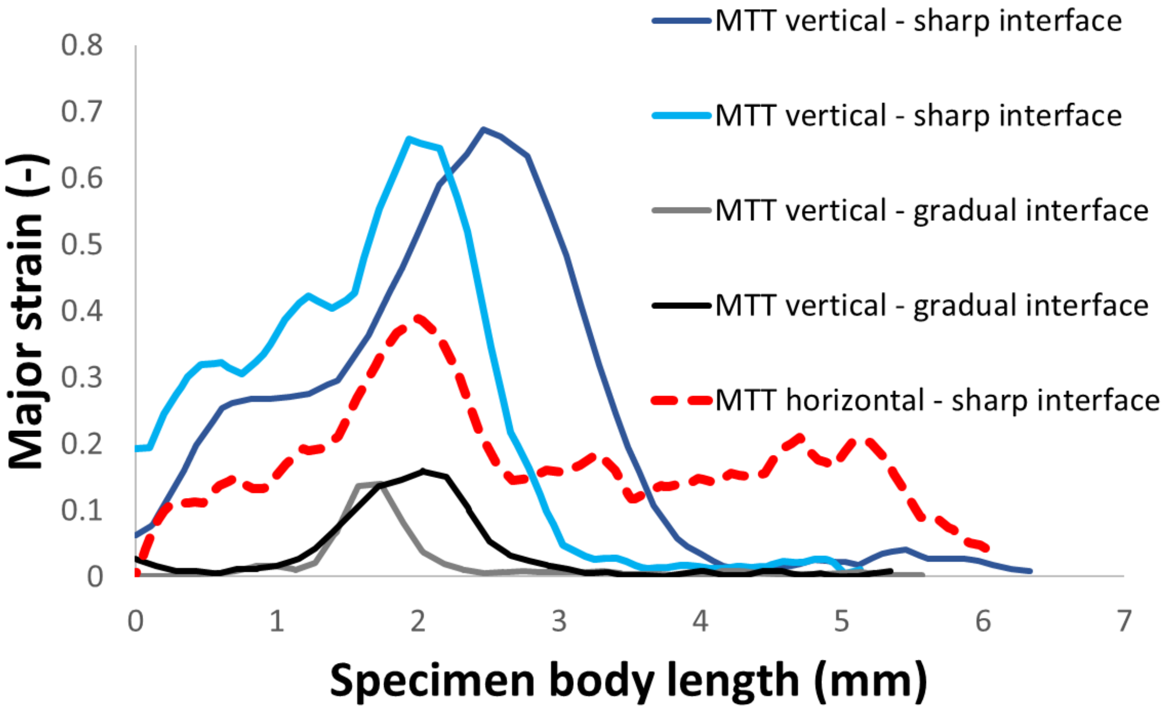

Figure 63. *Comparison of major strain profiles along the gauge length of MTT specimens between sharp and gradual interfaces.*

6 Discussion

The results section of the thesis demonstrates significant differences among each investigated FGM modifications. The main factors that affect the successful production of FGM materials using DED are identified and evaluated in this section. In the experimental part of the thesis, notable findings have been made concerning the evolution of the structure, the formation of defects, and the mechanical behaviour of the produced FGM. A comprehensive overview of the structural and mechanical properties is presented, along with a critical assessment of the potential applicability of each modification.

6.1 Interface orientation-dependent structure evaluation

The appearance of the material interface strongly depends on the orientation of the deposited material in relation to the melt-pool. A visual comparison of horizontal and vertical interfaces is presented in **Figure 64**. Based on the comparison of EDS maps, it is evident that the horizontal interface appears straighter, with well-defined areas of single materials. Conversely, the vertical interface exhibits a clear zig-zag pattern as each single material is alternately deposited. A zig-zag or irregular interface can introduce stress concentrations, leading to localized deformation and potential failure points during loading. This can reduce the efficiency of load transfer between the constituents, resulting in compromised mechanical properties and lower overall strength. Therefore, a straight interface is generally preferred. However, zig-zag pattern seems to be inevitable when vertical interface is produced due to the alternate deposition sequence. Furthermore, due to the defects observed in the vertical block (VB), the actual mechanical performance of the VB interface could not be evaluated. Considering the created temperature field and heat transfer typical for AM processes, each interface type had a different temperature history, potentially resulting in varying levels of residual stress and differences in elemental distribution across the interface. Singh et al. [148] analysed residual stress in laser-deposited IN718. The highest residual stresses were detected near the platform of the block where the largest thermal gradients were present. Similar results might be expected at every interface for a two-material FGM system. However, a thorough investigation of residual stress distribution across the graded block would be required to support this theory.

Nevertheless, such an analysis was beyond the scope of this work. Another difference caused by various single material orientations might be found in the melt-pool flow dynamics. In the case of a horizontal interface, the two different materials are unevenly distributed within the melt-pool, with one material located at the bottom while the currently deposited material is in the upper part. In contrast, the melt-pool of a vertically oriented interface is divided into left and right sides with respect to the material position. In this case, the laser beam spot is aimed equally between the IN718 and 316L zones. Due to the different starting material distribution within the melt-pool, varying levels of mutual mixture can be expected. The so-called Marangoni effect describes mass transfer as a result of driving forces arising from temperature and surface tension differences within the melt-pool. Furthermore, melt-pool fluid transfer is a phenomenon highly dependent on deposition parameters, which becomes even more complex when dealing with the deposition of two different materials. In such cases, differences in temperature and surface tension are increased due to variations in material heat conductivity and material density between the two different materials [61]. Ultimately, the degree of material compatibility determines whether the constituents will be mixed together to form a unified material mass or tend to separate from each other, resulting in a heterogeneous mass.

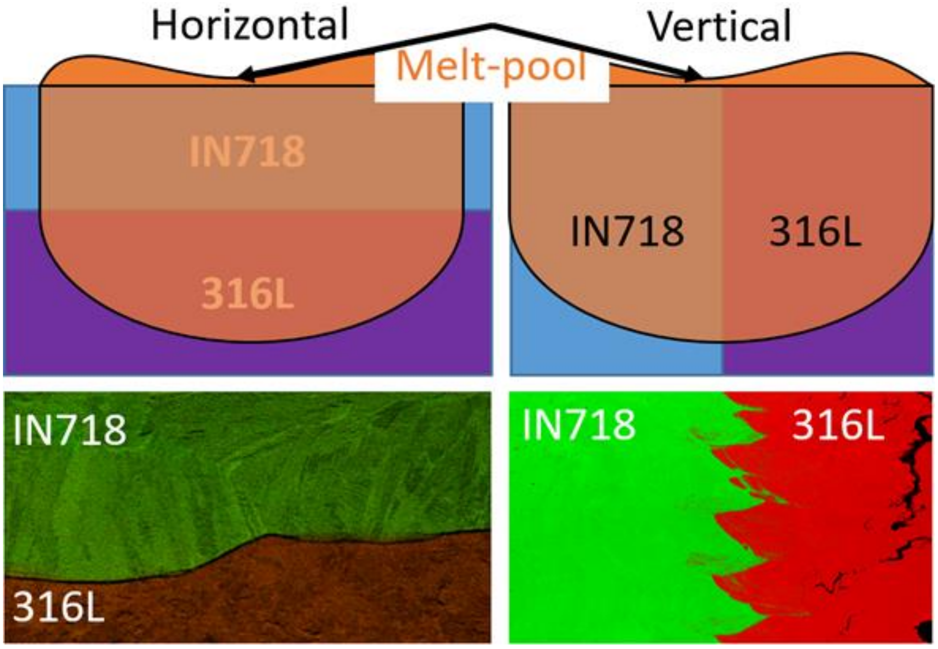

***Figure 64**. Single material zone orientation in relation to the melt-pool and final interface appearance.*

For IB interfaces, the structural evolution exhibits both sharp interfaces of HB and zig-zag interfaces of VB, depending on the deposition strategy. Sharp interfaces were formed for all DIBs regardless of the interface angle. This was the intended outcome of the deposition strategy, which included pre-machining the substrate to maintain consistent sharp interfaces at all interface angles. This was confirmed by the EDS line scan in **Figure 53**, which clearly shows a sudden change in Fe and Ni content. In contrast, the CIB interfaces exhibited closer resemblance to the zig-zag shape of VB, with this effect becoming more pronounced as the interface angle increased. Furthermore, the zig-zag shape of the interface, combined with the continuous deposition process, contributed to a step-like change in chemical composition across the interface. This is significantly different from the sharp interfaces of HB, where a sharp change in the chemical composition profile was exclusively observed. The correlation between one DED layer and the width of the step-like change in the EDS line profiles for all blocks and interfaces are summarized in **Table 13**. For all blocks, the melt-pool height was approximately 250 µm. This dimension is correlated with the compositional width change (CWC) for all blocks, except for VB, where the CWC is observed in the melt-pool width direction (approx. 800 µm). A noteworthy point is the comparison of compositional changes between the sharp and gradual interfaces of HB. In this regard, the CWC width is below the melt pool width for sharp interface (180 µm) but approximately 600 µm for gradual interface. This is attributed to the deep penetration effect of the laser when steel is deposited on nickel-based alloy. The CWC width is considerably larger for VB interfaces, corresponding to the width of a single melt-pool. A rather sharp CWC was observed for DIB interfaces, where the CWC was mostly within a distance below a single melt-pool height. This seems to be the result of pre-machining operation that might have beneficial effect on the discrete fusion line creation. For CIB blocks, the CWC size increased with the interface angle until it matched the CWC of VB for CIB45 and CIB60. Furthermore, for all CIB interfaces, a step-like CWC was monitored.

***Table 13**. Comparison of compositional width change across the interface for each FGM modification and dimension of the melt-pools.*

Interface type	Compositional width change (CWC)	Melt-pool height/width*
	µm	µm
HB sharp	180	250
HB gradual	600	250
VB	500-900	800*
DIB15	150	250
DIB30	280	250
DIB45	70	250
DIB60	70	250
CIB15	100	250
CIB30	160	250
CIB45	700	250
CIB60	900	250

EBSD analysis revealed that regardless of the interface type, the grains tend to grow perpendicular to the fusion line (HB and IB) or along the boundaries of the molten pool tracks (VB). Furthermore, epitaxial grain growth is a common occurrence, particularly in the curved grain regions near IN718, close to the interface zone of VB. In these areas, grains grow across multiple molten-pool tracks while maintaining the orientation of their neighbouring grains displayed in **Figure 65**. A significant discovery was made regarding the grain structure at the DIB interface, where an instantaneous refinement of IN718 grains was observed in **Figure 54**. Grain size changes were also noted with respect to the angle. In the case of DIB60, fine grains of IN718 were consistently observed along the entire length of the interface. This refinement effect appears to be linked to surface machining prior to deposition. This refinement could potentially have a positive strengthening effect on the interface zone, thereby improving mechanical behaviour. For example, it could enhance fatigue properties, reduce crack propagation rates across the interface, or improve strength properties by impeding dislocation movement.

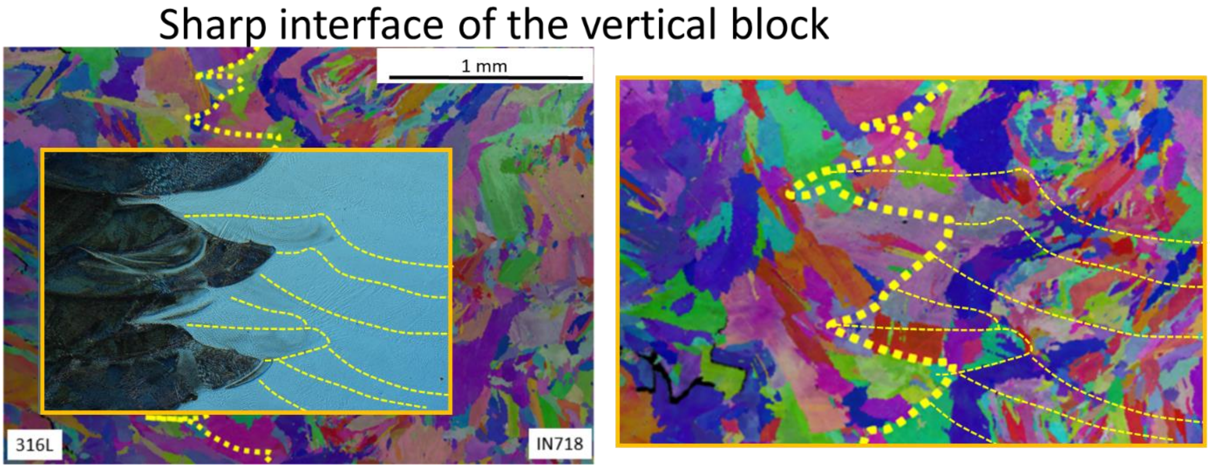

Figure 65*. Representation of the grain growth perpendicular to the molten pool tracks (yellow dashed line) and across multiple molten pool tracks with curved shape as a result of epitaxial growth at the sharp interface of vertical block.*

6.2 Porosity and defects formation

The structural observations unequivocally reveal that the formation of SCs and the evolution of porosity strongly depend on the material deposition sequence and the interface angle. The most critical disruption to structural integrity was detected for vertically oriented interfaces (VB) as shown in **Figure 27**, particularly at an interface angle of 60°. The size and concentration of defects also increase with the interface angle. Furthermore, the surface condition on which deposition takes place has a significant effect. Surface machining operations prior to deposition suppress the evolution of defects. SCs were primarily located near the interface on the 316L side in the case of VB. In some instances, their presence at the fusion line was confirmed by light microscopy (DIB60). These SCs propagated intergranularly. EDS line plots for the VB interface (**Figure 30**) were also used to determine the position of SCs with respect to the concentration of Ni and Fe. It was found that in sharp interface, cracks began to form at locations with approximately 15% Ni and 63% Fe. In the initial state of 316L stainless steel, a composition of 10% Ni and 68% Fe was measured. In gradual interface, the composition at the location of crack formation corresponded to approximately 14% Ni and 65% Fe. Line scans of the continuous IB showed that for 60° and 45° interfaces, cracks were exclusively present in the 316L area where the content of Fe and Ni remained stable. On the contrary, the SC formation was limited to the zone of mixture for HB gradual interface. These various locations of SCs indicate that the change in chemical composition across the interface is not the sole factor responsible for crack evolution in FGM.

Residual stresses, as a factor contributing to SC, were investigated by Hallberg [149]. They argued that the level of residual stresses formed at the melt-pool boundaries due to shrinkage is more critical for deeper and narrower melt-pools. However, in all deposited blocks within this study, no changes in melt-pool size and shape were observed between single-material zones and mixed gradual interfaces. Moreover, the only observed change in melt-pool size was consistently at the sharp interface. 316L melt-pools at the fusion line exhibited increased depth compared to previous layers; however, no cracking was observed in this case. Nonetheless, the unchanged melt-pool size does not rule out residual stresses as a contributing factor. Mixed zones, due to different laser inputs, undoubtedly undergo different thermal processing. Recent studies have reported that strain localization in materials with an FCC lattice leads to grain boundary sliding, preferential void formation, and cracking at the grain boundaries. Furthermore, SCs were observed to form at the interface between equiaxed dendrites and columnar dendrites. The transition from equiaxed to columnar dendrite appearance confirms the chemical imbalance in the mixed zone, resulting in thermal instability and the formation of residual stresses. The results clearly demonstrate that continuous deposition, leading to gradual chemical composition changes, likely increased residual stresses and different thermal history at the two-material interface, significantly contributes to the formation of SC.

Regardless of the location of cracks and other defects, a comparison of the porosity level at the interface zone among all FGM blocks is presented in **Figure 66**. For this analysis, all blocks were divided into two main groups. The first group consists of continuously deposited interfaces, including all CIB blocks, as well as HB and VB, since no surface treatment was applied before interface formation. The other group includes discontinuously deposited interfaces, comprising only DIB blocks where surface machining was employed. The results show that the continuous deposition strategy significantly increases the porosity level with increasing interface angle. For DIB interfaces, the porosity level remains stable at around 0.05% for angles between 15° and 45°, but there is an abrupt increase to approximately 0.5% at a 60° angle. Surface machining has the potential to remove detrimental features commonly present on the surface after L-DED processes, such as unmelted particles, various surface roughness (which depends on factors like feedstock material, deposition strategy, and energy density), porosity, surface defects (due to gas entrapment, insufficient fusion, or inadequate process control), and oxide formation. Properly adjusted surface conditions contribute beneficially to the formation of high-quality joints. On the contrary, the only comparable porosity level to DIB interfaces is found at a 15° interface angle for CIB (0.061%). Beyond 30°, porosity continuously increases, reaching 1% at the 60° interface, which is more than double the porosity of the DIB 60° interface. At a 60° angle, the interface appearance is very close to VB, but VB exhibits even higher porosity, exceeding 2%. At lower angles, when pre-machining is employed before IN718 deposition to clean the surface from unmelted particles, the process suppresses defects and improves material fusion. However, beyond a certain threshold (60°), the effectiveness of this effect diminishes, leading to defect formation. This is attributed to changes in surface tension and the loss of melt-pool stability. When material is deposited at a higher interface angle, surface tension forces can cause the material to bead up or form irregular structures, promoting pore and void formation. In other words, an inclined substrate can induce instability in the formed melt-pool of the deposited material and alter material flow. The best results in terms of defect concentration were recorded for the sharp interface of the HB block, where no SCs were observed, and the porosity level was very low (0.01%). Even without surface machining, the horizontal interface orientation benefits melt-pool stability and thermal history. The distinct separation of materials at the interface suppresses chemical imbalances in the otherwise gradually mixed interface area. Furthermore, discontinuous blocks exhibited porosity levels below 0.08% up to a 45° angle. In contrast, the porosity of continuous blocks rapidly increases with higher interface angles, exceeding 1% above 30° and reaching 60°. Summary of porosity values for each block is presented in **Table 14**.

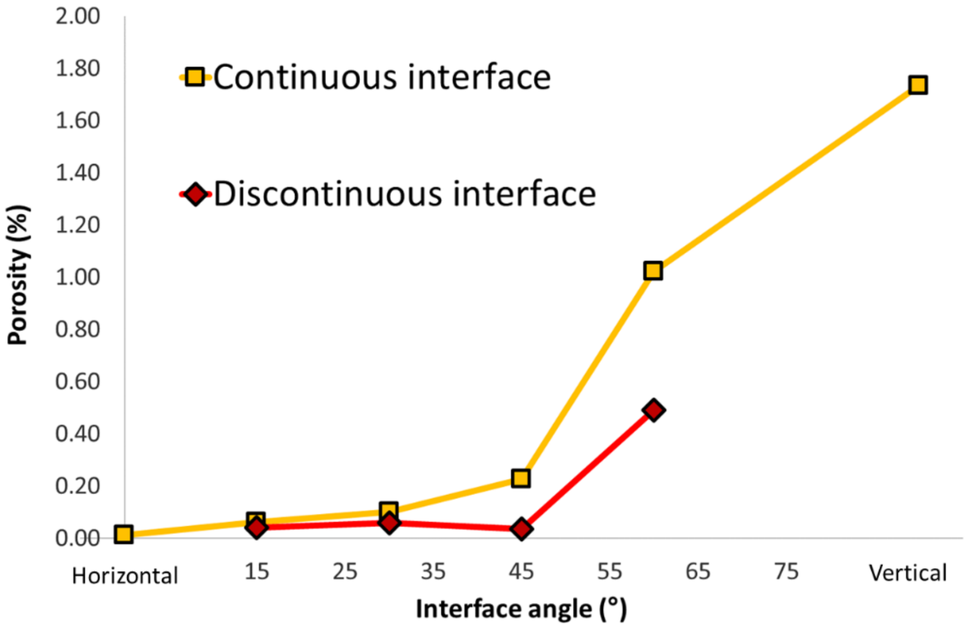

Figure 66. *Evolution of the porosity at the interface of FGM with respect to the interface orientation and application of pre-machining operation.*

Table 14. *Comparison of defects concentration between each FGM.*

Sample	**Binary Area Fraction/%**				
	Angle	Interface	316L SS	IN718	Whole
Horizontal	0	0.011	-	-	0.011
CIB15	15	0.062	0.042	0.051	0.048
CIB30	30	0.102	0.017	0.020	0.032
CIB45	45	0.227	0.052	0.075	0.086
CIB60	60	1.023	0.016	0.031	0.249
Vertical	90	1.735	-	-	0.450
DIB15	15	0.041	0.074	0.031	0.051
DIB30	30	0.058	0.050	0.081	0.067
DIB45	45	0.036	0.024	0.044	0.035
DIB60	60	0.491	0.023	0.056	0.210

6.3 Tensile characteristics comparison

A comparison of tensile test results among all FGM blocks is presented in the form of a column graph in **Figure 67**, showcasing yield strength, ultimate tensile strength, and elongation values. The graph is divided into two sections based on continuous or discontinuous material deposition, with each section sorted by interface angle in ascending order. Starting from the continuous block section, the most impressive performance in terms of tensile behaviour was observed in the sharp interface of HB, with an ultimate tensile strength (R_m) of 665.9 MPa, the highest value among all interface types. Additionally, the deviation of ±2.9 MPa is the smallest among all, indicating great repeatability. Immediately following the 15° inclination, CIB15 displayed a drop in R_m by approximately 100 MPa and $R_{p0.2}$ by 70 MPa. Despite both HB sharp and CIB15 specimens failing in the 316L area, locally formed SCs were observed in CIB15, which were responsible for the reduction in strength characteristics and elongation values. As the defect concentration increases with the angle, the most sensitive parameter appears to be elongation, which steadily decreases from 41% for HB to 8% for CIB60. On the other hand, strength values initially increase and then decrease, especially yield strength values. This is a consequence of two factors: increasing defect concentration and the variable distribution of materials within the tensile specimen body associated with the change in interface angle. All samples were produced in the vertical direction with ZYX orientation, but this is where the difference arises in the specimen's response to tensile load. This difference was demonstrated in Chapter 5.5, where the failure of sharp interfaces in vertically and horizontally oriented specimens was analysed. The results revealed that the load and deformation concentration are carried by different material zones depending on the specimen's orientation. In vertically oriented specimens (ZYX), 316L is the main tensile process zone, whereas in horizontally oriented specimens, IN718 is where the fracture process and tensile load occur. Specimens with inclined interfaces ranging from 15 to 60° represent intermediate steps between these two cases, where the behaviour of the samples gradually transitions from one to the other. Consequently, there is an initial increase in $R_{p0.2}$ due to the larger portion of the load being borne by IN718 for angles of 15, 30, and 45°. However, there is a decrease in strength for 60°, primarily due to the critical defects concentration, leading to early specimen failure. The early specimen failure results in the critical strength for failure being significantly lower, even though the portion of IN718 would theoretically yield a higher strength compared to previous interface angles. This is supported by the continuously decreasing elongation values across all inclinations. Considering that IN718 takes up a larger portion of the MTT specimens as the interface angle increases, the elongation should decrease correspondingly, as IN718 exhibits lower elongation compared to 316L. However, XYZ-oriented specimens from HB at the sharp interface yielded an elongation above 20%, significantly higher compared to CIB30-CIB60 specimens. This implies that the decrease in elongation for samples from CIB30 to CIB60 is a consequence of the higher proportion of defects and not the variable representation of IN718 in the test sample. Lastly, the continuously produced VB interface yielded the lowest elongation, around 3%, and an R_m below any $R_{p0.2}$ value of any previous continuous block. This is attributed to the critical development of SC, which had a detrimental effect on the tensile performance of the interface.

The right side of the graph, representing discontinuous blocks, exhibits a significant improvement in the trend of elongation values, ranging from 20% to 25% for DIB15 to DIB45. Only DIB60 shows a more noticeable decrease in elongation, although it remains higher than every elongation value observed for CIB30 to VB on the left side of the graph. $R_{p0.2}$ and R_m exhibit more stable values across the angle range, with a slight tendency for an increase as the interface angle goes from 15 to 60°. This trend aligns with the previously discussed influence of the interface angle on the tensile performance of MTT specimens. The results for DIB60 suggest that surface machining prior to IN718 deposition is beneficial for maintaining the consistency of tensile properties and the stability of the melt-pool, which in turn suppresses the formation of SC. The summary of tensile results for each block is presented in **Table 15**.

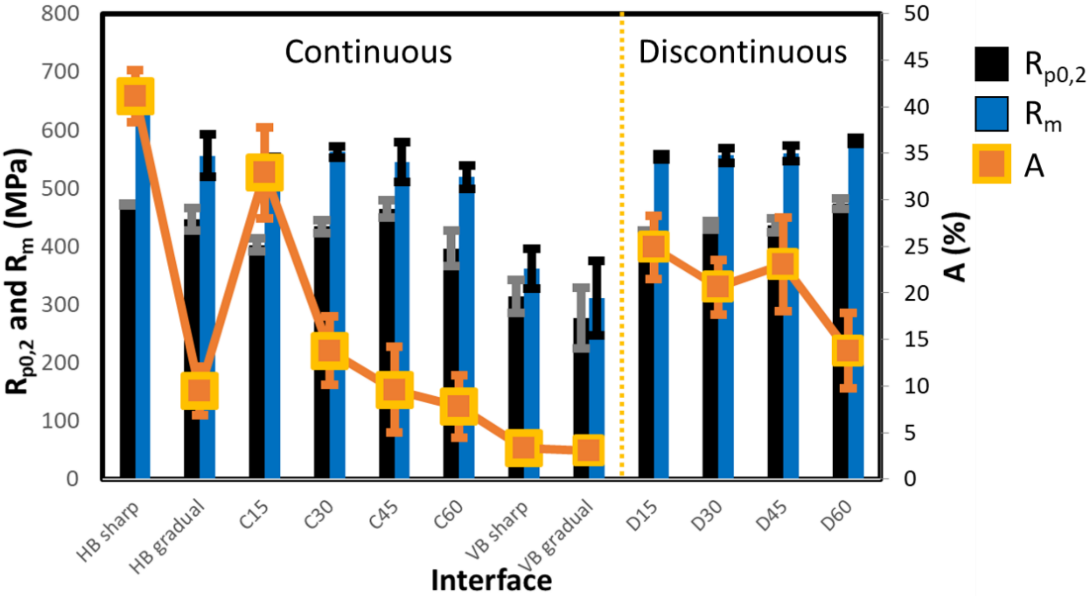

Figure 67. *Evolution of tensile properties with the interface orientation between 316L and IN718.*

***Table 15**. Summary of tensile parameters values for all FGMs.*

Deposition strategy	Interface	$R_{p0.2}$	±	R_m	±	A_g	±	A	±	Z	±
Continuous	**HB sharp**	**471.6**	**1.9**	**665.9**	**2.4**	**28.8**	**2.1**	**41.1**	**2.8**	**75.1**	**1.7**
	HB gradual	447.1	19.3	555.8	37	6.4	2	9.5	2.6	44.3	14.8
	CIB15	**402.4**	**10.6**	**543.0**	**10.0**	**21.6**	**3.7**	**32.9**	**4.9**	**67.1**	**14.1**
	CIB30	434.0	11.3	562.0	10.0	7.5	3.0	13.8	3.7	59.3	15.5
	CIB45	**464.3**	**15.1**	**545.0**	**34.0**	**4.7**	**2.6**	**9.6**	**4.6**	**49.7**	**11.1**
	CIB60	396.2	30.4	519.0	20.0	3.7	2.0	7.8	3.3	38.3	10.9
	VB sharp	313.6	28.7	361.1	34.0	1.6	0.6	3.3	1.4	18.5	6.3
	VB gradual	**276.2**	**52.3**	**311.2**	**64.3**	**1.4**	**0.5**	**3.0**	**0.6**	**16.3**	**4.1**
Discontinuous	**DIB15**	**422.8**	**4.5**	**554.1**	**4.6**	**16.1**	**1.4**	**24.9**	**3.4**	**67.9**	**4.1**
	DIB30	435.8	7.5	556.2	12.5	14.7	2.0	20.6	2.9	62.8	3.0
	DIB45	**435.8**	**11.9**	**559.3**	**13.1**	**15.9**	**2.5**	**23.1**	**5.0**	**63.0**	**3.6**
	DIB60	472.8	9.0	580.9	5.3	9.0	2.6	13.8	4.0	51.9	9.4

Table 16 provides a summary of tensile test results published in different studies for 316L and IN718 materials. The experimentally measured values within this thesis are marked with an asterisk (*). In the case of 316L, the R_m and $R_{p0.2}$ values are very similar to those reported in other studies. However, for IN718, the R_m and $R_{p0.2}$ values in the vertical orientation are lower compared to other studies, where IN718 exhibited roughly half of the elongation value. Nevertheless, in the current study, it appears that the tensile results of single-material layers are influenced by the interfaces across which the Multi-Material Tensile (MTT) specimens exhibit neck curvatures. For example, the results of ZYX_3 and ZYX_5 oriented MTT specimens made of 316L material are in good agreement with the results of MTT specimens from gradual transition ZYX_2–3 and ZYX_4–5 (represented by green bars in **Figure 18**). These results suggest that the strength and elongation values for specimens extracted from a single material layer in ZYX orientation might be distorted by the influence of the interfaces, thereby affecting the overall performance of the MTT specimens. A similar effect was observed for single material layer number 4 of IN718, which consistently exhibited lower tensile values compared to layers 2 and 6. This observation is in agreement with results of study conducted by [100], tensile tests were performed on specimens with both directly joined and gradient path interfaces between 316L and IN718. The fracture positions were analysed. The results revealed that in instances of directly joined materials, fractures occurred on the 316L side in close proximity to the interface. On the other hand, for the gradient path interface, fractures transpired at the

two-material transition, specifically on the side nearer to the 316L side, with 316L/IN718 ratios of 75/25 and 70/30.

***Table 16**. Comparison of tensile results for individual materials and interface with chosen literature data.*

Material zone	**Material**	**Process**	**Orientation**		**$R_{p0.2}$**	**R_m**	**A_g**	**A**	**Z**	**Ref.**
					MPa	MPa	%	%	%	
Single material	**316L VB***	BP DED	YZX	Horizontal	446±24	640±15	29±6	40±9	74±4	[143]
			ZYX	Vertical	406±21	603±39	33±10	43±13	77±4	
	316L HB*	BP DED	XYZ	Horizontal	474±11	673±11	33±1	47±3	73±1	[142]
			YXZ		493±11	689±15	32±3	46±3	72±3	
			ZYX	Vertical	453±11	559±7	9±1	11±0.1	42±4	
	316L	Laser Cladding Deposition (LCD)	-	-	300-440	550 - 660	-	42	-	[44]
			-	-	-	-	-	-	-	
	316L	Laser Metal Deposition (LMD)	-	Horizontal	500 - 600	625 - 695	-	20 - 25	-	[45]
	316L	High Power Direct Laser Deposition (HP DLD)	-	Horizontal	580	900	-	4	-	[42]
			-	Vertical	415	770	-	4.5	-	
	316	LENS		Vertical	285	557	-	45	-	[84]
	IN718 VB*	BP DED	YZX	Horizontal	562±16	877±34	19±3	22±4	41±5	[143]
			ZYX	Vertical	493±13	834±21	27±4	31±5	46±4	
	IN718 HB*	BP DED	XYZ	Horizontal	608±10	948±13	21±0.3	24±0.5	41±2	[142]
			YXZ		632±13	972±6	21±1	24±1	41±1	
			ZYX	Vertical	517±7	829±41	22±7	23±8	76±1	
	IN718	DED	-	Horizontal	-	-	-	-	-	[46]
			-	Vertical	650	1000	-	-	38	
	IN718	DED	-	Horizontal	-	-	-	-	-	[150]
			-	Vertical	590	845	-	11	26	
Interfaces	**HB sharp***	BP DED	ZYX	Vertical	472±2	666±2	29±2	41±3	75±2	[142]
	HB gradual*	BP DED	ZYX	Vertical	447±19	556±37	6±2	10±3	44±15	
	C15*	BP DED	ZYX	Vertical	402±11	543±10	22±4	33±5	67±14	[144]
	C30*	BP DED	ZYX	Vertical	434±11	562±10	8±3	14±4	60±16	
	C45*	BP DED	ZYX	Vertical	464±15	545±34	5±3	10±5	50±11	
	C60*	BP DED	ZYX	Vertical	396±30	519±20	4±2	8±3	38±11	
	Sharp VB*	BP DED	YZX	Horizontal	313±29	361±34	2±1	3±1	19±6	[143]
	Gradual VB*	BP DED	YZX	Horizontal	276±52	311±64	1±1	3±1	16±4	
	D15*	BP DED	YZX	Vertical	423±5	554±5	16±1	25±3	68±4	[144]
	D30*	BP DED	YZX	Vertical	436±8	556±13	15±2	21±3	63±3	
	D45*	BP DED	YZX	Vertical	436±12	560±13	16±3	23±5	63±4	
	D60*	BP DED	YZX	Vertical	473±9	581±5	9±3	14±4	52±9	
	Discrete	LENS	-	Vertical	285	539	-	35	-	[84]
	Gradient	LENS	-	Vertical	306	537	-	31	-	
	Gradient	LDMD	-	Vertical	823	1030	-	2	-	[88]
	Discrete	DED	-	Vertical	398±33	564±31		(10-15)		[87]

6.4 Crack propagation across the interfaces

The mechanism of crack propagation in the ductile mode was evaluated for crack growth across the interfaces of HB. Crack propagation across the sharp interface from 316L to IN718 is illustrated by the J-R curve in **Figure 20**, using green square and circle data points. Initially, the shape of the J-R curve closely resembled that measured for the 316L area. However, as the crack extended into the sharp interface, a rapid decrease in the loading force and significant crack length extension were observed. After the instability occurred, the crack propagation mechanism returned to a stable ductile mode within the IN718 area. This sudden change in fracture behaviour is attributed to the rapid transition between different materials and their varying crack growth resistance. The abrupt change in fracture behaviour may be linked to the value of the J-integral at the moment when the ductile crack enters the material on the other side of the interface. In the transition from 316L to IN718, the energy input in the specimen required for crack propagation in 316L exceeded the maximum capacity of IN718. This value, approximately 650 kJ/m^2, was twice that of IN718 for a corresponding ductile crack extension. Consequently, the excess energy in the system was released through rapid cracking, as evidenced by the drop in force accompanied by a corresponding CMOD opening. Once the input energy was consumed by crack growth and the formation of a new surface, the crack extension mode returned to ductile when further loading of the specimen was necessary for additional ductile crack growth within the IN718 area. In the case of crack growth from IN718 to 316L, represented by the dark blue R-curve, the material transition exhibited a gradual increase in fracture resistance as the crack entered the 316L area. In this scenario, no unpredictable behaviour was expected since the crack growth was oriented from a less fracture-resistant material to a more resistant one.

In the conventional J–R curve theory, the trend can typically be divided into two parts. Initially, when the relationship between energy and crack extension is linear, it corresponds to the crack blunting process, during which the crack demands a progressively higher input of energy for further growth. The slope during this phase corresponds to the constructed blunting line, which is based on the characteristic strength properties [151]. Once a noticeable decrease in slope is observed, the crack tearing process is considered. These principles of ductile crack extension are clearly visible in the J-R curves for single-material zones, particularly for IN718. Below, J-R curves specific to interfaces were plotted, and it's evident that the linear part of the R-curve for both sharp and gradual interfaces occupies a very small portion of the R-curve, making it barely observable. This indicates that the crack blunting process was highly limited for these specimens, and the crack tearing process began almost immediately in the test. The fractography of MCT specimens revealed that the fracture surfaces located at the interfaces were heavily occupied by defects. As a result, significant attention was devoted to tracking the precise path of crack growth, especially for VB. From the images of the broken halves of the MCT specimens, it's clear that, for the VB MCT specimens, the direction of crack growth was deflected from its original path. While the crack's origin was located at the interface, the high concentration of SCs within the 316L material caused the crack to continue extending along the weakest direction. This observation mirrors what was noted in the MTT results, where interface zones influenced tensile results for specific specimens within single-material zones. The fracture toughness results of HB and VB blocks are summarized in **Table 17**.

***Table 17**. Summary of fracture toughness results for individual materials and interfaces of HB and VB.*

Material	**Process**	**Orientation**	**K_{JQ}** MPa·$m^{1/2}$	**Ref.**
316L VB	BP DED	YZS	**231±7**	[143]
316L HB	BP DED	ZYM	281±2	[142]
		YZS	268±2	
IN718 VB	BP DED	YZS	**212±8**	[143]
IN718 HB	BP DED	ZYM	201±3	[142]
		YZS	172±18	
VB Sharp	BP DED	ZYM	114	[143]
VB gradual			125	
HB sharp	BP DED	ZYM	148	[142]
HB gradual			131	
316L	Conventionally processed	-	270-280	[152]
IN718	Conventionally processed	-	120	[152]
IN718	Conventionally processed	-	100-200	[153]
IN718	EB_PBF	XZM	166	[154]
		XZE	145	

7 Conclusions

The objective of this thesis was to conduct an in-depth investigation of functionally graded materials (FGM) created through the combination of stainless steel 316L and the nickel-based superalloy Inconel 718, manufactured via directed energy deposition. The research focused on assessing the structural properties, defects formation, tensile strength, and fracture toughness properties of these experimental materials at the conditions of room temperature and in as deposited state. Characterization was carried out using miniaturized specimens, and the study encompassed four sets of FGM modifications categorized based on interface orientation. These modifications included horizontal block, vertical block, and inclined blocks with interface angles of 15, 30, 45, and 60°, each with continuous deposition and pre-machined surface treatments.

7.1 Summary of research achievements

The main findings of the thesis are based on the seven main points of the experimental program listed in chapter 4 are as follows:

- Examination of the influence of the sequence of deposited base materials on the nature of the multi-material interface:

Microstructural analysis revealed the presence of two types of interfaces based on the order of deposited materials. When IN718 was deposited on 316L in horizontally oriented interfaces, a rather sharp interface with an unequivocal fusion line was created. In contrast, a gradual interface with a mixture of combined materials within the melt-pools was observed when 316L was deposited on IN718. The extent of mixing depended on the applied laser power for each material, which, in turn, was influenced by the melting point of the constituents. Vertically oriented interfaces, regardless of the order of material deposition, exhibited characteristics of gradual interfaces. The primary difference appeared to be the width of the mixed zone, as observed in the etched structure of the interface.

- Correlation between the compositional width change across the interface and its type:

The measurement of compositional width change (CWC) for Fe and Ni revealed several distinct patterns. For horizontal interfaces, CWC of 180 µm for sharp and 600 µm for gradient interfaces were measured. Height of the melt pool was 250 µm for both, sharp and gradual interface. In contrast, vertical interfaces exhibited a CWC from 500 – 900 µm in width, while the width of the melt pool was approximately 800 µm. As a result of surface machining, discontinuous inclined interfaces displayed CWC values similar to those of horizontal interfaces or potentially much smaller CWC with a width of 70 µm. Continuous inclined interfaces demonstrated a clear trend of increasing CWC with interface angle, ranging from 100 to 900 µm.

- Correlation between the type of multi-material interface and the occurrence of defects:

The investigation into defects clearly revealed that the formation of solidification cracks depends on the proportion of the two primary constituents within the melt-pool at the interface. As a result, a crack-free structure was observed in the sharp interface of horizontal blocks, while some cracks were present in gradual interfaces. The presence of material mixture within the melt-pool emerged as the key factor contributing to the development of solidification cracks. This phenomenon arises from chemical instability due to imperfect mixing of the constituents, resulting in cracks between fine cellular structures and dendritic structures. Vertical interfaces exhibited a critical level of solidification cracks. In continuously manufactured inclined interfaces, there was an observable increase in both the size and concentration of defects with higher interface angles. The formation of these cracks was attributed to changes in surface tension and a loss of melt-pool stability. When materials are deposited at steeper interface angles, surface tension forces can cause the material to bead up or form irregular structures, thereby promoting the formation of pores and voids.

- Effect of surface treatment prior the dissimilar interface deposition on the defect formation:

Surface machining of the 316L part before IN718 deposition was carried out to assess defects formation and the mechanical performance of the interface. The results revealed that this machining operation enhances the stability of the melt-pools at the interface and reduces the likelihood of solidification crack formation at the interface.

This improvement was corroborated through fractography of Miniaturized Tensile Test specimens, porosity measurements, and the performance of the interfaces in tensile testing.

- Exploration of the limitations and advantages of employing miniaturized testing techniques for FGM characterization:

Miniaturized tensile tests and miniaturized fracture toughness tests were utilized for the mechanical characterization of various interfaces. All specimens provided reliable results with excellent repeatability when the entire specimen body was extracted from a single material zone. However, when MTT or Mini compact tension specimens spanned the interface, the presence of defects near the interface could affect the specimen's behaviour. For example, vertically oriented MTT specimens with their bodies within a single material zone but with neck curvatures and shoulders crossing the interfaces exhibited tensile results similar to those of interface-located MTT specimens. This similarity occurred because the specimens failed at the weakest point of the material. Similarly, the fracture toughness tests of MCT specimens located at the interface were influenced by the presence of solidification cracks within the 316L zone. The plane of crack extension was deflected from its original direction towards the weakened zone affected by solidification cracks. These examples illustrate that while miniaturized specimens are suitable for measuring local mechanical properties of FGM materials, their placement within the FGM structure must be carefully considered to reliably assess material behaviour. Despite these considerations, mechanical test results based on miniaturized specimens exhibited excellent repeatability when measuring tensile and fracture parameters within single material zones and interfaces. They are also suitable for demonstrating trends in evaluated parameters across the range of investigated FGMs.

- Comparative analysis of mechanical test outcomes across different block modifications:

The investigation into the mechanical behaviour of all FGM blocks revealed that, considering various interface orientations, the horizontally oriented interface exhibited the best performance in terms of tensile behaviour and defects formation. In contrast, the vertically oriented interface represented the worst-case scenario due to a significant reduction in structural integrity caused by the formation of solidification cracks within the 316L zone. For inclined interfaces, the most representative parameter for assessing interface performance quality was elongation, which exhibited a clear decreasing trend with increasing interface angle. The machining operation conducted prior to material deposition improved the mechanical performance of the interface and stabilized the elongation parameter for interface angles ranging from 15° to 45°.

- Investigation into the tensile failure of interface:

The sharp horizontal interface exhibited the highest tensile performance, and its failure mechanism was analysed using digital image correlation and Fractography. Both vertically and horizontally oriented tensile specimens spanning the interface were analysed. The results revealed that the load and deformation were concentrated in different material zones depending on the specimen's orientation. In vertically oriented specimens (ZYX), 316L served as the primary tensile process zone, while in horizontally oriented specimens, IN718 played this role, accommodating the fracture process and tensile load. This finding holds significance when considering the loading mode of real FGM components that combine 316L and IN718.

7.2 Contribution to the scientific discipline

The main findings of presented dissertation extended the current knowledge about FGM manufactured using L-DED. Most significant contribution is the interface orientation dedicated research, that for metallic FGM is unique. Setting the limitation of L-DED process in terms of interface orientation, was important aspect that directly affects the production process of FGM. No less important findings that expand scientific knowledge include a section dedicated to the influence of surface condition on defect formation. These insights broaden understanding of the patterns of defect formation at material interfaces formed through AM even under extreme conditions such as varying orientation of material interfaces. Furthermore, the description of failure mechanisms under mechanical loading provides a detailed analysis, offering a tool for potential prediction of material failure, crack propagation, and the location of its initiation under different orientations of material interfaces.

7.3 Contribution to practice

The main findings of the thesis reflect the limitations associated with using DED for repair applications of components and Functionally Graded Material production. While depositing layers from a single material type is mostly problem-free, issues arise in areas where different materials are mixed. The instability of material flow in the melt-pool and local chemical imbalances create a predisposition for the formation of defects and cracks, significantly compromising the material's performance during mechanical testing. When using DED technology for component repair, it is crucial to pay attention to the orientation of deposition planes. Deviations from the ideal horizontal direction should be carefully considered, and vertical orientations should be avoided entirely. Study showed that the liquid flow and melt-pool stability are negatively affected with increasing slope of the fusion line. Finally, proper surface preparation, including machining operations, should be employed when component repair is conducted. This stabilizes the conditions at the substrate-newly deposited layer interface and mitigates the formation of defects, even in cases where interfaces deviate from the horizontal plane by up to 45°.

7.4 Recommendations for further research

The thesis managed to describe the principles in the construction of chemically graded composites considering various orientation of the fusion lines. The main findings of the work are valuable not only for the specific material combination that was investigated, but under the constraint of using different materials can serve as a reference case, on which basis a new structures with direct application potential are investigated.

The results kept opened several other areas that should be investigated following the presented results. For instance, life assessment and fatigue behaviour of chemically graded components remains to be investigated. Study investigated the material failure behaviour at quasi-static loading conditions. Thus, fatigue regime of loading should follow to evaluate whether the principles of FGM failure follow those in the presented study. The grain structure is a critical factor for fatigue crack growth mechanism of material. Microstructural investigation of FGM revealed differences of grain size between homogeneous and interface zones. Specifically, it is a refinement of the grain in the area of the fusion line and change of grains orientation. These structural changes might have effect on the stability of propagated fatigue crack within the FGM.

8 Závěr

Hlavním cílem předložené disertační práce bylo provést detailní výzkum funkčně gradovaného materiálu FGM, vytvořeného kombinací korozivzdorné oceli 316L a niklové superslitiny Inconel 718, deponovanými metodou přímé depozice DED. Výzkum byl cílen na charakterizaci strukturních vlastností, hodnocení podmínek vzniku vnitřních defektů, hodnocení mechanické odezvy při jednoosém zatěžování a hodnocení lomových vlastností při podmínkách quasi-statického zatěžování za pokojové teploty ve stavu po depozici. Mechanické charakteristiky byly hodnocené pomocí miniaturizovaných zkušebních těles, které byly extrahovány ze čtyř typově odlišných FGM modifikací, lišícími se orientací materiálového rozhraní. Mezi tyto modifikace patřily: horizontální blok, vertikální blok a bloky „nakloněné“, u nichž byl úhel rozhraní o náklonu 15, 30, 45 a 60 °. Nakloněné bloky byly dále rozdělené na dvě skupiny dle metodiky výroby: průběžně deponované a před obrobené.

8.1 Souhrn dosažených výsledků výzkumu

Hlavní výsledky disertační práce vycházejí ze stanovených cílů v kapitole 3 a náplně experimentálního programu, který byl stanoven v kapitole 4.

- Hodnocení vlivu střídavé depozice kombinovaných materiálů na vlastnosti materiálového rozhraní:

Mikrostrukturní analýzy odhalily přítomnost dvou rozdílných typů rozhraní v závislosti na pořadí deponovaných materiálů. Pro případ depozice niklové slitiny na ocel v horizontální orientaci vzniklo diskrétní rozhraní s jednoznačně vyhraněnými oblastmi jednotlivých materiálů a rozpoznatelnou ostrou hranicí. Oproti tomu, rozhraní s postupným přechodem a výrazně širší oblastí promíšení rozdílných materiálů, ve které docházelo k postupné změně jednoho materiálu v druhý, bylo pozorováno pro případ depozice oceli na niklovou slitinu. Úroveň promíšení materiálů byla závislá na použitém výkonu laseru. Tento výkon byl pro každý materiál nastaven odlišně s ohledem na rozdílnou teplotu tání. Vertikálně orientovaná rozhraní, bez ohledu na pořadí depozice materiálů, vykazovaly charakteristiky postupných rozhraní. Hlavní rozdíl mezi horizontální a vertikální orientací byl v šířce zóny promíšení, která byla výrazně širší pro vertikálně orientované rozhraní.

- Korelace mezi šířkou změny chemického složení na rozhraní a typu rozhraní:

Přímé měření šířky změny chemického složení (CWC) na rozhraních pomocí EDS liniového skenu pro prvky Fe a Ni odhalilo následující. Pro horizontální ostré rozhraní byla CWC o šířce 180 μm a 600 μm pro postupný přechod. Výška tavné lázně byla pro obě rozhraní 250 μm. Oproti tomu, CWC pro vertikální rozhraní bylo v rozsahu od 500–900 μm, zatímco šířka tavné lázně byla zhruba 800 μm. Diskontinuální nakloněná rozhraní vykazovala hodnoty CWC podobné horizontálním rozhraním nebo potenciálně mnohem menší CWC se šířkou 70 μm. Kontinuální nakloněná rozhraní prokázala jasnou tendenci k zvýšení CWC s úhlem rozhraní, pohybující se od 100 do 900 μm.

- Korelace mezi orientací rozhraní a výskytem vad:

Vyšetřování vad jednoznačně ukázalo, že tvorba solidifikačních trhlin závisí na poměru dvou hlavních složek v oblasti natavení na rozhraní. To znamená, že struktura bez solidifakčních trhlin byla pozorována pro ostré rozhraní horizontálního bloku, zatímco v rozhraních s vyšší úrovní promíšení byly trhliny pozorovány. Přítomnost směsi materiálu v oblasti natavení se ukázala jako klíčový faktor přispívající k tvorbě solidifikačních trhlin. Tento jev vzniká v důsledku chemické nestability nedokonalým promíšením složek, což má za následek vznik trhlin mezi jemnými buněčnými strukturami oceli a dendritickými strukturami niklové slitiny. Vertikální rozhraní vykazovala kritickou úroveň vzniku solidifikačních trhlin vznikajících intergranulárně. U nepřetržitě vyráběných nakloněných rozhraní byl pozorován nárůst jak velikosti, tak koncentrace vad s rostoucím úhlem náklonu rozhraní. Tvorba těchto trhlin byla přičítána změnám povrchového napětí a ztrátě stability svarové lázně. Když jsou materiály ukládány pod strmějšími úhly rozhraní, povrchové napětí může způsobit shlukování materiálu nebo tvorbu nepravidelných struktur, čímž je vznikají podmínky podporující tvorbu pórů a dutin.

- Vliv úpravy povrchu před depozicí odlišného rozhraní na tvorbu vad:

Část bloku z oceli 316L byla obrobena před depozicí niklové slitiny Inconel 718 pro posouzení vlivu na tvorbu vad a odezvu na mechanické zatížení rozhraní. Výsledky ukázaly, že před obrobení zlepšuje stabilitu tavných lázní na rozhraní a snižuje pravděpodobnost tvorby solidifikačních trhlin na rozhraní. Toto zlepšení bylo potvrzeno fraktografií, zkouškami tahem na zmenšených vzorcích a měřením pórovitosti.

- Průzkum výhod a nevýhod používání miniaturizovaných testovacích technik pro charakterizaci FGM:

V disertační práci byly využité miniaturizované tahové vzorky (MTT) a miniaturizované vzorky pro zkoušku lomové houževnatosti (MCT) pro hodnocení jednotlivých materiálů a rozdílných rozhraní. Všechny vzorky, které byly extrahované z oblasti jednoho materiálu poskytovaly výsledky s dobrou opakovatelností a relativně malými rozptyly vyhodnocených charakteristik. Nicméně, když MTT nebo MCT vzorky byly extrahované v rozhraní mezi materiály, přítomnost vad poblíž rozhraní ovlivňovala výsledné hodnoty. Například MTT vzorky s tělem umístěným v jedné materiálové zóně, ale hlavami v jiné materiálové zóně, vykazovaly tahové výsledky podobné těm vzorkům MTT, jejichž tělo bylo umístěno na rozhraní cíleně. Tato podobnost nastávala proto, že vzorky selhaly v nejslabším bodě materiálu. Což byla právě rozhraní oslabená přítomnými defekty. Obdobně testy lomové houževnatosti MCT vzorků umístěných na rozhraní byly ovlivněny přítomností solidifikačních trhlin v zóně 316L. Rovina šíření trhliny byla odchýlena od svého původního směru do roviny oslabené solidifikačními trhlinami. Tyto příklady ilustrují, že zatímco miniaturizované vzorky jsou vhodné pro měření lokálních mechanických vlastností FGM materiálů, jejich umístění uvnitř FGM struktury musí být pečlivě zváženo, a především známo, aby bylo možné spolehlivě posoudit chování materiálu a byl jednoznačně stanovený vztah mezi strukturou a mechanickými vlastnostmi.

- Srovnávací analýza výsledků mechanických testů mezi různými modifikacemi bloků:

Výsledky tahových zkoušek všech bloků FGM odhalily, že při zohlednění různých orientací rozhraní vykazovalo horizontálně orientované rozhraní nejlepší tahové vlastnosti. Naopak, vertikálně orientované rozhraní představovalo nejhorší možný scénář kvůli významné redukci strukturální integrity způsobené tvorbou solidifikačních trhlin v oblasti 316L. U nakloněných rozhraní byl nejreprezentativnějším parametrem pro posouzení kvality výkonu rozhraní prodloužení, které vykazovalo jasně klesající trend s rostoucím úhlem rozhraní. Obráběcí operace provedená před depozicí materiálu výrazně zlepšila tahové vlastnosti a soudržnost materiálů na rozhraních o náklonu 15°, 30 ° a 45 °.

- Hodnocení módu porušení horizontálního rozhraní při tahovém zatížení

Ostré horizontální rozhraní prokázalo nejvyšší tahový výkon a jeho mechanismus selhání byl analyzován pomocí digitální korelace obrazu a fraktografie. Byly analyzovány jak vertikálně, tak horizontálně orientované tahové vzorky, které překračovaly rozhraní. Výsledky ukázaly, že zatížení a deformace byly soustředěny v různých materiálových zónách v závislosti na orientaci vzorku. Ve vertikálně orientovaných vzorcích (ZYX) sloužila 316L jako hlavní zóna pro tahový proces a koncentraci napětí, zatímco pro horizontálně orientované vzorky bylo napětí přenášeno především oblastí Inconelu 718, kde docházelo ke vzniku lomu. Tento nález má význam při zohlednění způsobu zatěžování reálných komponent FGM, které kombinují 316L a IN718, případně jiné materiály s odlišnými pevnostními vlastnostmi.

8.2 Přínos pro vědní obor

Vytyčené cíle disertační práce rozšiřují dosavadní vědecké poznání o zkoumané problematice výroby funkčně gradovaných materiálů pomocí L-DED. Nejvíce významným příspěvkem je výzkum věnovaný vlivu orientace materiálového rozhraní, který je pro kovové FGM materiály zcela unikátní. V rámci této části byly stanovené okrajové podmínky použitelnosti L-DED v případě proměnné orientace rozhraní. Neméně důležitými poznatky, které rozšiřují vědecké poznání, se týkají části věnované vlivu stavu povrchu na vznik defektů. Tyto poznatky rozšiřují znalosti o zákonitostech vzniku defektů na materiálovém rozhraní vzniklém pomocí AM a to i při extrémních podmínkách jako je právě rozdílná orientace materiálového rozhraní. Popis mechanismu porušení při mechanickém zatížení zase nabízí detailní analýzu, která poskytuje nástroj k možné predikci porušení materiálu, šíření trhliny a místa jejího vzniku při různých orientacích materiálového rozhraní.

8.3 Přínos pro praxi

Hlavní zjištění této práce odrážejí omezení spojená s použitím DED pro opravy komponentů a výrobu materiálů s funkčním gradientem. Zatímco nanášení vrstev z jednoho typu materiálu je většinou bezproblémové, problémy vznikají v oblastech, kde dochází k míšení různých materiálů. Nestabilita toku materiálu v tavné lázni a místní chemické nerovnováhy vytvářejí předpoklady pro tvorbu vad a trhlin, což významně oslabuje výkonnost materiálu během mechanických testů. Při použití technologie DED pro opravu komponentů je důležité věnovat pozornost orientaci rovin depozice. Odklon od ideální horizontální orientace by mělo být pečlivě zvažováno a vertikální orientace by měla být zcela vyloučena. Studie ukázala, že materiálový tok a stabilita tavné lázně jsou negativně ovlivněny s rostoucím sklonem rozhraní mezi materiály. Při opravách reálných komponent by také mělo být provedeno vhodné ošetření povrchu, včetně obráběcích operací, které na základě výsledků studie mohou mít příznivý vliv na stabilitu tavné lázně a výrazně snížení množství vnitřních defektů. Obrobení povrchu stabilizuje podmínky na rozhraní mezi podkladem a nově uloženou vrstvou i v případech, kdy se rozhraní odklání od horizontální roviny až o 45°.

8.4 Doporučení na další výzkum

V této disertační práci se podařilo popsat principy při výrobě chemicky gradientních kompozitů s ohledem na různou orientaci rozhraní mezi chemicky rozdílnými materiály. Hlavní zjištění práce jsou cenná nejen pro konkrétní kombinaci materiálů, které byly zkoumány, ale mohou sloužit jako reference pro použití kombinace jiných materiálů, které by měly vyšší potenciál pro přímou aplikaci v technické praxi. Výsledky také otevřely několik dalších oblastí, které by měly být zkoumány na základě dosavadních prezentovaných výsledků. Například hodnocení životnosti a únavového chování chemicky gradientních komponent je veliká oblast, které by měla být věnovaná pozornost. Studie zkoumala chování materiálu při kvazi-statických podmínkách zatížení. Proto by mělo následovat zkoumání chování v režimu únavového zatěžování, aby bylo možné zhodnotit, zda principy selhání FGM odpovídají těm v prezentované studii. Zrnitá struktura je klíčovým faktorem mechanismu růstu únavové trhliny materiálu. Mikrostrukturní zkoumání FGM odhalilo rozdíly ve velikosti zrna napříč rozhraními rozdílných materiálů. Konkrétně jde o zjemnění zrna v oblasti spoje a změnu orientace zrn. Tyto strukturální změny by mohly mít vliv na stabilitu šíření únavové trhliny uvnitř FGM.

9 References

[1] T. Wohlers and T. Gornet, “History of Additive Manufacturing 2014,” *Wohlers Rep. 2014 - 3D Print. Addit. Manuf. State Ind.*, 2014.

[2] ISO/ASTM, “ISO/ASTM 52909: Additive manufacturing of metals — Finished part properties — Orientation and location dependence of mechanical properties for metal powder bed fusion,” *Int. Stand.*, 2022.

[3] Additive Manufacturing Research Group, “The 7 Categories of Additive Manufacturing,” *Loughborough University*, 2018. .

[4] T. Wohlers, “Wohlers Report 2023 Analysis. Trends. Forecasts. 3D Printing and Additive Manufacturing State of the Industry.,” 2023.

[5] O. Abdulhameed, A. Al-Ahmari, W. Ameen, and S. H. Mian, “Additive manufacturing: Challenges, trends, and applications,” *Adv. Mech. Eng.*, 2019, doi: 10.1177/1687814018822880.

[6] M. Armstrong, H. Mehrabi, and N. Naveed, “An overview of modern metal additive manufacturing technology,” *Journal of Manufacturing Processes*. 2022, doi: 10.1016/j.jmapro.2022.10.060.

[7] J. Zhu et al., “A review of topology optimization for additive manufacturing: Status and challenges,” *Chinese Journal of Aeronautics*. 2021, doi: 10.1016/j.cja.2020.09.020.

[8] C. Sun et al., “Additive manufacturing for energy: A review,” *Appl. Energy*, 2021, doi: 10.1016/j.apenergy.2020.116041.

[9] B. Saleh *et al.*, “30 Years of functionally graded materials: An overview of manufacturing methods, Applications and Future Challenges,” *Composites Part B: Engineering*. 2020, doi: 10.1016/j.compositesb.2020.108376.

[10] I. Gibson, D. W. Rosen, and B. Stucker, *Additive manufacturing technologies: Rapid prototyping to direct digital manufacturing*. 2010.

[11] J. Byskov and N. Vedel-Smit, “Additive manufacturing,” in *The Future of Smart Production for SMEs: A Methodological and Practical Approach Towards Digitalization in SMEs*, 2022.

[12] B. Blakey-Milner *et al.*, “Metal additive manufacturing in aerospace: A review,” *Mater. Des.*, 2021, doi: 10.1016/j.matdes.2021.110008.

[13] G. Liu *et al.*, “Additive manufacturing of structural materials,” *Materials Science and Engineering R: Reports*. 2021, doi: 10.1016/j.mser.2020.100596.

[14] M. Javaid, A. Haleem, R. P. Singh, R. Suman, and S. Rab, “Role of additive manufacturing applications towards environmental sustainability,” *Advanced Industrial and Engineering Polymer Research*. 2021, doi: 10.1016/j.aiepr.2021.07.005.

[15] T. DebRoy *et al.*, “Additive manufacturing of metallic components – Process, structure and properties,” *Prog. Mater. Sci.*, vol. 92, pp. 112–224, 2018, doi: https://doi.org/10.1016/j.pmatsci.2017.10.001.

[16] H. Salem, H. Abouchadi, and K. El Bikri, “Design for additive manufacturing,” *J. Theor. Appl. Inf. Technol.*, 2020, doi: 10.1201/9780429466236-7.

[17] M. Brandt, *Laser additive manufacturing: Materials, design, technologies, and applications*. 2016.

[18] K. S. Prakash, T. Nancharaih, and V. V. S. Rao, “Additive Manufacturing Techniques in Manufacturing -An Overview,” 2018, doi: 10.1016/j.matpr.2017.11.642.

[19] I. Bahnini, M. Rivette, A. Rechia, A. Siadat, and A. Elmesbahi, “Additive manufacturing technology: the status, applications, and prospects,” *Int. J. Adv. Manuf. Technol.*, 2018, doi: 10.1007/s00170-018-1932-y.

[20] R. Zhang, F. Jiang, L. Xue, and J. Yu, “Review of Additive Manufacturing Techniques for Large-Scale Metal Functionally Graded Materials,” *Crystals*. 2022, doi: 10.3390/cryst12060858.

[21] S. K. Bohidar, R. Sharma, and P. R. Mishra, “Functionally Graded Materials: A Critical Review,” *Int. J. Res.*, 2014.

[22] N. T. Aboulkhair et al., “3D printing of Aluminium alloys: Additive Manufacturing of Aluminium alloys using selective laser melting,” *Progress in Materials Science*. 2019, doi: 10.1016/j.pmatsci.2019.100578.

[23] G. Cardeal, B. Ferreira, P. Peças, M. Leite, and I. Ribeiro, “Designing Sustainable Business Models to Reduce Spare Part Inventory,” 2022, doi: 10.1016/j.procir.2022.02.029.

[24] D. Son, S. Kim, and B. Jeong, “Sustainable part consolidation model for customized products in closed-loop supply chain with additive manufacturing hub,” *Addit. Manuf.*, 2021, doi: 10.1016/j.addma.2020.101643.

[25] G. Udupa, S. S. Rao, and K. V. Gangadharan, “Functionally Graded Composite Materials: An Overview,” *Procedia Mater. Sci.*, 2014, doi: 10.1016/j.mspro.2014.07.442.

[26] G. H. Loh, E. Pei, D. Harrison, and M. D. Monzón, “An overview of functionally graded additive manufacturing,” *Additive Manufacturing*. 2018, doi: 10.1016/j.addma.2018.06.023.

[27] R. Ghanavati and H. Naffakh-Moosavy, “Additive manufacturing of functionally graded metallic materials: A review of experimental and numerical studies,” *Journal of Materials Research and Technology*. 2021, doi: 10.1016/j.jmrt.2021.05.022.

[28] J. J. Sobczak and L. B. Drenchev, *Metal based functionally graded materials*. 2009.

[29] M. Sathish, N. Radhika, and B. Saleh, “A critical review on functionally graded coatings: Methods, properties, and challenges,” *Composites Part B: Engineering*. 2021, doi: 10.1016/j.compositesb.2021.109278.

[30] L. Yan, Y. Chen, and F. Liou, “Additive manufacturing of functionally graded metallic materials using laser metal deposition,” *Addit. Manuf.*, vol. 31, no. October 2019, p. 100901, 2020, doi: 10.1016/j.addma.2019.100901.

[31] R. M. Mahamood and E. T. Akinlabi, “Additive Manufacturing of Funtionally Graded Materials,” in *Topics in Mining, Metallurgy and Materials Engineering*, 2017.

[32] S. Hasanov *et al.*, “Review on additive manufacturing of multi-material parts:

Progress and challenges," *Journal of Manufacturing and Materials Processing*. 2022, doi: 10.3390/jmmp6010004.

[33] C. Zhang *et al.*, "Additive manufacturing of functionally graded materials: A review," *Mater. Sci. Eng. A*, vol. 764, p. 138209, 2019, doi: https://doi.org/10.1016/j.msea.2019.138209.

[34] V. Boggarapu *et al.*, "State of the art in functionally graded materials," *Composite Structures*. 2021, doi: 10.1016/j.compstruct.2021.113596.

[35] Z. Liu, M. A. Meyers, Z. Zhang, and R. O. Ritchie, "Functional gradients and heterogeneities in biological materials: Design principles, functions, and bioinspired applications," *Progress in Materials Science*. 2017, doi: 10.1016/j.pmatsci.2017.04.013.

[36] A. Pasha and R. B.m, "Functionally graded materials (FGM) fabrication and its potential challenges & applications," 2022, doi: 10.1016/j.matpr.2021.09.077.

[37] A. Reichardt *et al.*, "Advances in additive manufacturing of metal-based functionally graded materials," *International Materials Reviews*. 2021, doi: 10.1080/09506608.2019.1709354.

[38] A. Toudehdehghan, J. W. Lim, K. E. Foo, M. I. N. Ma'Arof, and J. Mathews, "A brief review of functionally graded materials," 2017, doi: 10.1051/matecconf/201713103010.

[39] I. M. El-Galy, B. I. Saleh, and M. H. Ahmed, "Functionally graded materials classifications and development trends from industrial point of view," *SN Applied Sciences*. 2019, doi: 10.1007/s42452-019-1413-4.

[40] Y. Chen and F. Liou, "Additive manufacturing of metal functionally graded materials: A review," 2020.

[41] A. Saboori, G. Piscopo, M. Lai, A. Salmi, and S. Biamino, "An investigation on the effect of deposition pattern on the microstructure, mechanical properties and residual stress of 316L produced by Directed Energy Deposition," *Mater. Sci. Eng. A*, vol. 780, p. 139179, 2020, doi: https://doi.org/10.1016/j.msea.2020.139179.

[42] P. Guo, B. Zou, C. Huang, and H. Gao, "Study on microstructure, mechanical properties and machinability of efficiently additive manufactured AISI 316L stainless steel by high-power direct laser deposition," *J. Mater. Process. Technol.*, vol. 240, pp. 12–22, 2017, doi: https://doi.org/10.1016/j.jmatprotec.2016.09.005.

[43] X. Zhao, J. Chen, X. Lin, and W. Huang, "Study on microstructure and mechanical properties of laser rapid forming Inconel 718," *Mater. Sci. Eng. A*, vol. 478, no. 1, pp. 119–124, 2008, doi: https://doi.org/10.1016/j.msea.2007.05.079.

[44] M. Ma, Z. Wang, and X. Zeng, "A comparison on metallurgical behaviors of 316L stainless steel by selective laser melting and laser cladding deposition," *Mater. Sci. Eng. A*, vol. 685, pp. 265–273, 2017, doi: https://doi.org/10.1016/j.msea.2016.12.112.

[45] K. Zhang, S. Wang, W. Liu, and X. Shang, "Characterization of stainless steel parts by Laser Metal Deposition Shaping," *Mater. Des.*, vol. 55, pp. 104–119, 2014, doi: https://doi.org/10.1016/j.matdes.2013.09.006.

[46] P. L. Blackwell, “The mechanical and microstructural characteristics of laser-deposited IN718,” *J. Mater. Process. Technol.*, vol. 170, no. 1, pp. 240–246, 2005, doi: https://doi.org/10.1016/j.jmatprotec.2005.05.005.

[47] Z. Hu, Z. Ma, L. Yu, and Y. Liu, “Functionally graded materials with grain-size gradients and heterogeneous microstructures achieved by additive manufacturing,” *Scr. Mater.*, 2023, doi: 10.1016/j.scriptamat.2022.115197.

[48] M. Poggi, A. Salmi, E. Atzeni, and L. Iuliano, “Effect of process parameters on AISI 316L single tracks by laser powder directed energy deposition,” *Procedia CIRP*, vol. 118, pp. 735–740, 2023, doi: https://doi.org/10.1016/j.procir.2023.06.126.

[49] I. Z. Era and Z. Liu, “Effect of process parameters on tensile properties of SS 316 prepared by directional energy deposition,” *Procedia CIRP*, vol. 103, pp. 115–121, 2021, doi: https://doi.org/10.1016/j.procir.2021.10.018.

[50] G. Su, Y. Shi, G. Li, G. Zhang, and Y. Xu, “Improving the deposition efficiency and mechanical properties of additive manufactured Inconel 625 through hot wire laser metal deposition,” *J. Mater. Process. Technol.*, vol. 322, p. 118175, 2023, doi: https://doi.org/10.1016/j.jmatprotec.2023.118175.

[51] K. Liu, Z. Yan, R. Pan, F. Wang, and S. Chen, “Effect of deposition sequence on interfacial characteristics of Inconel–copper functional bimetallic structures fabricated by directed energy deposition-arc,” *Mater. Lett.*, vol. 345, p. 134487, 2023, doi: https://doi.org/10.1016/j.matlet.2023.134487.

[52] J. K. Chaurasia *et al.*, “Effect of deposition strategy and post processing on microstructure and mechanical properties of serviced Inconel 625 parts repaired using laser directed energy deposition,” *Opt. Laser Technol.*, vol. 168, p. 109831, 2024, doi: https://doi.org/10.1016/j.optlastec.2023.109831.

[53] A. du Plessis *et al.*, “Properties and applications of additively manufactured metallic cellular materials: A review,” *Progress in Materials Science*. 2022, doi: 10.1016/j.pmatsci.2021.100918.

[54] O. Abdelaal, F. Hengsbach, M. Schaper, and K. P. Hoyer, “LPBF Manufactured Functionally Graded Lattice Structures Obtained by Graded Density and Hybrid Poisson’s Ratio,” *Materials (Basel).*, 2022, doi: 10.3390/ma15124072.

[55] S. Ataollahi, “A review on additive manufacturing of lattice structures in tissue engineering,” *Bioprinting*. 2023, doi: 10.1016/j.bprint.2023.e00304.

[56] C. H. P. Nguyen, Y. Kim, and Y. Choi, “Design for Additive Manufacturing of Functionally Graded Lattice Structures: A Design Method with Process Induced Anisotropy Consideration,” *Int. J. Precis. Eng. Manuf. - Green Technol.*, 2021, doi: 10.1007/s40684-019-00173-7.

[57] Y. Wang *et al.*, “Lattice structure design optimization coupling anisotropy and constraints of additive manufacturing,” *Mater. Des.*, 2020, doi: 10.1016/j.matdes.2020.109089.

[58] A. Bandyopadhyay, Y. Zhang, and B. Onuike, “Additive manufacturing of bimetallic structures,” *Virtual Phys. Prototyp.*, vol. 17, no. 2, pp. 256–294, Apr. 2022, doi: 10.1080/17452759.2022.2040738.

[59] Y. S. Eom *et al.*, “Heat treatment effect on physical properties of stainless steel / inconel bonded by directed energy deposition,” *Arch. Metall. Mater.*, 2021, doi:

10.24425/amm.2021.136423.

[60] K. Li *et al.*, “A functionally graded material design from stainless steel to Ni-based superalloy by laser metal deposition coupled with thermodynamic prediction,” *Mater. Des.*, 2022, doi: 10.1016/j.matdes.2022.110612.

[61] A. Dass and A. Moridi, “State of the art in directed energy deposition: From additive manufacturing to materials design,” *Coatings*. 2019, doi: 10.3390/COATINGS9070418.

[62] A. Saboori *et al.*, “Application of directed energy deposition-based additive manufacturing in repair,” *Applied Sciences (Switzerland)*. 2019, doi: 10.3390/app9163316.

[63] S. L. Sing, C. F. Tey, J. H. K. Tan, S. Huang, and W. Y. Yeong, “3D printing of metals in rapid prototyping of biomaterials: Techniques in additive manufacturing,” in *Rapid Prototyping of Biomaterials: Techniques in Additive Manufacturing*, 2019.

[64] L. Zorzetto *et al.*, “Properties and role of interfaces in multimaterial 3D printed composites,” *Sci. Rep.*, 2020, doi: 10.1038/s41598-020-79230-0.

[65] I. Q. Vu, L. B. Bass, C. B. Williams, and D. A. Dillard, “Characterizing the effect of print orientation on interface integrity of multi-material jetting additive manufacturing,” *Addit. Manuf.*, 2018, doi: 10.1016/j.addma.2018.05.036.

[66] I. F. Ituarte, N. Boddeti, V. Hassani, M. L. Dunn, and D. W. Rosen, “Design and additive manufacture of functionally graded structures based on digital materials,” *Addit. Manuf.*, vol. 30, p. 100839, Dec. 2019, doi: 10.1016/j.addma.2019.100839.

[67] Y. Zhang, W. De Backer, R. Harik, and A. Bernard, “Build Orientation Determination for Multi-material Deposition Additive Manufacturing with Continuous Fibers,” 2016, doi: 10.1016/j.procir.2016.04.119.

[68] D. G. Ahn, “Directed Energy Deposition (DED) Process: State of the Art,” *International Journal of Precision Engineering and Manufacturing - Green Technology*. 2021, doi: 10.1007/s40684-020-00302-7.

[69] G. Piscopo and L. Iuliano, “Current research and industrial application of laser powder directed energy deposition,” *International Journal of Advanced Manufacturing Technology*. 2022, doi: 10.1007/s00170-021-08596-w.

[70] D. Svetlizky *et al.*, “Laser-based directed energy deposition (DED-LB) of advanced materials,” *Materials Science and Engineering: A*. 2022, doi: 10.1016/j.msea.2022.142967.

[71] G. Piscopo, E. Atzeni, A. Saboori, and A. Salmi, “An Overview of the Process Mechanisms in the Laser Powder Directed Energy Deposition,” *Applied Sciences (Switzerland)*. 2023, doi: 10.3390/app13010117.

[72] “Handbook of Stainless Steels,” *Br. Corros. J.*, 1978, doi: 10.1179/000705978798318774.

[73] “ASM specialty handbook: nickel, cobalt, and their alloys,” *Choice Rev. Online*, 2001, doi: 10.5860/choice.38-6206.

[74] K. Halmešová *et al.*, “Effect of laser power on thermal properties of multimaterial structure Inconel 718 and stainless steel 316L processed by directed energy

deposition," *J. Alloys Compd.*, vol. 927, p. 167082, 2022, doi: https://doi.org/10.1016/j.jallcom.2022.167082.

[75] A. Ascari, A. H. A. Lutey, E. Liverani, and A. Fortunato, "Laser Directed Energy Deposition of Bulk 316L Stainless Steel," *Lasers Manuf. Mater. Process.*, 2020, doi: 10.1007/s40516-020-00128-w.

[76] J. T. Pacheco *et al.*, "Laser directed energy deposition of AISI 316L stainless steel: The effect of build direction on mechanical properties in as-built and heat-treated conditions," *Adv. Ind. Manuf. Eng.*, 2022, doi: 10.1016/j.aime.2022.100079.

[77] X. Zhang *et al.*, "A novel method to prevent cracking in directed energy deposition of Inconel 738 by in-situ doping Inconel 718," *Mater. Des.*, 2021, doi: 10.1016/j.matdes.2020.109214.

[78] P. Ramiro *et al.*, "Effect of Heat Treatment on the Microstructure and Hardness of Ni-Based Alloy 718 in a Variable Thickness Geometry Deposited by Powder fed Directed Energy Deposition," *Metals (Basel).*, 2022, doi: 10.3390/met12060952.

[79] Z. Li *et al.*, "The microstructure evolution and tensile properties of Inconel 718 fabricated by high-deposition-rate laser directed energy deposition," *Addit. Manuf.*, 2020, doi: 10.1016/j.addma.2019.100941.

[80] X. Yu *et al.*, "Microstructure and fatigue crack growth behavior of Inconel 718 superalloy manufactured by laser directed energy deposition," *Int. J. Fatigue*, 2021, doi: 10.1016/j.ijfatigue.2020.106005.

[81] N. Sargent *et al.*, "Exploring Alloy Design Pathway Through Directed Energy Deposition of Powder Mixtures: A Study of Stainless Steel 316L and Inconel 718," *Addit. Manuf. Lett.*, 2023, doi: 10.1016/j.addlet.2023.100133.

[82] A. Saboori *et al.*, "An investigation on the effect of powder recycling on the microstructure and mechanical properties of AISI 316L produced by Directed Energy Deposition," *Mater. Sci. Eng. A*, 2019, doi: 10.1016/j.msea.2019.138360.

[83] Z. H. Liu, D. Q. Zhang, S. L. Sing, C. K. Chua, and L. E. Loh, "Interfacial characterization of SLM parts in multi-material processing: Metallurgical diffusion between 316L stainless steel and C18400 copper alloy," *Mater. Charact.*, 2014, doi: 10.1016/j.matchar.2014.05.001.

[84] U. Savitha *et al.*, "Chemical analysis, structure and mechanical properties of discrete and compositionally graded SS316-IN625 dual materials," *Mater. Sci. Eng. A*, 2015, doi: 10.1016/j.msea.2015.09.001.

[85] N. Chen *et al.*, "Microstructural characteristics and crack formation in additively manufactured bimetal material of 316L stainless steel and Inconel 625," *Addit. Manuf.*, vol. 32, p. 101037, 2020, doi: https://doi.org/10.1016/j.addma.2020.101037.

[86] R. Koike *et al.*, "Evaluation for mechanical characteristics of Inconel625-SUS316L joint produced with direct energy deposition," 2017, doi: 10.1016/j.promfg.2017.11.012.

[87] D. R. Feenstra, A. Molotnikov, and N. Birbilis, "Effect of energy density on the interface evolution of stainless steel 316L deposited upon INC 625 via directed energy deposition," *J. Mater. Sci.*, vol. 55, no. 27, pp. 13314–13328, Sep. 2020,

doi: 10.1007/s10853-020-04913-y.

[88] B. Chen, Y. Su, Z. Xie, C. Tan, and J. Feng, “Development and characterization of 316L/Inconel625 functionally graded material fabricated by laser direct metal deposition,” *Opt. Laser Technol.*, vol. 123, p. 105916, Mar. 2020, doi: 10.1016/j.optlastec.2019.105916.

[89] R. Koike, I. Unotoro, Y. Kakinuma, and Y. Oda, “Graded inconel 625 - SUS316L joint fabricated using directed energy deposition,” *Int. J. Autom. Technol.*, 2019, doi: 10.20965/ijat.2019.p0338.

[90] D. Wu, X. Liang, Q. Li, and L. Jiang, “Laser Rapid Manufacturing of Stainless Steel 316L/Inconel718 Functionally Graded Materials: Microstructure Evolution and Mechanical Properties,” *Int. J. Opt.*, vol. 2010, p. 802385, 2010, doi: 10.1155/2010/802385.

[91] S. Wen, K. Chen, and Y. Che, “Tailored microstructure and robust joint of Inconel 718 / 316L bimetallic multi-material fabricated by selective laser melting,” *Chinese J. Mechancial Eng.*, 2020.

[92] D. Svetlizky *et al.*, “Directed energy deposition (DED) additive manufacturing: Physical characteristics, defects, challenges and applications,” *Materials Today*. 2021, doi: 10.1016/j.mattod.2021.03.020.

[93] H. Oh, J. Lee, J. G. Kim, and S. Kim, “Effect of defects on environment-assisted fracture (EAF) behavior of Ti-6Al-4V alloy fabricated by direct energy deposition (DED),” *J. Mater. Res. Technol.*, 2022, doi: 10.1016/j.jmrt.2022.08.158.

[94] M. Liu, A. Kumar, S. Bukkapatnam, and M. Kuttolamadom, “A review of the anomalies in directed energy deposition (DED) processes & potential solutions - Part quality & defects,” 2021, doi: 10.1016/j.promfg.2021.06.093.

[95] H. Balhara, B. Botcha, S. J. Wolff, and S. T. S. Bukkapatnam, “Ripple formations determine the heterogeneous microstructure of directed energy deposition (DED)-printed 316L components,” *Mater. Des.*, 2023, doi: 10.1016/j.matdes.2023.111756.

[96] A. Wang *et al.*, “Effects of processing parameters on pore defects in blue laser directed energy deposition of aluminum by in and ex situ observation,” *J. Mater. Process. Technol.*, 2023, doi: 10.1016/j.jmatprotec.2023.118068.

[97] J. Hensel, A. Przyklenk, J. Müller, M. Köhler, and K. Dilger, “Surface quality parameters for structural components manufactured by DED-arc processes,” *Mater. Des.*, 2022, doi: 10.1016/j.matdes.2022.110438.

[98] H. Naffakh, M. Shamanian, and F. Ashrafizadeh, “Dissimilar welding of AISI 310 austenitic stainless steel to nickel-based alloy Inconel 657,” *J. Mater. Process. Technol.*, 2009, doi: 10.1016/j.jmatprotec.2008.08.019.

[99] W. Meng *et al.*, “Additive fabrication of 316L/Inconel625/Ti6Al4V functionally graded materials by laser synchronous preheating,” *Int. J. Adv. Manuf. Technol.*, 2019, doi: 10.1007/s00170-019-04061-x.

[100] S. W. Yang, J. Yoon, H. Lee, and D. S. Shim, “Defect of functionally graded material of inconel 718 and STS 316L fabricated by directed energy deposition and its effect on mechanical properties,” *J. Mater. Res. Technol.*, vol. 17, pp. 478–497, 2022, doi: https://doi.org/10.1016/j.jmrt.2022.01.029.

[101] S. H. Kim *et al.*, “Selective compositional range exclusion via directed energy deposition to produce a defect-free Inconel 718/SS 316L functionally graded material,” *Addit. Manuf.*, vol. 47, p. 102288, Nov. 2021, doi: 10.1016/j.addma.2021.102288.

[102] M. Koukolíková, T. Simson, S. Rzepa, M. Brázda, and J. Džugan, “The influence of laser power on the interfaces of functionally graded materials fabricated by powder-based directed energy deposition,” *J. Mater. Sci.*, vol. 57, no. 28, pp. 13695–13723, 2022, doi: 10.1007/s10853-022-07453-9.

[103] L. Zhang *et al.*, “Use of miniaturized tensile specimens to evaluate the ductility and formability of dual phased steels for Rapid Alloy Prototyping,” *Mater. Sci. Eng. A*, 2023, doi: 10.1016/j.msea.2023.145075.

[104] D. J. Cruz *et al.*, “Development of a mini-tensile approach for sheet metal testing using Digital Image Correlation,” 2020, doi: 10.1016/j.prostr.2020.04.036.

[105] I. van Zyl, M. Moletsane, P. Krakhmalev, I. Yadroitsava, and I. Yadroitsev, “Validation of miniaturised tensile testing on DMLS Ti6Al4V (ELI) specimens,” *South African J. Ind. Eng.*, 2016, doi: 10.7166/27-3-1666.

[106] D. J. Cruz, J. Xavier, R. L. Amaral, and A. D. Santos, “A Miniaturized Device Coupled with Digital Image Correlation for Mechanical Testing,” *Micromachines*, 2022, doi: 10.3390/mi13112027.

[107] P. Wang, M. H. Goh, Q. Li, M. L. S. Nai, and J. Wei, “Effect of defects and specimen size with rectangular cross-section on the tensile properties of additively manufactured components,” *Virtual Phys. Prototyp.*, 2020, doi: 10.1080/17452759.2020.1733430.

[108] British Standards Institution, “EN ISO 6892-1:2019 Metallic materials - Tensile testing Part 1: Method of test at room temperature,” *Br. Stand.*, 2019.

[109] ASTM, “ASTM E8/E8M standard test methods for tension testing of metallic materials,” *Annu. B. ASTM Stand.*, 2021.

[110] H. Dizdar, C. Vatab, and B. Aydemir, “Differences of Latest Versions of ISO 6892-1 and ASTM E8 Tensile Testing Standards,” *Biol. Chem. Res.*, 2016.

[111] L. Bergonzi, M. Vettori, and A. Pirondi, “Development of a miniaturized specimen to perform uniaxial tensile tests on high performance materials,” 2019, doi: 10.1016/j.prostr.2020.02.018.

[112] P. Konopik, P. Farahnak, M. Rund, J. Džugan, and S. Rzepa, “Applicability of miniature tensile test in the automotive sector,” 2018, doi: 10.1088/1757-899X/461/1/012043.

[113] R. Procházka, P. Sláma, J. Dlouhỳ, P. Konopík, and Z. Trojanová, “Local mechanical properties and microstructure of EN AW 6082 aluminium alloy processed via ECAP-conform technique,” *Materials (Basel).*, 2020, doi: 10.3390/ma13112572.

[114] S. Rzepa *et al.*, “Tensile properties evaluation of additively manufactured AISI 316L thin wall and bulk material using various miniaturized specimen geometries,” *IOP Conf. Ser. Mater. Sci. Eng.*, 2021, doi: 10.1088/1757-899x/1178/1/012048.

[115] M. Urbánek *et al.*, “Prediction of Behaviour of Thin-Walled DED-Processed

Structure: Experimental-Numerical Approach," *Materials* , vol. 15, no. 3. 2022, doi: 10.3390/ma15030806.

[116] M. Henning and H. Vehoff, "Statistical size effects based on grain size and texture in thin sheets," *Mater. Sci. Eng. A*, 2007, doi: 10.1016/j.msea.2006.11.113.

[117] P. Zheng *et al.*, "On the standards and practices for miniaturized tensile test – A review," *Fusion Eng. Des.*, 2020, doi: 10.1016/j.fusengdes.2020.112006.

[118] H. Liu, Y. Shen, S. Yang, P. Zheng, and L. Zhang, "A comprehensive solution to miniaturized tensile testing: Specimen geometry optimization and extraction of constitutive behaviors using inverse FEM procedure," *Fusion Eng. Des.*, 2017, doi: 10.1016/j.fusengdes.2017.07.016.

[119] S. Karnati, J. L. Hoerchler, F. Liou, and J. W. Newkirk, "Influence of gage length on miniature tensile characterization of powder bed fabricated 304L stainless steel," 2020.

[120] B. Strnadel and J. Brumek, "The size effect in tensile test of steels," 2013, doi: 10.1115/PVP2013-98162.

[121] K. Kumar *et al.*, "Use of miniature tensile specimen for measurement of mechanical properties," 2014, doi: 10.1016/j.proeng.2014.11.112.

[122] S. Karnati, S. P. Isanaka, Y. Zhang, F. F. Liou, and J. L. Schulthess, "A Comparative Study on Representativeness and Stochastic Efficacy of Miniature Tensile Specimen Testing," *Mater. Perform. Charact.*, 2022, doi: 10.1520/MPC20210136.

[123] S. Raghavan *et al.*, "Effect of post-treatment on local mechanical properties of additively manufactured impellers made of maraging steel," *Rapid Prototyp. J.*, 2023, doi: 10.1108/RPJ-03-2022-0089.

[124] J. Dzugan *et al.*, "Effects of thickness and orientation on the small scale fracture behaviour of additively manufactured Ti-6Al-4V," *Mater. Charact.*, vol. 143, pp. 94–109, 2018, doi: 10.1016/j.matchar.2018.04.003.

[125] "Cracks and fracture," in *Cracks and Fracture*, 1999.

[126] B. A. Baykal and P. Spätig, "Analysis of crack front loading to improve reliability of fracture toughness calculations based on miniaturized CT specimens," *Procedia Struct. Integr.*, vol. 42, pp. 1350–1360, 2022, doi: https://doi.org/10.1016/j.prostr.2022.12.172.

[127] B. A. Baykal and P. Spätig, "Constraint loss correction: Enhancing transferability of fracture toughness of Eurofer97 compact tension specimens between specimen sizes," *Eng. Fract. Mech.*, vol. 293, p. 109682, 2023, doi: https://doi.org/10.1016/j.engfracmech.2023.109682.

[128] M. Li, I. Uytdenhouwen, T. Pardoen, R. Chaouadi, and M. Lambrecht, "Effect of the pre-crack non-uniformity on the initiation of brittle fracture in mini-CT specimen," *Eng. Fract. Mech.*, vol. 290, p. 109457, 2023, doi: https://doi.org/10.1016/j.engfracmech.2023.109457.

[129] M. Li, R. Chaouadi, I. Uytdenhouwen, and T. Pardoen, "Size correction scheme to determine fracture toughness with mini-CT geometry in the transition regime," *Eng. Fract. Mech.*, vol. 290, p. 109486, 2023, doi:

https://doi.org/10.1016/j.engfracmech.2023.109486.

[130] S. Rzepa *et al.*, “Effect of ECAP on fracture toughness and fatigue endurance of DED-processed Ti-6Al-4V investigated on miniaturized specimens,” *J. Alloys Compd.*, vol. 968, p. 172167, 2023, doi: https://doi.org/10.1016/j.jallcom.2023.172167.

[131] M. S. Duval-Chaneac *et al.*, “Fatigue crack growth in IN718/316L multi-materials layered structures fabricated by laser powder bed fusion,” *Int. J. Fatigue*, vol. 152, p. 106454, Nov. 2021, doi: 10.1016/j.ijfatigue.2021.106454.

[132] ASTM International, “E1820-18a Standard Test Method for Measurement of Fracture Toughness,” *ASTM B. Stand.*, 2019.

[133] M. Sevčík, P. Hutař, L. Náhlík, and Z. Knésl, “An evaluation of the stress intensity factor in functionally graded materials,” 2009.

[134] P. R. Marur and H. V. Tippur, “Numerical analysis of crack-tip fields in functionally graded materials with a crack normal to the elastic gradient,” *Int. J. Solids Struct.*, 2000, doi: 10.1016/S0020-7683(99)00207-3.

[135] Z. H. Jin and R. C. Batra, “Some basic fracture mechanics concepts in functionally graded materials,” *J. Mech. Phys. Solids*, 1996, doi: 10.1016/0022-5096(96)00041-5.

[136] R. O. Ritchie and D. Liu, *Introduction to Fracture Mechanics*. 2021.

[137] B. Pan, K. Qian, H. Xie, and A. Asundi, “Two-dimensional digital image correlation for in-plane displacement and strain measurement: A review,” *Meas. Sci. Technol.*, 2009, doi: 10.1088/0957-0233/20/6/062001.

[138] N. McCormick and J. Lord, “Digital Image Correlation,” *Mater. Today*, vol. 13, no. 12, pp. 52–54, 2010, doi: https://doi.org/10.1016/S1369-7021(10)70235-2.

[139] Z. Wu *et al.*, “A Metallic Fracture Estimation Method Using Digital Image Correlation,” *Processes*, 2022, doi: 10.3390/pr10081599.

[140] B. Pan, “Digital image correlation for surface deformation measurement: Historical developments, recent advances and future goals,” *Measurement Science and Technology*. 2018, doi: 10.1088/1361-6501/aac55b.

[141] F. Hild and S. Roux, “Digital image correlation: From displacement measurement to identification of elastic properties - A review,” *Strain*. 2006, doi: 10.1111/j.1475-1305.2006.00258.x.

[142] D. Melzer, J. Džugan, M. Koukolíková, S. Rzepa, and J. Vavřík, “Structural integrity and mechanical properties of the functionally graded material based on 316L/IN718 processed by DED technology,” *Mater. Sci. Eng. A*, vol. 811, p. 141038, Apr. 2021, doi: 10.1016/j.msea.2021.141038.

[143] D. Melzer *et al.*, “Fracture characterisation of vertically build functionally graded 316L stainless steel with Inconel 718 deposited by directed energy deposition process,” *Virtual Phys. Prototyp.*, vol. 17, no. 4, pp. 821–840, Oct. 2022, doi: 10.1080/17452759.2022.2073793.

[144] D. Melzer *et al.*, “Influence of interface orientation and surface quality on structural and mechanical properties of SS316L/IN718 block produced using directed energy deposition,” *Surfaces and Interfaces*, p. 103139, 2023, doi: https://doi.org/10.1016/j.surfin.2023.103139.

[145] ISO, “ISO 6892-1 Metallic materials — Tensile testing — Part 1: Method of test at room temperature 1,” *Met. Mater.*, 2009.

[146] ASTM E1820 - 20e1, “Standard Test Method for Measurement of Fracture Toughness.” West Conshohocken, PA, 2020, p. West Conshohocken, PA, 2020, [Online]. Available: www.astm.org.

[147] C. T. Sun and Z.-H. Jin, “Chapter 5 - Mixed Mode Fracture,” in *Fracture Mechanics*, C. T. Sun and Z.-H. Jin, Eds. Boston: Academic Press, 2012, pp. 105–121.

[148] U. P. Singh, S. Swaminathan, and G. Phanikumar, “Thermo-mechanical approach to study the residual stress evolution in part-scale component during laser additive manufacturing of alloy 718,” *Mater. Des.*, 2022, doi: 10.1016/j.matdes.2022.111048.

[149] E. Hallberg, “Investigation of hot cracking in additive manufactured nickel-base superalloys,” 2018, [Online]. Available: https://api.semanticscholar.org/CorpusID:55141002.

[150] X. Zhao, J. Chen, X. Lin, and W. Huang, “Study on microstructure and mechanical properties of laser rapid forming Inconel 718,” *Mater. Sci. Eng. A*, 2008, doi: 10.1016/j.msea.2007.05.079.

[151] X. K. Zhu and J. A. Joyce, “Review of fracture toughness (G, K, J, CTOD, CTOA) testing and standardization,” *Eng. Fract. Mech.*, 2012, doi: 10.1016/j.engfracmech.2012.02.001.

[152] M. A. Sokolov *et al.*, “Fracture toughness characterization of 304L and 316L austenitic stainless steels and alloy 718 after irradiation in high-energy, mixed proton/neutron spectrum,” 2000, doi: 10.1520/stp10530s.

[153] W. J. Mills, “Fracture Toughness Variations for Alloy 718 Base Metal and Welds,” 2012, doi: 10.7449/1989/superalloys_1989_517_532.

[154] M. R. Gotterbarm *et al.*, “Small scale testing of IN718 single crystals manufactured by EB-PBF,” *Addit. Manuf.*, vol. 36, p. 101449, 2020, doi: https://doi.org/10.1016/j.addma.2020.101449.

10 List of own publications

Year of publication	Impact factor	Quartile	Publication
2023	-	-	S. Rzepa, M. Uhlík, **D. Melzer**, M. Koukolíková, P. Konopík, J. Džugan, Mechanical Behavior of 316L-IN718 Interface Produced by Directed Energy Deposition Investigated Using Miniaturized Specimens, ASME 2023 Pressure Vessels & Piping Conference, 2023: p. V005T06A092. https://doi.org/10.1115/PVP2023-106298.
2023	6,2	Q1	S. Rzepa, Z. Trojanová, **D. Melzer**, R. Procházka, M. Koukolíková, P. Podaný, J. Džugan, Effect of ECAP on fracture toughness and fatigue endurance of DED-processed Ti-6Al-4V investigated on miniaturized specimens, J. Alloys Compd. 968 (2023) 172167. https://doi.org/https://doi.org/10.1016/j.jallcom.2023.172167.
2023	6,4	Q1	**D. Melzer**, J. Gil, S. Rzepa, R. Amaral, P. Podaný, J. Džugan, A. Reis, Ambient and high temperature tensile behaviour of DLD-manufactured inconel 625/42C steel joint, Mater. Sci. Eng. A. (2023). https://doi.org/10.1016/j.msea.2023.145603.
2023	6,2	Q1	**D. Melzer**, M. Koukolíková, S. Rzepa, Y. Li, J. Džugan, M. Brázda, Influence of interface orientation and surface quality on structural and mechanical properties of SS316L/IN718 block produced using directed energy deposition, Surfaces and Interfaces. (2023) 103139. https://doi.org/https://doi.org/10.1016/j.surfin.2023.103139.
2023	5,4	Q1	E. Azinpour, S. Rzepa, **D. Melzer**, A. Reis, J. Džugan, J.M.A. Cesar de Sa, Phase-field ductile fracture analysis of multi-materials and functionally graded composites through numerical and experimental methods, Theor. Appl. Fract. Mech. (2023). https://doi.org/10.1016/j.tafmec.2023.103906.

2023	3,4	Q2	P. Salvetr, A. Školáková, J. Kotous, J. Drahokoupil, **D. Melzer**, Z. Jansa, Č. Donik, A. Gokhman, Z. Nový, Effect of Double-Step and Strain-Assisted Tempering on Properties of Medium-Carbon Steel, Materials (Basel). (2023). https://doi.org/10.3390/ma16052121.
2023	4,9	Q1	S. Rzepa, Z. Trojanová, J. Džugan, R.Z. Valiev, M. Koukolíková, **D. Melzer**, M. Brázda, Effect of ECAP processing on microstructure and mechanical behaviour of Ti-6Al-4V manufactured by directed energy deposition, Mater. Charact. (2023). https://doi.org/10.1016/j.matchar.2022.112622.
2022	2,7	Q2	F. Galgon, **D. Melzer**, C. Zenk, J. Džugan, C. Körner, Miniature mechanical testing of LMD-fabricated compositionally & microstructurally graded γ titanium aluminides, J. Mater. Res. (2022). https://doi.org/10.1557/s43578-022-00801-0.
2022	6,4	Q1	P. Salvetr, A. Školáková, **D. Melzer**, M. Brázda, J. Duchoň, J. Drahokoupil, P. Svora, Š. Msallamová, P. Novák, Characterization of super duplex stainless steel SAF2507 deposited by directed energy deposition, Mater. Sci. Eng. A. (2022). https://doi.org/10.1016/j.msea.2022.144084.
2022	10,6	Q1	**D. Melzer**, J. Džugan, M. Koukolíková, S. Rzepa, J. Dlouhý, M. Brázda, T. Bucki, Fracture characterisation of vertically build functionally graded 316L stainless steel with Inconel 718 deposited by directed energy deposition process, Virtual Phys. Prototyp. (2022). https://doi.org/10.1080/17452759.2022.2073793.
2022	-		R. Singh, J. Kondás, C. Bauer, J. Cizek, J. Medricky, S. Csaki, J. Čupera, R. Procházka, **D. Melzer**, P. Konop.ík, Bulk-like ductility of cold spray additively manufactured copper in the as-sprayed state, Addit. Manuf. Lett. 3 (2022) 100052. https://doi.org/https://doi.org/10.1016/j.addlet.2022.100052.

2022	3,75	Q2	M. Urbánek, J. Hodek, **D. Melzer**, M. Koukolíková, A. Prantl, J. Vavřík, M. Brázda, P. Martínek, S. Rzepa, J. Džugan, Prediction of Behaviour of Thin-Walled DED-Processed Structure: Experimental-Numerical Approach, Mater. . 15 (2022). https://doi.org/10.3390/ma15030806.
2022	6,2	Q1	**D. Melzer**, I. Smirnov, O. Lukáš, J. Dlouhý, A. Evstifeev, J. Džugan, R. Valiev, Fracture locus characteristics of Al alloy 5083 processed by equal channel angular pressing using miniaturized specimens, J. Alloys Compd. (2022). https://doi.org/10.1016/j.jallcom.2021.161675.
2021	-	-	S. Rzepa, **D. Melzer**, M. Koukolíková, P. Konopík, M. Brázda, J. Vavřík, Tensile properties evaluation of additively manufactured AISI 316L thin wall and bulk material using various miniaturized specimen geometries, IOP Conf. Ser. Mater. Sci. Eng. (2021). https://doi.org/10.1088/1757-899x/1178/1/012048.
2021	-	-	M. Brázda, P. Salvetr, S. Rzepa, **D. Melzer**, J. Vavřík, Effect of heat treatment on mechanical properties of duplex steel SAF 2507 manufactured by DED, IOP Conf. Ser. Mater. Sci. Eng. (2021). https://doi.org/10.1088/1757-899x/1178/1/012008.
2021	6	Q1	**D. Melzer**, J. Džugan, M. Koukolíková, S. Rzepa, J. Vavřík, Structural integrity and mechanical properties of the functionally graded material based on 316L/IN718 processed by DED technology, Mater. Sci. Eng. A. (2021). https://doi.org/10.1016/j.msea.2021.141038.
2021	-	-	M. Rund, S. Rzepa, **D. Melzer**, P. Konopík, M. Urbánek, Improved methodology for validation of the FEA model using testing components, in: Met. 2021 - 30th Anniv. Int. Conf. Metall. Mater. Conf. Proc., 2021. https://doi.org/10.37904/metal.2021.4150.

2021	3,46	Q1	M.R. Sunilkumar, E. Schmidova, P. Konopík, **D. Melzer**, Fracture toughness examination of dual-phase and interstitial free steel using essential work of fracture method, Fatigue Fract. Eng. Mater. Struct. (2021). https://doi.org/10.1111/ffe.13555.
2020	-	-	J. Džugan, **D. Melzer**, M. Koukolíková, J. Vavřík, M. Seifi, Characterization of functionally graded materials based on inconel 718 and stainless steel 316L manufactured by DED process, in: ASTM Spec. Tech. Publ., 2020. https://doi.org/10.1520/STP163120190138.
2020	2,4	Q2	S.K.M. R, E. Schmidova, P. Konopík, **D. Melzer**, F. Bozkurt, N. V. Londe, Fracture toughness analysis of automotive-grade dual-phase steel using essential work of fracture (Ewf) method, Metals (Basel). (2020). https://doi.org/10.3390/met10081019.
2020	7	Q1	M.R. Gotterbarm, M. Seifi, **D. Melzer**, J. Džugan, A.A. Salem, Z.H. Liu, C. Körner, Small scale testing of IN718 single crystals manufactured by EB-PBF, Addit. Manuf. (2020). https://doi.org/10.1016/j.addma.2020.101449.
2020	-	-	E. Chvostová, J. Horváth, P. Konopík, S. Rzepa, **D. Melzer**, Optimization of test specimen dimensions for thermal power station exposure device, in: IOP Conf. Ser. Mater. Sci. Eng., 2020. https://doi.org/10.1088/1757-899X/723/1/012009.
2020	-	-	**D. Melzer**, I. Smirnov, A. Evstifeev, S. Rzepa, P. Konopík, Effect of revolutions number on mechanical properties of HPT processed copper, in: IOP Conf. Ser. Mater. Sci. Eng., 2020. https://doi.org/10.1088/1757-899X/723/1/012019.
2019	-	-	P. Konopik, M. Rund, S. Rzepa, J. Dzugan, **D. Melzer**, Compatibility of fracture toughness results in the upper shelf region, in: Procedia Struct. Integr., 2019. https://doi.org/10.1016/j.prostr.2019.08.063.

List of figures and tables

Figures

FIGURE 1. FGM BASIC CLASSIFICATIONS BASED ON THE SCALE AND PRODUCTION METHOD [29]. 18

FIGURE 2. GRAPHICAL REPRESENTATION OF DIFFERENT JOINING METHODS OF FGM PRODUCTION [30]........ 19

FIGURE 3. SCHEMA OF DIRECTED ENERGY DEPOSITION PROCESS PRINCIPLE [63]........ 23

FIGURE 4. TIMELINE OF THE EXPERIMENTAL PART EVOLUTION. 42

FIGURE 5. EXTRACTION PLAN OF MTT SPECIMENS PRODUCTION FROM HB, VB AND IBS WITH THE SPECIMEN'S DESIGNATION SYSTEM EXAMPLES. 50

FIGURE 6. A) MTT SETUP; B) MTT SPECIMEN GEOMETRY........ 50

FIGURE 7. MCT SPECIMEN'S EXTRACTION SCHEMA WITH SPECIFIC LOCATIONS AND ORIENTATIONS FOR HB AND VB........ 52

FIGURE 8. A) FRACTURE TOUGHNESS TESTING SETUP; B) MCT SPECIMEN GEOMETRY. 53

FIGURE 9. FGM BLOCK WITH HORIZONTALLY ORIENTED INTERFACES BETWEEN 316L AND IN718 REFERRED AS HB AND SCHEMA OF THE DEPOSITION SEQUENCES REPETITION FROM THE TOP-DOWN VIEW. 55

FIGURE 10. IMAGE ANALYSIS OF THE DEFECTS IN THE AREA ACROSS THE MULTIPLE INTERFACES OF HB AND WITHIN THE AREAS OF MATERIALS INTERFACES........ 56

FIGURE 11. ETCHED STRUCTURE OF THE HB WITH REVEALED SHARP AND GRADUAL INTERFACES BETWEEN INDIVIDUAL MATERIALS........ 57

FIGURE 12. EDS MAPPING OF FE (RED) AND NI (GREEN) ELEMENTS AT THE TWO TYPES OF INTERFACE OF HB........ 59

FIGURE 13. EDS LINE SCAN ACROSS THE SHARP AND GRADUAL INTERFACE OF HB. 59

FIGURE 14. EBSD IMAGES OF SHARP AND GRADUAL INTERFACES OF HB WITH FUSION LINE HIGHLIGHTED BY DASHED YELLOW LINE........ 60

FIGURE 15. REPRESENTATIVE ENGINEERING TENSILE CURVES OF INDIVIDUAL MATERIALS AND INTERFACES OF HB........ 61

FIGURE 16. COLUMN GRAPHS OF MTT RESULTS OF HB FOR 316L MATERIAL: A) XYZ-ORIENTED, B) YXZ-ORIENTED AND C) ZYX-ORIENTED........ 62

FIGURE 17. COLUMN GRAPHS OF MTT RESULTS OF HB FOR IN718 MATERIAL: A) XYZ-ORIENTED, B) YXZ-ORIENTED AND C) ZYX-ORIENTED........ 63

FIGURE 18. COLUMN GRAPHS OF MTT RESULTS OF HB FOR INTERFACE LOCATED SPECIMENS: A) R_M AND $R_{P0,2}$ PARAMETERS; B) A, A_G AND Z PARAMETERS........ 64

FIGURE 19. SUMMARY OF J-R CURVES FOR SINGLE MATERIAL-LOCATED MCT SPECIMENS OF HB. 65

FIGURE 20. SUMMARY OF J-R CURVES FOR AT THE INTERFACE-LOCATED MCT OF HB. 66

FIGURE 21. A) FRACTURE MORPHOLOGY OF 316L-LOCATED MTT; B) FRACTURE MORPHOLOGY OF IN718-LOCATED MTT; C) FRACTURE MORPHOLOGY OF SHARP INTERFACE-LOCATED MTT; D) FRACTURE MORPHOLOGY OF GRADUAL INTERFACE-LOCATED MTT........ 67

FIGURE 22. A) FRACTURE MORPHOLOGY OF HORIZONTALLY ORIENTED MTT AT THE SHARP INTERFACE; B) DETAIL OF FRACTURE MORPHOLOGY TRANSITION OF SHARP INTERFACE; C) FRACTURE MORPHOLOGY OF HORIZONTALLY ORIENTED MTT AT THE GRADUAL INTERFACE; D) EDS LINE SCAN ANALYSIS OF GRADUAL INTERFACE LOCATED MTT SPECIMEN. 68

FIGURE 23. FRACTURE MORPHOLOGY OF MCT SPECIMENS OF HB: A) 316L-LOCATED MCT SPECIMEN; B) IN718-LOCATED SPECIMEN; C) AT THE SHARP INTERFACE-LOCATED MCT SPECIMEN; D) AT THE GRADUAL INTERFACE-LOCATED MCT SPECIMEN; E) FROM 316L TO IN718 CRACK MORPHOLOGY; F) FROM IN718 TO 316L CRACK MORPHOLOGY. 69

Figure 24. a) FGM block with vertically oriented interfaces between 316L and IN718 referred as VB, b) schema of the deposition sequences repetition of each layer from top-down view, c) schema of the deposition process. 70
Figure 25. Image analysis of the defects in the area across the multiple interfaces of VB and within the areas of materials interfaces. 71
Figure 26. Etched structure of the VB with revealed sharp and gradual interfaces between individual materials. 73
Figure 27. Detail of gradual interface of VB with marked 316L zone, cracking zone, and interface zone. 74
Figure 28. Detail of the structure variability within the single melt-pool of VB. 74
Figure 29. EDS mapping of Fe (red) and Ni (green) elements at the two interfaces of VB. 75
Figure 30. EDS line scan across the sharp and gradual interface of VB. 75
Figure 31. EBSD map of grain distribution and orientation across the two interfaces of VB with fusion line marked by yellow dotted line. 76
Figure 32. Representative engineering tensile curves of individual materials and interfaces of VB. 77
Figure 33. Column graphs of MTT results of VB for material 316Ll: a) XZY-oriented, b) ZYX-oriented. 78
Figure 34. Column graphs of MTT results of VB for material IN718, a) ZYX-oriented, b) XZY-oriented. 79
Figure 35. Column graphs of MTT results of VB for interface located specimens: a) Sharp interface YZX-oriented, b) Gradual interface YZX-oriented. 80
Figure 36. Summary of J-R curves for single material-located and interface-located MCT specimens of VB. 81
Figure 37. SEM images of MTT fracture surfaces with red marked areas highlighting the presence of ductile material failure and solidification cracking areas: (a) XZY IN718, (b) ZXY IN718, (c) XZY 316L, (d) ZXY 316L, (e) YZX 316L, (f) YZX IN718. 82
Figure 38. Fracture morphology of VB MCT: a) 316L, b) IN718, c) Interface sharp, d) interface gradual, e) transition from IN718 to 316L. 84
Figure 39. MCT specimen after the fracture toughness test with clearly deflected crack propagation plane. 85
Figure 40. a) FGM blocks with inclined interfaces between 316L and IN718 ranging from 15° to 60° deposited continuously CIB, b) schema of the deposition sequences repetition from the top-down view of the build.. 86
Figure 41. Macrographs of CIB blocks in polished state with designated areas of measured porosity. 87
Figure 42. Light microscope images of CIB interfaces. 88
Figure 43. EDS mapping of Fe (red) and Ni (green) elements at the interface of CIB15 and CIB60. 89
Figure 44. EDS line scans across the CIB interfaces. 90
Figure 45. EBSD images of CIB15 and CIB60 with the fusion lines marked by yellow dashed lines. 91
Figure 46. Representative tensile curves of CIB MTT specimens. 92
Figure 47. Columns graphs of tensile parameters evaluated for CIB MTT specimens. 92
Figure 48. SEM images of MTT specimen's fracture surfaces for continuous blocks, a) CIB15; b) CIB30; c) CIB45; d) CIB60. 94
Figure 49. FGM blocks with inclined interfaces between 316L and IN718 ranging

from 15° to 60° deposited discontinuously (DIB) and schema of the deposition sequences. 95
***Figure 50**. Macrographs of DIB blocks in polished state with designated areas of measured porosity.* 96
Figure 51. Light microscope images of DIB interfaces. 97
Figure 52. EDS mapping of Fe (red) and Ni (green) elements at the interface of DIB15 and DIB60. 98
Figure 53. EDS line scans across the DIB interfaces. 99
Figure 54. EBSD images of DIB15 and DIB60 with the fusion lines marked by yellow dashed lines. 100
Figure 55. Representative engineering tensile curves of interface located MTT of DIB. 101
Figure 56. Column graphs of MTT results of DIB for interface located specimens. 101
Figure 57. SEM images of MTT specimen's fracture surfaces for DIB, a) DIB15; b) DIB30; c) DIB45; d) DIB60. 102
Figure 58. Strain distribution of MTT specimen located across the gradual interface (ZYX) a) before loading; b) elastic part of the test; c) at fracture; d) major strain profile at the elastic stage of tensile load. 104
Figure 59. Strain distribution of MTT specimen located across the sharp interface (ZYX) a) before loading; b) elastic part of the test; c) at fracture; d) major strain profile at the elastic stage of tensile load. 106
Figure 60. Comparison of the extensometer-time evolution between full extensometer length (4 mm) and half extensometer gauge length of 2 mm for individual halves of the specimens. 107
Figure 61. Comparison of the engineering tensile curves between individual materials and sharp interface. 107
Figure 62. Strain distribution of MTT specimen located across the sharp interface (YXZ) a) before loading; b) elastic part of the test; c) at fracture; d) major strain profile at the elastic stage of tensile load. 109
Figure 63. Comparison of major strain profiles along the gauge length of MTT specimens between sharp and gradual interfaces. 110
Figure 64. Single material zone orientation in relation to the melt-pool and final interface appearance. 112
Figure 65. Representation of the grain growth perpendicular to the molten pool tracks (yellow dashed line) and across multiple molten pool tracks with curved shape as a result of epitaxial growth at the sharp interface of vertical block. 115
Figure 66. Evolution of the porosity at the interface of FGM with respect to the interface orientation and application of pre-machining operation. 118
Figure 67. Evolution of tensile properties with the interface orientation between 316L and IN718. 120

Tables

TABLE 1. SEVEN MAIN AM PROCESSES ACCORDING THE ASTM F42 [3]. 14
TABLE 2. LIST OF VARIOUS FGM PRODUCTION TECHNIQUES CLASSIFIED ACCORDING TO THE PROCESS TYPE [25]. 16
TABLE 3. SPECIFIC MATERIAL PROPERTIES OF THE TWO MAIN CONSTITUENTS 316L AND IN718. 26
TABLE 4. LIST OF USED MACHINES AND SYSTEMS FOR THE REALIZATION OF EXPERIMENTAL PART IN COMTES FHT A.S. 45
TABLE 5. DEPOSITION PARAMETERS FOR BOTH 316L AND IN718 OF PRODUCED FGM. 49
TABLE 6. SUMMARY OF FRACTURE TOUGHNESS RESULTS FOR HB. 66
TABLE 7. EVALUATED DEFECTS FRACTION IN THE INDIVIDUAL AREAS OF THE VB SPECIMEN. 72
TABLE 8. SUMMARY OF FRACTURE TOUGHNESS RESULTS FOR VB. 81
TABLE 9. POROSITY VALUES AT THE INTERFACE AND INDIVIDUAL MATERIAL ZONES OF CIB. 87
TABLE 10. RESULTS OF SEM FRACTOGRAPHY OF REPRESENTATIVE MTT CIB SPECIMENS WITH EVALUATED FRACTURE LOCATION. 93
TABLE 11. SUMMARY OF POROSITY VALUES PER EACH MEASURED AREA OF INCLINED INTERFACES DIB. 96
TABLE 12. RESULTS OF SEM FRACTOGRAPHY OF REPRESENTATIVE MTT DIB SPECIMENS WITH EVALUATED FRACTURE LOCATION. 102
TABLE 13. COMPARISON OF COMPOSITIONAL WIDTH CHANGE ACROSS THE INTERFACE FOR EACH FGM MODIFICATION AND DIMENSION OF THE MELT-POOLS. 114
TABLE 14. COMPARISON OF DEFECTS CONCENTRATION BETWEEN EACH FGM. 118
TABLE 15. SUMMARY OF TENSILE PARAMETERS VALUES FOR ALL FGMS. 121
TABLE 16. COMPARISON OF TENSILE RESULTS FOR INDIVIDUAL MATERIALS AND INTERFACE WITH CHOSEN LITERATURE DATA. 122
TABLE 17. SUMMARY OF FRACTURE TOUGHNESS RESULTS FOR INDIVIDUAL MATERIALS AND INTERFACES OF HB AND VB. 125